University of Genoa
Department of Physics
PhD course in Physics and Nanosciences
Cycle XXXVIII

UNIVERSITÀ DEGLI STUDI DI GENOVA

Electromagnetic Noise in Gravitational-Wave Detectors

PhD Candidate:
Federico Armato

Advisor:
Dr. Andrea Chincarini
Dr. Marco Raveri

Co-Advisors:
Dr. Irene Fiori
Dr. Rosario De Rosa

Academic Year 2025/2026

Acknowledgements

Ho riflettuto a lungo su come iniziare questi ringraziamenti e, a differenza del resto della tesi, ho scelto volutamente di scriverli in italiano. Essendo la mia lingua madre, mi sento più a mio agio nell'esprimere pienamente ciò che provo, e soprattutto perché tutte le persone a cui sono rivolti parlano italiano.

Il mio primo ringraziamento va al mio relatore, Andrea. Non si tratta di un semplice gesto formale, ma di una sincera gratitudine. Andrea non è solo una persona di straordinario valore dal punto di vista accademico, ma anche e soprattutto umano. Fin dai primi giorni mi sono trovato benissimo con lui e con tutto il gruppo del laboratorio, dove ho respirato fin da subito un clima sereno e positivo. Gran parte di questo merito va proprio ad Andrea, che non si è mai posto come un professore distaccato, ma come una guida disponibile, sempre pronta ad aiutarci. Il suo modo di insegnare fa emergere la profonda differenza tra chi spiega per dimostrare ciò che sa e chi spiega perché desidera davvero far comprendere.

Un grande grazie va anche a tutto il resto del laboratorio, un gruppo di persone speciali che mi hanno fatto sentire a casa fin dal primo giorno.

Tra questi ci tengo a ringraziare particolarmente Barbara e Francesca che, con la loro esperienza nel mio stesso ambito, sono state per me due punti di riferimento preziosissimi, sempre pronte a offrire supporto.

Voglio poi ringraziare tutti i miei amici, che hanno reso e rendono tutte le mie giornate più piacevoli, e così indirettamente hanno contribuito a questo risultato.

Ultimi, ma non per importanza, i miei genitori, Laura e Francesco, e la mia cagnolina, Viola, che mi hanno supportato sempre, con parole e con fatti, nelle mie scelte.

Abstract

The observation of gravitational waves represents the ultimate frontier of contemporary multi-messenger astronomy. This scientific milestone is achieved through long-baseline laser interferometers, complex instruments capable of detecting spacetime metric perturbations with a strain sensitivity on the order of 10^{-22} (corresponding to test mass displacements of approximately 10^{-18} m). Reaching such extreme precision requires highly sophisticated noise isolation and mitigation strategies. Among these noise sources, electromagnetic noise is playing an increasingly decisive role, emerging as a primary limiting factor for the low-frequency sensitivity of current and future third-generation detectors. However, the research effort dedicated to this noise source has not kept pace with its growing phenomenological impact. This doctoral thesis develops a systematic treatment of electromagnetic noise, aiming to outline the current state of the art and, crucially, to identify the boundaries of our current understanding and mitigation capabilities. By integrating numerical modeling with experimental validation — including the development of the MANET facility and the investigation of advanced shielding and actuator redesign (CALMA project) — this work establishes the methodological foundations for a 'by-design' management of magnetic noise, a fundamental prerequisite for the ultimate scientific success of the Einstein Telescope. Furthermore, by proposing an in-situ monitoring system, this work provides a framework for the investigation of electrostatic noise, addressing the current uncertainties regarding charge deposition on test masses.

Contents

Introduction

Gravitational waves (GWs) represent one of the most significant predictions of Albert Einstein's General Relativity, which postulated their existence in 1916 as wave-like solutions to the field equations. These perturbations in the spacetime metric propagate at the speed of light, carrying encoded information regarding the dynamics of the most energetic and violent astrophysical processes in the universe, thereby acting as a probe complementary to traditional electromagnetic radiation.

The experimental path toward their detection began in the 1960s with the pioneering work of Joseph Weber [1, 2], who proposed the use of resonant masses (metallic bars) to intercept the flux of gravitational radiation. Weber's intuition was based on the ability of an incident wave to excite the mechanical eigenmodes of the bar, producing vibrations measurable via piezoelectric transducers. Over the decades, this technology evolved into complex cryogenic systems — such as the **Nautilus** [3] and **AURIGA** [4] detectors — operating at temperatures near absolute zero to minimize thermal noise contributions and maximize spectral sensitivity.

Despite resonant detectors constituting a fundamental milestone in experimental gravitational physics, they were inherently limited by an extremely narrow bandwidth centered on the instrument's mechanical resonance frequency. This characteristic rendered them unsuitable for observing broadband signals, such as those produced by the coalescence of compact binary systems, which require sensitivity extended over a wide frequency range.

The transition toward modern gravitational astronomy was made possible by the development of kilometric-arm Michelson laser interferometers, such as **LIGO** [5], **Virgo** [6], and **KAGRA** [7]. On September 14, 2015, at 09:50:45 UTC, the Advanced LIGO detectors recorded the event **GW150914** [8], marking the first direct observation of a gravitational wave. The signal, generated by the merger of two black holes at a distance of approximately 1.3 billion light-years, experimentally confirmed the validity of General Relativity in the strong-field regime and officially inaugurated the era of multi-messenger astronomy.

The success of gravitational wave interferometers, however, was not a foregone conclusion but rather the result of a concerted effort by the scientific community. Indeed, the presence of various noise sources, if not appropriately mitigated, effectively precludes the observation of signals as infinitesimal as gravitational ones.
Among these noise sources is electromagnetic noise, the systematic study and mitigation of which is the central objective of this thesis. This source of disturbance is assuming an increasingly critical role in limiting the sensitivity of second-generation detectors and represents, according to current projections, one of the primary low-frequency *noise floors* for future third-generation observatories, such as the **Einstein Telescope (ET)** [9].

The thesis is structured as follows:

- **Chapter 1**: Provides the theoretical framework concerning the generation, propagation, and interaction of gravitational waves, with a specific focus on the response of Michelson interferometers.

- **Chapter 2**: Introduces the concept of the sensitivity curve and analyzes the primary noise sources (fundamental and technical) that limit interferometer performance.

- **Chapter 3**: Outlines the state of the art in the study and mitigation of electromagnetic noise, highlighting the growing discrepancy between the estimated impact of such noise and currently implemented strategies. The methodologies adopted during this research are also presented.

- **Chapter 4**: Develops a comprehensive analysis of magnetic noise in gravitational-wave interferometers, investigating both the nature of environmental and instrumental sources and the magneto-mechanical coupling mechanisms with suspensions and test masses.

- **Chapter 5**: Examines active and passive mitigation techniques, with particular emphasis on the use of high-permeability ferromagnetic *shields*.

- **Chapter 6**: Presents the results of advanced numerical simulations aimed at quantifying the effectiveness of various shielding strategies in reducing the magnetic field and its gradient near critical components.

- **Chapter 7**: Describes the **MANET** project (*MAgnetic Noise test facility for ET*), a facility currently under development at the INFN section of Genoa. Its characteristics are described and its objectives discussed: the magnetic characterization of components for ET and the experimental validation of mitigation techniques in the presence of geometric and material non-idealities.

- **Chapter 8**: Introduces the **CALMA** project, focused on reducing magnetic coupling through the redesign of test mass actuators, proposing a complementary approach to magnetic shielding.
- **Chapter 9**: Develops an analysis of electrostatic noise in the context of gravitational wave detectors, highlighting current gaps in the modeling of charge deposition on test masses and the resulting uncertainty in the overall *noise budget*.
- **Chapter 10**: Proposes the development of an *in-situ* charge monitoring system, aimed at understanding the dynamics of charge deposition processes and defining mitigation protocols based on direct measurements.

Finally, the **Conclusion** presents the main results of this work and highlights the current limitations and gaps in the study of electromagnetic noise within the context of gravitational-wave interferometers.

Chapter 1

Gravitational Waves

In 1916, Albert Einstein first predicted the existence of gravitational waves (GWs) within the framework of his theory of General Relativity [10, 11, 12]. In this theory, Einstein established a fundamental relation between geometry and matter, expressed through the field equations:

$$G_{\mu\nu} = \frac{8\pi G}{c^4} T_{\mu\nu}, \tag{1.1}$$

where $G_{\mu\nu}$ denotes the Einstein tensor, which encodes the geometry of space-time, while $T_{\mu\nu}$ is the stress-energy tensor, describing the distribution of matter and energy in space-time.

To describe gravitational waves, one adopts a perturbative approach. Specifically, a small perturbation $h_{\mu\nu}$ is introduced on top of the flat background metric $\eta_{\mu\nu}$ (the Minkowski metric):

$$g_{\mu\nu} = \eta_{\mu\nu} + h_{\mu\nu}, \qquad |h_{\mu\nu}| \ll 1. \tag{1.2}$$

Substituting this expression into Eq. (1.1) and retaining only terms linear in $h_{\mu\nu}$, one obtains the linearized Einstein equations. By exploiting the gauge freedom and imposing the harmonic (or Lorenz) gauge condition $\partial^\mu \bar{h}_{\mu\nu} = 0$, the equations reduce to a wave equation:

$$\Box \bar{h}_{\mu\nu} = -\frac{16\pi G}{c^4} T_{\mu\nu}, \tag{1.3}$$

where $\bar{h}_{\mu\nu} = h_{\mu\nu} - \frac{1}{2}\eta_{\mu\nu} h$ is the trace-reversed perturbation.

It is worth noting that the symmetric 4×4 matrix $h_{\mu\nu}$ initially contains 10 independent components. The harmonic gauge eliminates 4 of them, leaving 6 independent components. However, further residual gauge freedom can be exploited to remove an additional 4 components, leaving only 2 independent physical degrees of freedom, which correspond to the polarizations of gravitational waves. A more detailed treatment can be found in [13].

1.1 Propagation

To study the propagation of gravitational waves, one focuses on Eq. (1.3) in vacuum ($T_{\mu\nu} = 0$):

$$\Box \bar{h}_{\mu\nu} = 0. \tag{1.4}$$

The d'Alembertian operator $\Box = -\frac{1}{c^2}\frac{\partial^2}{\partial t^2} + \nabla^2$ implies that the speed of gravitational waves is equal to the speed of light.

To isolate the physical degrees of freedom, an additional condition, known as the Transverse-Traceless (TT) gauge, is imposed:

$$h_{0\mu} = 0, \quad \partial^i h_{ij} = 0, \quad h^i{}_i = 0. \tag{1.5}$$

With this choice and assuming a gravitational wave propagating in the z direction, the solution can be written as:

$$h_{\mu\nu}^{TT}(t,z) = \begin{pmatrix} 0 & 0 & 0 & 0 \\ 0 & h_+ & h_\times & 0 \\ 0 & h_\times & -h_+ & 0 \\ 0 & 0 & 0 & 0 \end{pmatrix} \cos\left[\omega(t - z/c)\right], \tag{1.6}$$

where h_+ and $h_\times$ are the amplitudes of the *"plus"* and *"cross"* polarizations.

1.1.1 Cosmological Expansion

When gravitational waves propagate over cosmological distances, the expansion of the Universe must be taken into account. In an expanding Friedmann-Lemaître-Robertson-Walker (FLRW) universe, the distance r is replaced by the **luminosity distance** $d_L(z)$. Furthermore, the expansion "stretches" the waveform: a signal emitted with a frequency f_{source} will be detected with a redshifted frequency $f_{obs} = f_{source}/(1+z)$.

This effect also affects the mass parameters of the source. For binary systems of mass m_1 and m_2, the signal evolution is governed by the **Chirp Mass**, defined as:

$$\mathcal{M} = \frac{(m_1 m_2)^{3/5}}{(m_1 + m_2)^{1/5}}. \tag{1.7}$$

Due to cosmological expansion, we define the **chirp mass in the detector frame** as $\mathcal{M}_z = \mathcal{M}_{source}(1+z)$, meaning that sources at high redshift appear to be more massive than they actually are in their rest frame.

1.2 Generation

The generation of gravitational waves is described assuming that the source field is sufficiently weak to justify an expansion around flat spacetime. In the low-velocity limit ($v \ll c$), the radiation is dominated by the mass quadrupole moment. The general solution to Eq. (1.3) is:

$$\bar{h}_{\mu\nu}(t, \vec{x}) = \frac{4G}{c^4} \int d^3x' \frac{1}{|\vec{x} - \vec{x}\,'|} T_{\mu\nu} \left(t - \frac{|\vec{x} - \vec{x}\,'|}{c}, \vec{x}\,' \right). \tag{1.8}$$

Transforming to the TT gauge, this yields the quadrupole formula:

$$h_{ij}^{TT} \simeq \frac{1}{r} \frac{2G}{c^4} \ddot{M}_{ij}^{TT}(t - r/c) \tag{1.9}$$

where $M_{ij} = \int d^3x \, \rho(x) x_i x_j$ is the second moment of the mass distribution.

1.2.1 Binary Systems

While several astrophysical processes (such as asymmetric supernovae or pulsars) can theoretically generate gravitational waves, the most relevant sources for current ground-based detectors are **compact binary systems** consisting of binary black holes (BBH), binary neutron stars (BNS) and black hole-neutron star systems (BH-NS). To date, these are the only sources directly observed; thus, this treatment will focus on them.

As shown in Figure 1.1, the coalescence of a binary system is divided into three distinct phases:

- **Inspiral:** The objects orbit each other, losing energy and angular momentum through GW emission. The frequency and amplitude increase over time, creating a "chirp" signal. In the adiabatic limit, the frequency evolves as:

$$f_{gw}(\tau) \simeq 134 \text{ Hz} \left(\frac{1.21 M_\odot}{\mathcal{M}} \right)^{\frac{5}{8}} \left(\frac{1 \text{ s}}{\tau} \right)^{\frac{3}{8}} \tag{1.10}$$

  where τ is the time to merger.

- **Merger:** The two bodies collide and form a single perturbed object. This corresponds to the peak amplitude of the **strain**, i.e., the relative length variation produced by the GW.

- **Ringdown:** The final object settles into a stable configuration, emitting damped sinusoids (quasi-normal modes) until all perturbations are radiated away.

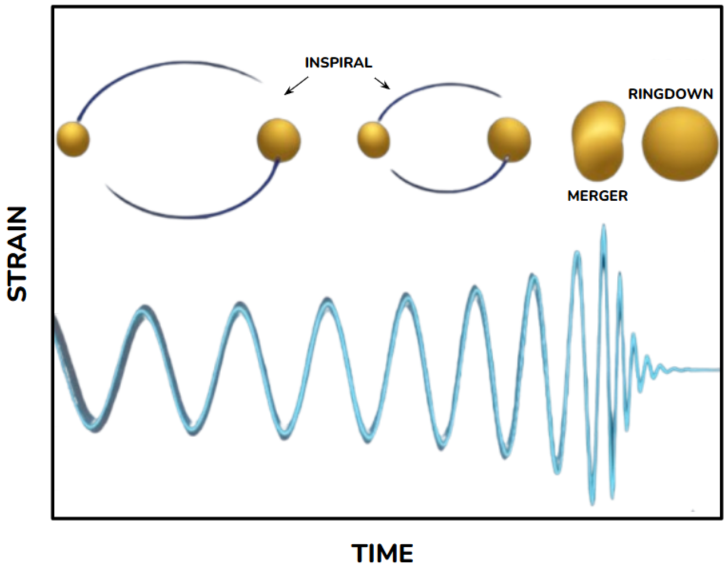

Figure 1.1: Evolution of a binary coalescence signal. The vertical axis represents the adimensionless strain h, while the horizontal axis shows the time.

1.3 Interaction

To study the effect of gravitational waves on physical objects, we consider **test masses** (TMs) in free fall. While the TT gauge is mathematically convenient, it is not the best choice for detection: in this gauge, test masses initially at rest remain at fixed coordinates.

In the laboratory frame, or **proper detector frame**, the gravitational wave manifests as a physical tidal force. The displacement ξ^i of a test mass is described by:

$$\ddot{\xi}^i = \frac{1}{2}\ddot{h}_{ij}^{TT}\xi^j. \tag{1.11}$$

This interaction is fundamentally described by the **gravitational strain** h, representing the fractional change in distance between two points: $h = \Delta L/L$. For a typical astrophysical signal reaching Earth, $h \approx 10^{-21}$. This infinitesimal strain induces a differential displacement: while one axis expands by $\delta L = hL/2$, the perpendicular one contracts, making the Michelson interferometer the ideal tool for its measurement.

1.3.1 GW Detectors

A Michelson interferometer translates the differential displacement of the test masses – the interferometer mirrors – into a phase shift $\Delta\Phi_{GW}$. To maximize the signal, the light should ideally spend a time inside the arms equal to half the GW period. This leads to an **optimal arm length** $L_{opt} = \lambda_{gw}/4 \simeq 750$ km for a 100 Hz signal, which is unfeasible on Earth.

To overcome this limitation, detectors like **Virgo** and **LIGO** integrate **Fabry-Perot cavities** within the arms. By reflecting the light multiple times, the effective optical path length is increased by a factor called the "finesse" ($\mathcal{F}$) of the cavity. Furthermore, additional "recycling" cavities (such as **Power Recycling** and **Signal Recycling**) are used to increase the circulating power and optimize the detector's bandwidth. A more detailed treatment of these optical configurations can be found in [14].

Chapter 2

Sensitivity Curve and Noise Sources

The ability of an interferometer to detect the infinitesimal strains described in Chapter 1 is limited by various noise sources. The minimum detectable signal amplitude is defined by the **sensitivity curve** (solid black line in Figure 2.1), which represents the quadratic sum of all noise spectral densities as a function of frequency:

$$S_h(f) = \sum_i S_i(f). \tag{2.1}$$

A gravitational signal with an amplitude $h(f)$ lying below this curve remains indistinguishable from the background, while a signal above it can be extracted.
In the following sections, we categorize noises into **fundamental**, which arise from the laws of physics and the nature of the apparatus, and **technical**, which depend on the detector's location and engineering.

2.1 Quantum Noise

Quantum noise is a fundamental noise which originates from the quantum nature of the laser light and the Heisenberg uncertainty principle. As discussed in Chapter 1, the use of Fabry-Perot cavities and power recycling is essential to enhance the signal; however, increasing the circulating optical power P_0 triggers a fundamental trade-off between two distinct quantum contributions: shot noise and radiation pressure noise. Their combined effect leads to a fundamental quantum limit in interferometric measurements.

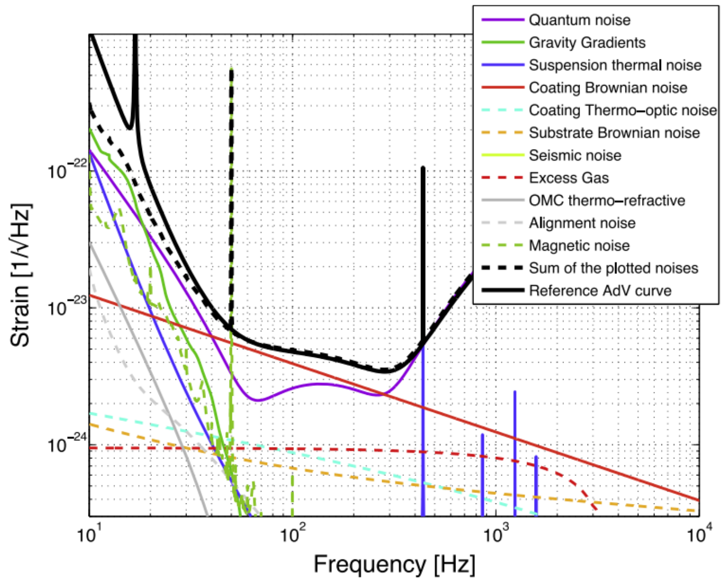

Figure 2.1: The target sensitivity of Advanced Virgo (solid black line) compared with the noise budget (dashed black line). The curve is a trade-off between fundamental limits and technical disturbances. Image reproduced from [6].

2.1.1 Shot Noise

Shot noise arises from the discrete nature of photons and corresponds to fluctuations in the number of photons arriving at the photodetector. These fluctuations translate into phase uncertainties, ultimately limiting the strain sensitivity at **high frequencies**. The shot noise contribution decreases with increasing laser power, as the relative statistical fluctuations in photon number become smaller. The associated single-sided strain noise spectral density is given by:

$$S_n^{1/2}(f)|_{\text{shot}} = \frac{1}{8L\mathcal{F}} \left(\frac{4\pi\hbar\lambda_L c}{\mathcal{C}P_0} \right)^{1/2} \sqrt{1 + (f/f_P)^2} \tag{2.2}$$

where L is the interferometer arm length, λ_L and P_0 denote the laser wavelength and input power, respectively, $\mathcal{C}$ is the power recycling gain, $\mathcal{F}$ is the finesse of the Fabry–Perot arm cavities, and f_P is their cavity pole frequency.

2.1.2 Radiation Pressure

In addition to shot noise, quantum fluctuations also manifest as radiation pressure noise. This contribution originates from the random momentum transfer exerted by photons on the test masses, leading to fluctuating displacements of the interferometer arms. Radiation pressure noise dominates at **low frequencies** and increases with laser power. The corresponding single-sided strain noise spectral density can be expressed as:

$$S_n^{1/2}(f)|_{\text{rad}} = \frac{16\sqrt{2}\mathcal{F}}{ML(2\pi f)^2}\left(\frac{\hbar\mathcal{C}P_0}{2\pi\lambda_L c}\right)^{1/2}\frac{1}{\sqrt{1+(f/f_P)^2}} \tag{2.3}$$

where M denotes the mass of each test mass.

2.1.3 The Standard Quantum Limit

The total quantum noise (purple line in Figure 2.1 and black line in Figure 2.2), also referred to as *optical read-out noise*, is obtained by summing the two contributions in quadrature:

$$S_n(f)|_{\text{opt}} = S_n(f)|_{\text{shot}} + S_n(f)|_{\text{rad}} \tag{2.4}$$

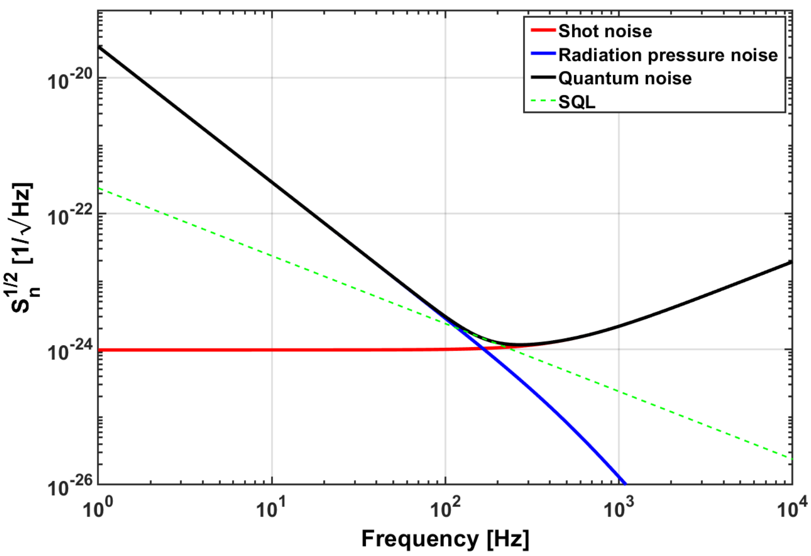

Figure 2.2: Shot noise, radiation pressure, quantum noise and SQL using parameters similar to those of Virgo ($L = 3000\ m$, $\mathcal{F} = 880$, $M = 42\ kg$).

For a fixed frequency f, one can minimize the total strain noise with respect to P_0, thus finding the lowest achievable noise at that frequency. The envelope of these minima across all frequencies defines the **Standard Quantum Limit** (SQL), which represents a fundamental quantum bound on the strain sensitivity:

$$S_{\text{SQL}}^{1/2}(f) = \sqrt{\frac{8\hbar}{M(2\pi f L)^2}} \tag{2.5}$$

By varying the laser power, the overall quantum noise curve is shifted, changing the frequency at which the detector achieves its maximum sensitivity (Figure 2.3).

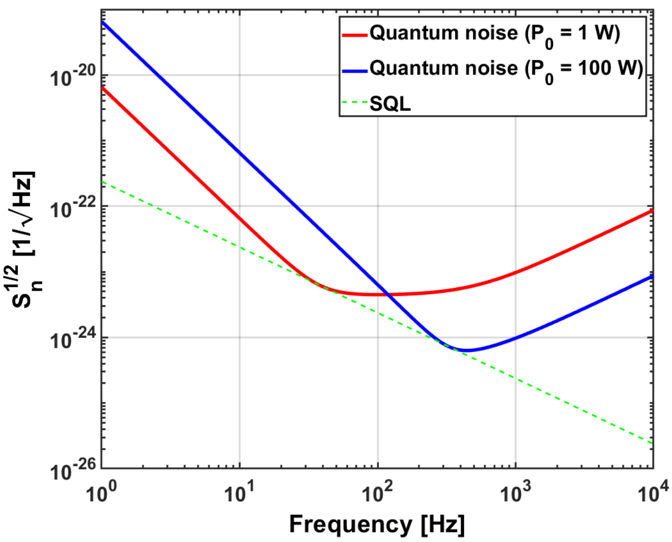

Figure 2.3: Quantum noise varying the laser output power P_0.

2.2 Displacement and Environmental Noise

Quantum noise is inherent to the detection method. However, the test masses also experience **displacement noise**, induced by external forces unrelated to gravitational waves.

2.2.1 Seismic and Newtonian Noise

Seismic noise (light green line in Figure 2.1) arises from ground vibrations, which in the frequency range 1–10 Hz are further amplified by anthropogenic activities. The corresponding spectral density is:

$$S_n^{1/2}(f)|_{\text{seismic}} = A \left(\frac{1Hz}{f^B}\right) \left(\frac{1m}{L}\right) Hz^{-1/2} \tag{2.6}$$

where L denotes the arm length, A is the noise amplitude at the reference frequency, and B characterizes the spectral slope. To mitigate this disturbance, Virgo employs the **superattenuator** (Figure 2.4) as a series of low-pass filters to suppress this noise above 1 Hz [15].

Conversely, **Newtonian noise** (dark green line in Figure 2.1) arises from local fluctuations of the gravitational field (e.g., from moving air or ground masses). Since gravity cannot be shielded, it is mitigated through active cancellation using arrays of auxiliary sensors [16].

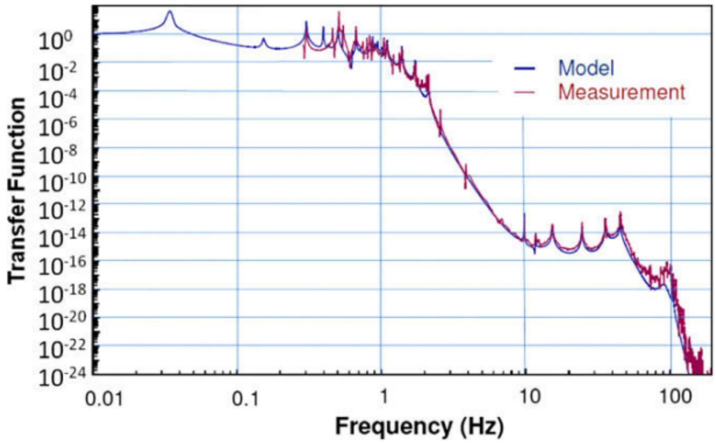

Figure 2.4: The Virgo superattenuator transfer function. Image reproduced from [15].

2.2.2 Magnetic Noise

Environmental magnetic fields (green dashed line in Figure 2.1) **arise** from the coupling between external magnetic fluctuations and the test masses or suspended optical benches. Because these fields act directly on the mirrors, they have the potential to **bypass** the mechanical isolation provided by the superattenuator. The investigation of this coupling and its mitigation through passive and active shielding **constitutes** the primary focus of the following chapters.

2.2.3 Thermal Noise

Thermal noise arises from the microscopic fluctuations of the atoms within the suspensions and the test masses. According to the **Fluctuation-Dissipation Theorem (FDT)**, every dissipative process in a system in thermal equilibrium is a source of fluctuations. The power spectral density of the thermal displacement $S_x(f)$ is related to the real part of the mechanical impedance $Z(f)$ by:

$$S_x(f) = \frac{4k_BT}{(2\pi f)^2}\text{Re}\left[\frac{1}{Z(f)}\right] \tag{2.7}$$

where k_B is the Boltzmann constant and T is the temperature. In the frequency domain, it is often more convenient to describe the dissipation through the **loss angle** $\phi(f)$, which leads to:

$$S_x(f) = \frac{4k_BTk}{(2\pi f)\left[(k - M(2\pi f)^2)^2 + k^2\phi^2(f)\right]}\phi(f) \tag{2.8}$$

where k is the elastic constant of the system. This noise manifests in two primary ways:

- **Suspension Thermal Noise (blue line in Figure 2.1):** It originates from the dissipation in the fused silica fibers used to suspend the test masses. The most prominent features are the **violin modes**: these are resonant harmonics of the suspension fibers, analogous to the vibrations of a plucked guitar string. The n-th harmonic frequency can be approximated by:

  $$f_n = \frac{n}{2L_f}\sqrt{\frac{T}{\rho}} \tag{2.9}$$

  where L_f is the fiber length, T the tension, and ρ the linear mass density. As shown in Figure 2.1, these modes appear as a forest of peaks (typically starting around 500 Hz and their harmonics). While they limit the sensitivity at specific frequencies, their narrow bandwidth allows for the search of gravitational signals in the regions between the peaks.

- **Coating Thermal Noise (red line in Figure 2.1):** Also known as Brownian Noise, it is caused by the dissipation within the thin dielectric layers that form the reflective surface of the mirrors. In the current gravitational-wave interferometers, this is a critical noise source as it limits the sensitivity in the intermediate frequency range (around 100 Hz), where the instrument is most sensitive to astrophysical signals. To mitigate these effects, the mirrors and their coatings are developed with high-quality materials (such as fused silica) characterized by extremely low loss angles ($\phi \approx 10^{-4}$ for coatings, $\phi \approx 10^{-7}$ for fibers).

Chapter 3

The Electromagnetic Challenge

This chapter delineates the theoretical and experimental framework concerning electromagnetic noise in gravitational-wave detectors. Following a bibliometric analysis that highlights a **notable lack of specialized literature** compared to other **noise sources**, the discussion traces the historical evolution and the growing impact of this disturbance in ground-based detectors. Finally, the **numerical modeling methodology** adopted in this work for the investigation and mitigation of such noise is presented.

3.1 A Bibliometric Lacuna

A systematic search conducted on the **Scopus** database at the end of 2025 reveals a marked disproportion in the scientific relevance attributed to various noise contributions within the international community. Out of a total of 42 147 publications indexed in the field, only 23 works specifically focused on **magnetic noise** were identified. This value is limited when compared to the literature on other noise sources, where the volume of publications is orders of magnitude higher:

- **Thermal Noise:** 648 publications;
- **Quantum Noise:** 601 publications;
- **Seismic Noise:** 209 publications;
- **Newtonian Noise:** 81 publications.

This gap is even more significant when considering **surface charge deposition**. In this field, scientific publications are almost entirely absent, and knowledge is preserved almost exclusively in the form of internal Technical

Reports within scientific collaborations.

Supporting this evidence, it is observed that for this specific source, it is currently impossible to perform a unique keyword-based search due to the lack of a universally accepted nomenclature. Terms such as “electrostatic noise” – which will be systematically adopted in this work – do not yet enjoy standardized recognition in academic search engines. A targeted search reveals barely a dozen scientific articles dealing with electrostatic disturbance in the context of gravitational-wave detectors, confirming the existence of a profound knowledge and instrumental gap that this thesis aims to address.

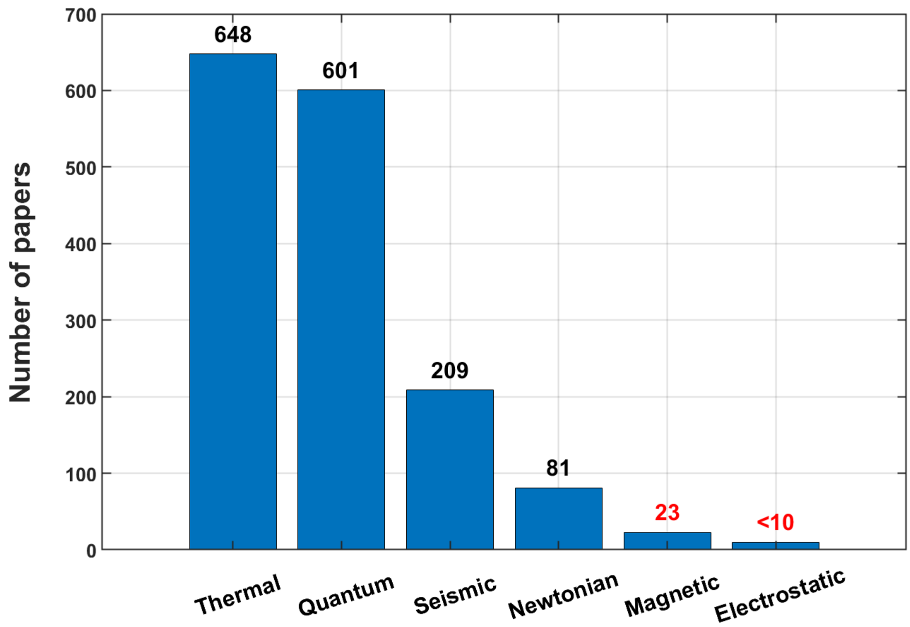

Figure 3.1: Bibliometric analysis from Scopus data (end of 2025).

3.2 State of the Art

Gravitational-wave detectors, both terrestrial and space-based, are extremely sensitive measurement instruments designed to detect relative length variations (strain) on the order of 10^{-21} or lower. At these levels of sensitivity, numerous environmental and instrumental noise sources can couple to the signal of interest and limit performance.

Historically, attention has primarily focused on seismic, thermal, and quantum noise, while magnetic noise was long considered a secondary source and, consequently, less systematically investigated.

With the progressive increase in interferometer sensitivity and the expansion of the LIGO-Virgo-KAGRA scientific program, the importance of magnetic noise has grown significantly. It has emerged that such noise can couple to the strain signal through various instrumental and environmental mechanisms, manifesting both as local noise and as globally correlated noise between detectors separated by thousands of kilometers.

The following section traces the historical evolution of magnetic noise studies in gravitational-wave detectors, starting from early works in the context of space missions, moving through characterization in second-generation terrestrial detectors – with particular focus on Virgo – and concluding with the implications for future third-generation interferometers.

The subsequent section then addresses the noise related to surface charge accumulation on the TMs, which represents an even less explored frontier. Unlike magnetic noise, whose sources and coupling mechanisms are characterized and monitored, electrostatic charge on test masses has historically been treated as an intermittent disturbance that is difficult to observe directly. The scientific literature of the last thirty years reflects a predominantly reactive approach, focused on post-hoc mitigation rather than real-time diagnostics, a critical gap which this work aims to bridge.

3.2.1 Magnetic Noise in GW interferometers

Magnetic noise has been recognized as a relevant source since the early design phases of space-based gravitational detectors. In the work of Hanson et al. [17], dedicated to the ST-7 gravitational sensor for the Disturbance Reduction System, it is shown how the interaction between the permanent magnetic moment of the test mass and the magnetic fields generated by the spacecraft electronics introduces a non-negligible contribution to acceleration noise. In particular, a noise source associated with the interaction between time-varying magnetic field gradients and the test mass's magnetic dipole is identified and included in the noise budget.

These issues were experimentally addressed in the LISA Pathfinder mission, as reported by Díaz et al. [18]. This work describes the in-flight characterization of the test masses' magnetic properties using a dedicated diagnostic system based on coils capable of generating controlled magnetic fields. The results show how magnetic susceptibility and residual magnetic moment contribute to acceleration noise and how their estimation is essential for evaluating the total magnetic noise contribution.

Subsequent studies, focused on test mass optimization and magnetic noise characterization for future space missions, are presented in Huang et al. [19] and Xu et al. [20], while Maria-Moreno et al. [21] discuss magnetic noise simulation and subtraction techniques for orbiting demonstrators. Collectively, these works demonstrate that the problem of magnetic noise is intrinsic to gravitational-wave detection from its origins, regardless of the operating environment.

In terrestrial detectors, magnetic noise couples to the strain signal through different mechanisms compared to the space-based case, due to the presence of mechanical structures, suspensions, and actuation systems. A systematic analysis of these effects is presented by Effler et al. [22], in the context of the sixth LIGO science run (S6).

This work identifies the dominant coupling mechanism as the interaction between environmental magnetic fields and the magnets used in the coil-magnet actuators of the suspended optics. Although the alternating magnet configuration reduces sensitivity to uniform magnetic fields, magnetic field gradients comparable to those produced by the actuation coils can introduce measurable displacements of the test masses, directly observable in the detector signal.

To quantify such couplings, the concept of magnetic injection is systematically introduced – an experimental technique based on the controlled generation of magnetic fields and the measurement of the detector's response. This approach has become a standard tool for characterizing magnetic noise in second-generation terrestrial detectors.

A fundamental conceptual advancement in the study of magnetic noise is represented by the recognition of globally correlated magnetic fields, particularly those associated with Schumann resonances [23, 24]. Thrane et al. [25] reported the first direct measurements of correlated magnetic noise between the LIGO and Virgo sites, showing that such correlations can introduce a systematic limit to searches for the stochastic gravitational-wave background.

In addition to the continuous contribution associated with Schumann resonances, magnetic noise can manifest as short-duration transients. Kowalska et al. [26] report observations of globally coherent magnetic transients attributed to atmospheric phenomena, occurring at a rate of several events per day. Such transients can produce test mass displacements on the order of 10^{-18} m, making them potentially relevant for both second and third-generation detectors.

These events represent a risk not only for stochastic background searches but also for the analysis of transient astrophysical signals, such as binary black hole and neutron star coalescences (BBH, BNS, BH-NS). The need to exclude magnetic contamination is clearly documented in the LIGO and

Virgo Scientific Collaboration's work on the first gravitational-wave detection, GW150914 [27].

In the context of Advanced Virgo, magnetic noise has been the subject of dedicated numerical and experimental studies. Cirone et al. [28] investigated the magnetic coupling of the Input Mirror Payload (IMP) through finite element (FE) simulations validated experimentally, showing that the magnetic noise contribution to sensitivity is currently limited but potentially relevant upon reaching design sensitivity.

These studies were experimentally extended in Cirone et al. [29], where magnetic injection campaigns allowed for the direct measurement of the coupling between the environmental magnetic field and the strain signal. During the third observing run, Fiori et al. [30] demonstrated how magnetic injections have become an operational tool for locating anomalous couplings and characterizing environmental noise.

Overall, the results obtained during the observing runs of second-generation detectors indicate that magnetic noise does not currently limit interferometer sensitivity. However, numerous works agree in predicting that it will become an increasingly relevant factor as these detectors operate stably at design sensitivity and, above all, for third-generation detectors such as the Einstein Telescope (ET) and the Cosmic Explorer [31, 32]. In this framework, the present thesis finds its place: its primary objective is to provide a comprehensive treatment of magnetic noise and its associated mitigation techniques, aiming to elevate the characterization of this source to the same level of scientific prominence as the noise sources more extensively studied within the gravitational-wave community.

3.2.2 Electrostatic Noise in GW interferometers

While magnetic noise occupies a relatively marginal role in the existing literature compared to fundamental noise sources, the study of **surface charge accumulation** represents an even more neglected frontier. If the former has at least benefited from the development of standardized monitoring protocols, electrostatic charging has historically been treated as an intermittent, almost "invisible" disturbance. This has led to a research landscape characterized by sporadic interventions rather than systematic investigation.

The first investigations into this phenomenon date back to the late 1990s and addressed the degradation of the quality factor (Q) of the suspensions. Specifically, Rowan et al. [33] and Mortonson et al. [34] demonstrated that charge accumulation on fused silica substrates not only introduces direct dissipative forces but also acts as an attractor for microscopic dust particles, causing rubbing friction noise that limits the mechanical performance of the system.

With the advent of second-generation detectors, the focus shifted to the stability of interferometric control. The introduction of electrostatic drives (ESDs) in LIGO established a critical coupling channel; Hewitson et al. [35] and Prokhorov et al. [36] highlighted how the charge present on the mass can distort actuation fields, leading to spurious test mass displacements.

In Europe, the issue emerged prominently during the third observation run of **Virgo**. Although the interferometer does not utilize ESDs, evidence of environmental electrostatic noise was confirmed. Fiori et al. [30] and the subsequent noise budget by Acernese et al. [37] identified couplings between the experimental hall's electromagnetic environment and the test masses, where deposited charge acts as a transducer for fluctuations in surrounding electric potentials.

However, the approach adopted in Virgo underscores a significant methodological limitation. Rather than a continuous diagnostic process, the test mass charge was measured only in a single, isolated instance using the magnetic actuation coils as the electrodes of a makeshift capacitor [38]. Crucially, the accumulated charge was not removed; instead, the intervention was limited to improving the grounding of the surrounding metallic structures to stabilize fluctuating potentials. While this successfully masked the noise in the detector's strain signal, it effectively left the root cause – the surface charge – unaddressed and unmonitored. Furthermore, no systematic investigation into the physical origin of the charge deposition was conducted. Ugolini et al. [39] and Mitrofanov et al. [40] attributed potential deposition mechanisms to triboelectric effects during *venting* or *pump-down* cycles, or to cosmic ray bombardment. However, these remain essentially unverified hypotheses.

The current state-of-the-art analysis reveals a significant methodological gap: while the community has mastered sophisticated discharge techniques (e.g., UV, ion flows, or electron beams [41, 42]), it currently lacks a non-invasive diagnostic tool capable of determining the spatial distribution and temporal evolution of the charge. Specifically, the limitations of the current paradigm can be summarized as follows:

1. **Absence of Online Operability:** Current measurement techniques require the interruption of scientific data acquisition, precluding dynamic control during observation runs.

2. **Lack of Spatial Resolution:** The literature conventionally treats charge as a global scalar quantity, ignoring the complex, localized na-

ture of surface charge deposition.

3. **Undetermined Deposition Origins:** The absence of continuous, high-fidelity monitoring prevents the correlation of deposition events with specific environmental or instrumental triggers.

This thesis aims to bridge this gap through the development of an innovative electrostatic monitoring system, designed to provide real-time, continuous, and spatially-resolved diagnostic data.

3.3 Numerical Modeling Methodology

The geometric and structural complexity of the systems analyzed in the subsequent chapters makes the use of analytical solutions extremely burdensome and, in many cases, impractical. For an accurate analysis of the phenomena involved, it was necessary to implement advanced numerical models based on the finite element (FE) software **COMSOL Multiphysics** [43].
The software's modular architecture allowed for addressing problems of different physical natures, tailoring the tool to the specific needs of each **experimental configuration**:

- **AC/DC Module:** employed for the study and mitigation of magnetic noise in Chapters 5 and 6, and for the **optimization of geometric and electrical parameters** of the MANET facility in Chapter 7. The same module was used for the modeling of electric fields in Chapter 10.

- **Heat Transfer Module:** used in Chapter 7 to model heat propagation produced by the Joule effect from the coils. This analysis was crucial for evaluating the thermal profile of the host structure and guided **material selection**, ensuring system stability under thermal load.

Depending on the nature of the problem, two different geometric modeling strategies were adopted. In some cases, such as for the monitoring system, the process involved importing and *de-featuring* complex CAD geometries. In others, such as for the study of magnetic shielding, a strategy of **increasing complexity** was adopted: starting from elementary analytical geometries (cylinders), the model was progressively refined by including apertures and structural details (arms, viewports).

This methodological approach allowed for optimal control over the subsequent **discretization of the domain** (*meshing*), adapting it to the specificities of each model to balance accuracy of results and computational costs.

Given the geometric complexity of the analyzed systems and the need to accurately model interactions in the surrounding air volumes, free tetrahedral elements were employed.

Although for components with regular geometries, such as the cylindrical test mass, structured meshes could be adopted, the uniformity of tetrahedral elements was maintained to ensure a smoother transition between different domains and better management of complex interfaces. To ensure high resolution in regions of interest, a **mesh refinement** strategy was implemented: mesh density was significantly increased near sensitive areas. This approach proved essential for ensuring the accuracy of magnetic flux and electric potential calculations within the volume occupied by the test mass. Conversely, in more distant areas or external air volumes, a coarser mesh was maintained to favor stable calculation convergence and reduce computation time (Figure 3.2).

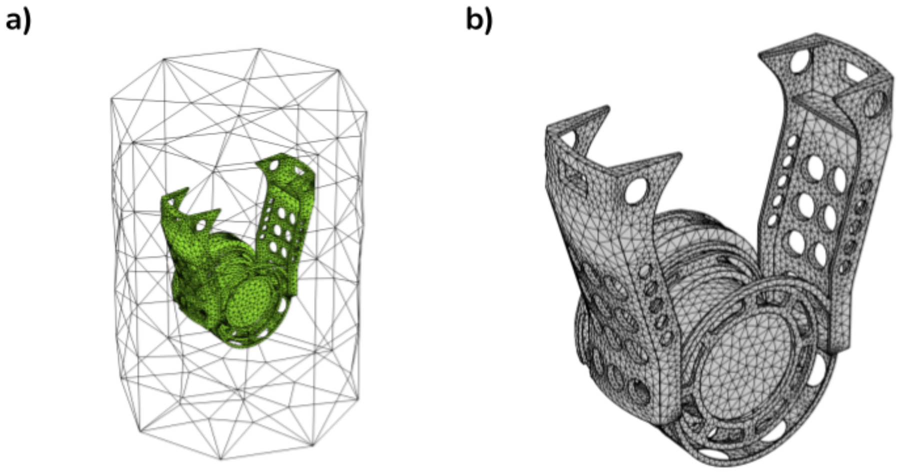

Figure 3.2: Visualization of the finite element mesh discretization strategy. a) Global view of the entire simulation domain: the coarser tetrahedral mesh applied to the surrounding air volume is visible to optimize computational cost, while the higher element density at internal components can be discerned. b) Detailed view focused on the central assembly (test mass, cage, and supports), highlighting the high level of local refinement adopted to accurately capture complex geometries and critical regions.

Chapter 4

Magnetic Noise

The term **magnetic noise** is somewhat misleading. In contrast to other noise sources, such as quantum or thermal noise, which are intrinsic to the interferometer, magnetic noise **originates** primarily **from the interaction between external magnetic fields and specific components of the detector**. In the absence of such coupling mechanisms, magnetic noise would be negligible, even in the presence of strong and fluctuating ambient magnetic fields.

A comprehensive study of magnetic noise therefore requires an investigation of both the sources of magnetic fields and the interferometer subsystems that are susceptible to them, together with a characterization of the physical mechanisms responsible for the coupling.

As seen in Chapter 3, at present in the Virgo interferometer, magnetic noise does not represent a dominant contribution to the overall noise budget, being overshadowed by other sources [30]. Nevertheless, it cannot be ignored because of the strong coupling between external magnetic fields and the test masses (TMs), each of which carries four permanent magnets for precision actuation and control [28].

Looking ahead, **in the Einstein Telescope** (ET) interferometer, magnetic noise is anticipated to constitute **one of the principal limitations to sensitivity** at low frequencies (1–100 Hz), together with Newtonian noise [44].

4.1 Magnetic Noise Sources

Magnetic noise can be broadly classified into two categories: natural magnetic noise and so-called self-inflicted or anthropogenic magnetic noise, which originates from human activity.

The dominant source of **natural magnetic noise is represented by the Schumann resonances** (SRs) [23, 24], ultra-low frequency electromagnetic waves (fundamental frequency at $\sim 7.83\,\mathrm{Hz}$ with higher harmonics) that are established within the resonant cavity formed between the Earth's surface and the ionosphere.

These resonances are primarily excited by lightning discharges, which generate electromagnetic pulses propagating around the Earth and reflecting multiple times between the ground and the ionosphere. Whenever the wavelength of these waves matches the dimensions of the cavity, a resonance condition is fulfilled, giving rise to the Schumann modes (Figure 4.1).

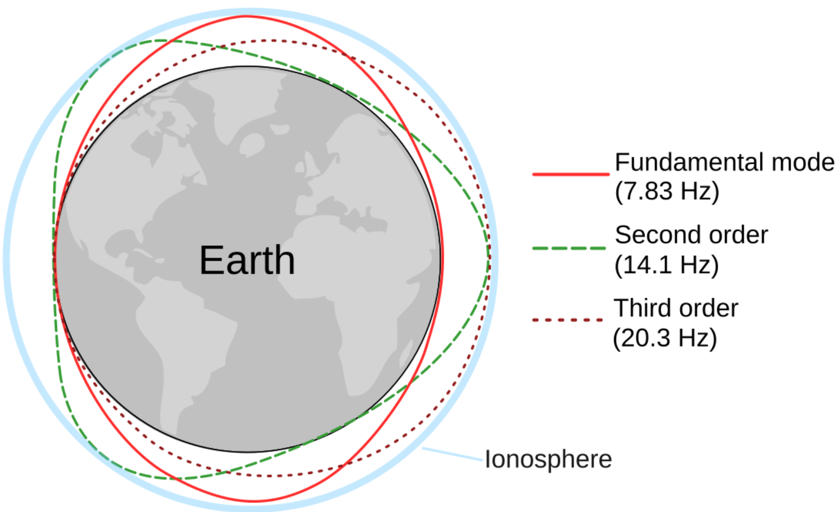

Figure 4.1: Sketch of Schumann resonances in Earth's atmosphere. Reproduced from [45].

Due to their coherence over continental scales, Schumann resonances constitute a correlated noise source for the global network of gravitational-wave detectors. Their typical amplitude is of the order of $1\,\mathrm{pT}/\sqrt{\mathrm{Hz}}$.

Experimental measurements at KAGRA have shown that the amplitude of the Schumann resonance in the X-direction is larger inside the underground tunnel compared to the external environment (Figure 4.2). Such an effect was not observed at the Sos Enattos site in Sardinia, where no amplification between surface and underground measurements was detected (Figure 4.3).

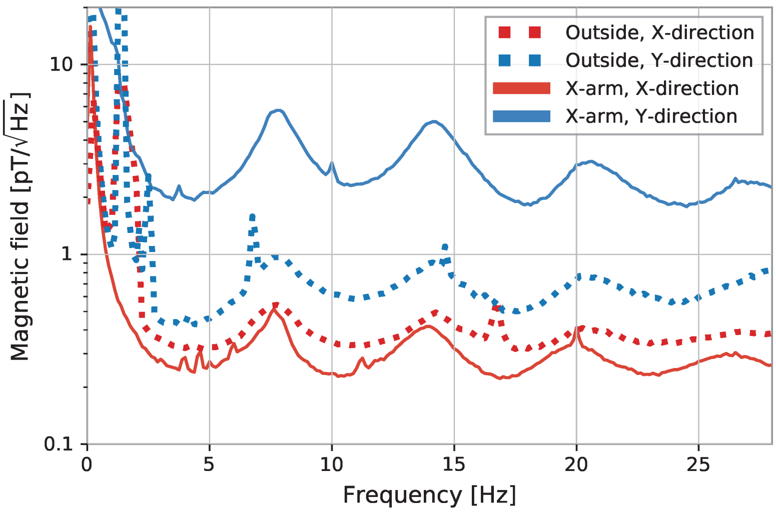

Figure 4.2: Amplitude spectral density of the Schumann resonances measured outside (dashed) and inside the KAGRA X-arm tunnel (solid). Red/blue correspond to the X/Y-arm directions. Image reproduced from [46].

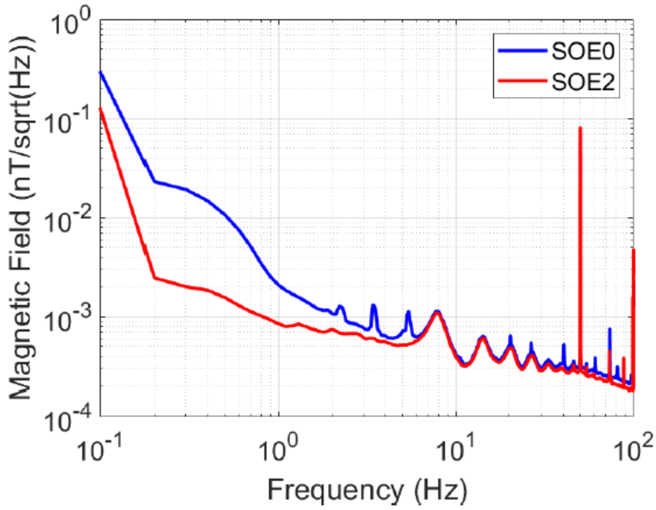

Figure 4.3: Amplitude spectral density of Schumann resonances at the Sos Enattos site in Sardinia, comparing surface (blue) and underground (red) measurements. Image reproduced from [47].

Despite the relevance of Schumann resonances, the **dominant contribution to magnetic noise** in current interferometers **is of anthropogenic origin**. In particular, the electromagnetic fields generated by the detector's own infrastructure – including power cables, control electronics, and auxiliary devices – constitute the largest fraction of the magnetic noise budget.

At Virgo, for instance, measurements in the central building show that Schumann resonances are almost completely obscured by local self-inflicted noise (Figure 4.4). Schumann resonances remain detectable in particularly quiet environments, however their amplitude often appears enhanced due to the interferometer's own contribution (Figure 4.5).

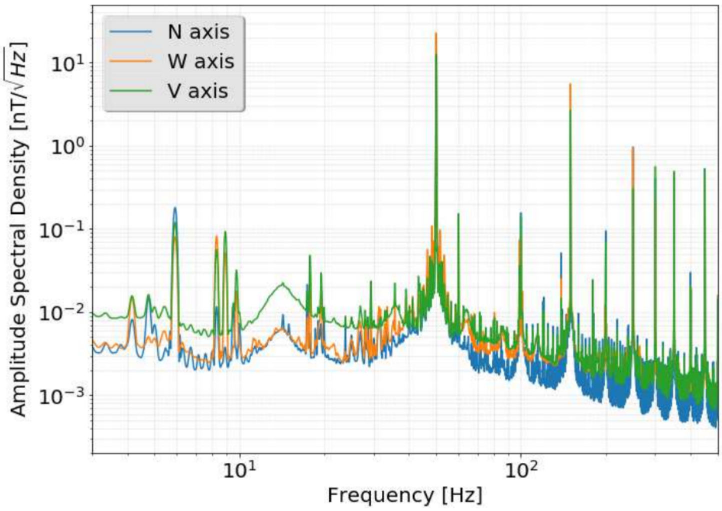

Figure 4.4: Amplitude spectral density of magnetic fields measured at Virgo Central Building. N, W, and V denote North–South, West–East, and Vertical directions, respectively. Image reproduced from [29].

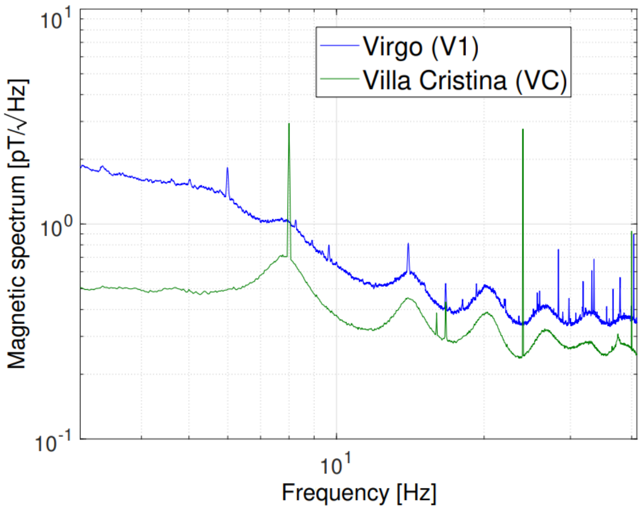

Figure 4.5: Comparison of Schumann resonance amplitudes measured at a low-noise site within Virgo and at Villa Cristina, located about 13 km away. Image reproduced from [48].

4.2 Magnetic Noise Coupling

Magnetic noise arises from the interaction between external magnetic fields and the interferometer components sensitive to such fluctuations. These sensitive elements include the magnetic anti-springs (Figure 4.6) of the Superattenuator (SA) and the magnets within the coil-magnet actuation system of both the SA and the TM (Figure 4.7) [49].

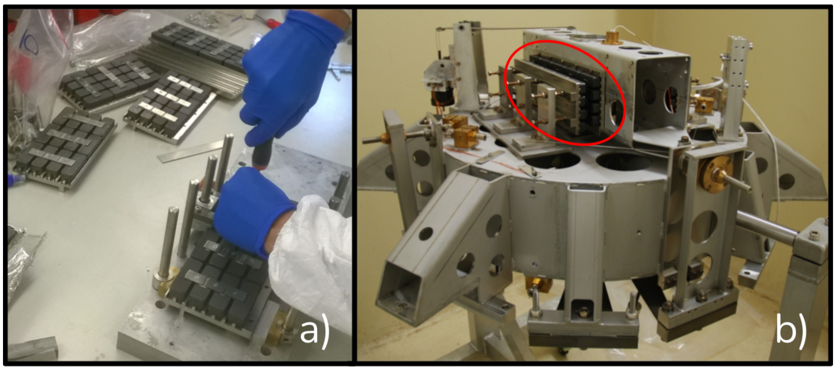

Figure 4.6: Magnetic anti-springs assembly. (a) Manual assembly of the permanent magnets (black parallelepipeds) onto the titanium plates at the Virgo site. (b) The two magnet arrays installed in the Filter 0 of the Superattenuator are highlighted by the red circle. Images reproduced from [50, 51].

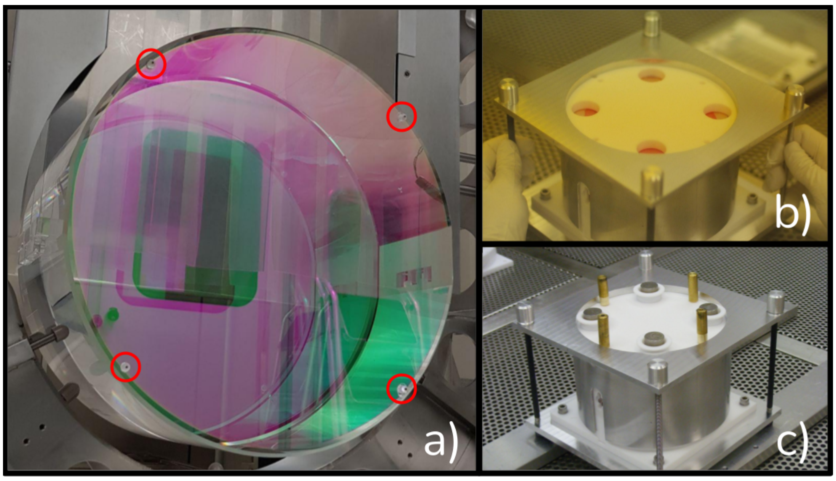

Figure 4.7: Preparation and bonding of magnets on the optics. (a) Detail of the North End (NE) Test Mass with four glued magnets (highlighted by red circles). (b-c) Assembly phases on the Input Mode Cleaner (IMC) Test Mass: (b) positioning of the spacer to ensure millimetric alignment; (c) final bonding of the magnets. Images reproduced from [52, 53].

The most critical coupling is that involving the permanent magnets on the Test Masses, as it results in a direct force acting on the mirror's displacement. Characterizing and mitigating this interaction is a pivotal challenge for the detector's sensitivity and is currently an active research topic within the Virgo Collaboration [30]. In particular, in Virgo, a uniform magnetic field is injected for each test mass and the interferometer response is measured. From this, the ***Coupling Function*** (CF) is calculated as:

$$\mathrm{CF}(f) = \sqrt{\frac{X_{inj}^2 - X_{bkg}^2}{B_{inj}^2 - B_{bkg}^2}} \tag{4.1}$$

where X represents the Amplitude Spectral Density (ASD) of the interferometer channel Hrec, B is the ASD measured by a magnetometer located near the corresponding test mass, and the subscript "bkg" refers to the background condition without injections (Figure 4.8).

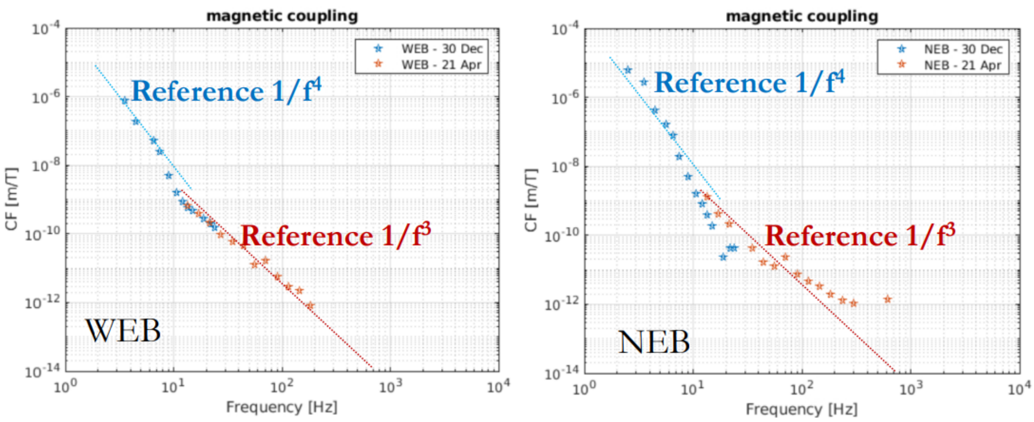

Figure 4.8: Coupling Function for two different Virgo test masses: one located in the west-end building and the other in the north-end building. Image reproduced from [54].

Considering the interferometer arm length L, the magnetic noise contribution from each test mass can be estimated by multiplying its Coupling Function by the measured magnetic field in the vicinity of the mass:

$$h_{MAG}^{(i)}(f) = \frac{1}{L}\mathrm{CF}^{(i)}(f) \cdot B^{(i)}(f) \tag{4.2}$$

The overall magnetic noise for the interferometer is then obtained by summing the contributions from all test masses in quadrature:

$$h_{MAG}(f) = \sqrt{\sum_{i=1}^{4} \left[h_{MAG}^{(i)}(f)\right]^2} \tag{4.3}$$

4.3 Magnetic Noise Budget in the Einstein Telescope

For the Einstein Telescope (ET), the Coupling Function of its test masses is not yet available. Therefore, the CF is estimated from Virgo measurements [29], assuming that the coupling mechanism remains unchanged and accounting for differences in test mass. Specifically:

$$\mathrm{CF}_{ET} \simeq \frac{m_{Virgo}}{m_{ET}} \mathrm{CF}_{Virgo} \tag{4.4}$$

Figure 4.9 shows an estimated low-frequency noise budget for ET, including the contribution from natural magnetic noise calculated as described above. It is clear how, without adequate mitigation, natural magnetic noise alone could exceed the maximum allowed level to reach the ET target sensitivity.

The situation becomes more critical when considering self-inflicted magnetic noise (Figure 4.10). Assuming an ASD comparable to that measured at Virgo, the anthropogenic magnetic noise for ET is expected to be approximately two orders of magnitude above the maximum permissible level [55].

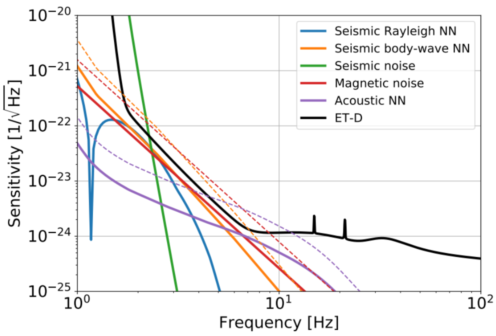

Figure 4.9: Example of an ET environmental-noise budget together with the ET sensitivity model. Dashed lines indicate noise levels without the required additional mitigation (factor 3). Image reproduced from [44].

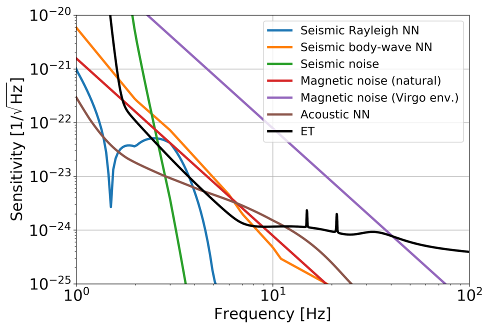

Figure 4.10: ET environmental-noise budget without mitigation. The self-inflicted magnetic noise (purple line) was estimated from Virgo environmental magnetic noise measurements. Image reproduced from [55].

Chapter 5

Magnetic Noise Mitigation

As discussed in Chapter 4, if not properly mitigated, magnetic noise can significantly constrain the sensitivity of current gravitational-wave interferometers beyond the O5 run and is expected to constitute a critical obstacle for future detectors, such as the Einstein Telescope.

The mitigation of magnetic noise can be approached through a threefold strategy:

- Attenuation of the magnetic field source (when the source is known and localized);
- Mitigation of the magnetic field in the vicinity of interferometer components that are particularly sensitive to external disturbances (e.g. test mass towers);
- Reduction of the magnetic coupling factor.

The first two strategies can be implemented using mitigation techniques designed to shield, redirect, or compensate for the magnetic field responsible for the noise. In this context, the ***Shielding Factor*** (SF) is defined as the **ratio between the magnetic flux before and after the implementation of a mitigation system**:

$$SF = \frac{\Phi_S(B_0)}{\Phi_S(B)} \tag{5.1}$$

where B_0 and B are the magnetic fields before and after applying the magnetic shielding technique, respectively. The surface S is the area through which the flux is calculated: for a source to be mitigated, it represents the outgoing flux (Figure 5.1-a); for a region to be shielded, it represents the incoming flux (Figure 5.1-b).

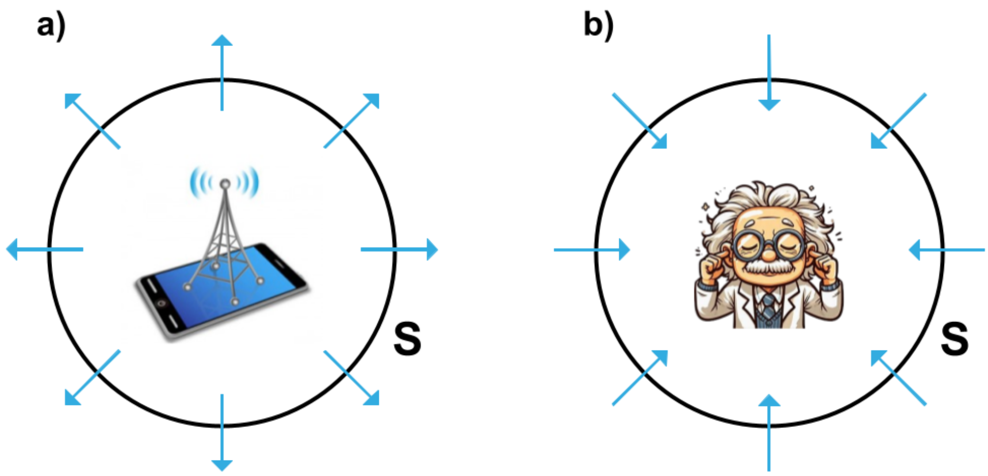

Figure 5.1: Schematic representation of magnetic shielding scenarios: a) outgoing flux from a source to be mitigated; b) incoming flux in a region to be shielded.

While the flux-based SF provides an integrated measure of the mitigation effectiveness over a volume, it is often necessary to evaluate the performance at specific locations. To this end, we also define a **pointwise Shielding Factor** $SF_{(P)}$, as the ratio of the magnetic flux density magnitudes at a given point P:

$$SF_{(P)} = \frac{|\vec{B}_0(P)|}{|\vec{B}(P)|} \tag{5.2}$$

This local parameter is particularly useful in FEM simulations to identify potential field leakages. With this definition, a value of $SF_{(P)} = 1$ indicates no attenuation, while values $SF_{(P)} > 1$ represent an effective reduction of the magnetic field.

The third strategy can be implemented by redesigning the magnetic actuators used in ground-based interferometers – a topic reserved for an in-depth discussion in Chapter 8.

Technical solutions available for shielding and compensating external magnetic fields are categorized into two primary domains:

- **Passive techniques**: Self-sustaining and requiring no external power, such as high-permeability ferromagnetic shields and eddy-currents.
- **Active techniques**: Requiring power supplies, control circuitry, and potentially specific environmental conditions (e.g., cryogenic temperatures), such as adaptive currents and superconducting shields.

The remainder of this chapter provides a comparative analysis of these methods, evaluating their effectiveness in reducing the magnetic field.

5.1 Ferromagnetic Shields

Ferromagnetic shields exploit the high magnetic permeability of certain materials to redirect magnetic field lines, effectively steering them away from the region to be protected (Figure 5.2).

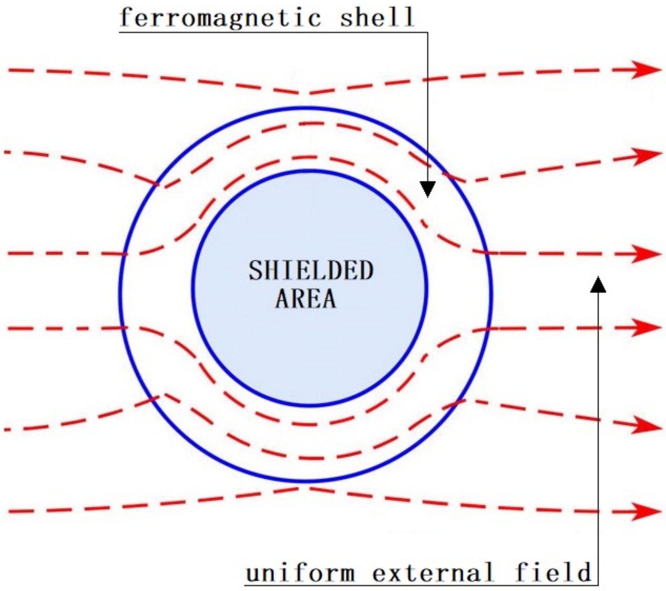

Figure 5.2: Schematic representation of the effect of a ferromagnetic shield: a central area (the region to be protected) is enclosed by a ferromagnetic shell that redirects the external magnetic field.

The materials typically used for this purpose, known as soft magnets, are characterized by extremely high magnetic permeability and an exceptionally narrow hysteresis loop - key properties that prevent residual magnetic fields (Table 5.1).

Material	**Name**	$\boldsymbol{\mu_i}$	$\boldsymbol{\mu_{max}}$	$\boldsymbol{H_c}$
Fe	iron	300	5 000	70 A/m
$Mn_xZn_{1-x}Fe_2O_4$	MnZn ferrite	4 000	20 000	20 A/m
$Ni_{77}Fe_{16.5}Cu_5Cr_{1.5}$	mu-metal	20 000	100 000	4 A/m
$Ni_{180}Fe_{15}Mo_5$	supermalloy	100 000	300 000	0.5 A/m

Table 5.1: Comparison between iron and three different soft magnets. μ_i and μ_{max} denote the initial and maximum relative permeability, respectively, while H_c represents the coercive field [56].

Among soft magnets, Fe-Ni alloys, such as mu-metal and supermalloy, exhibit the highest magnetic permeability [56]. However, an important consideration when working with these materials is their sensitivity to mechanical deformation. Even minor deformations can significantly degrade their performance. Only through annealing these alloys can recover their original properties [57, 58, 59].

The annealing process involves heating the material to a specific temperature for a defined period, followed by controlled cooling. This thermal treatment relieves internal stresses and restores the material's crystalline structure, thereby enhancing its magnetic and mechanical properties.

For Fe-Ni alloys, annealing is essential to achieve high magnetic permeability and low coercivity, both of which are compromised by mechanical deformation or improper thermal treatment (Figure 5.3)

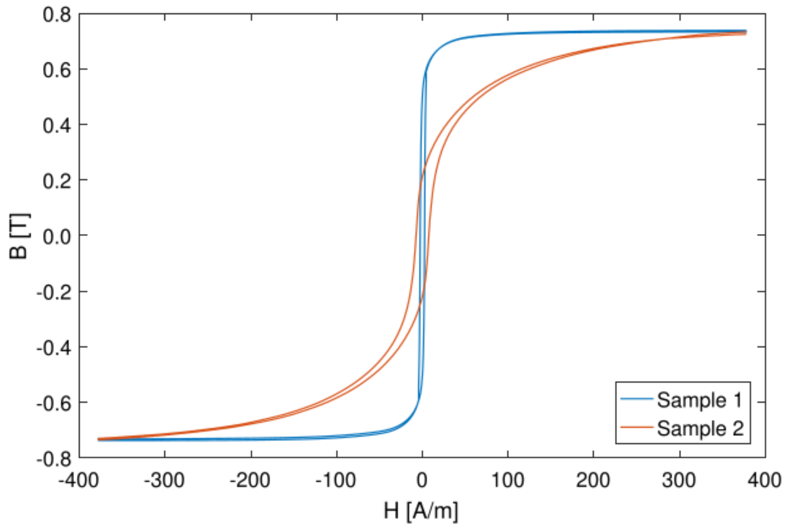

Figure 5.3: Measured DC hysteresis loops for two mu-metal samples. Sample 1 is annealed, sample 2 is unannealed. Image reproduced from [59].

In contrast, other soft magnets, such as ferrites, display greater stability and durability in their magnetic properties, albeit with lower magnetic permeability.

Ferromagnetic shields are commonly implemented using magnetically shielded rooms – large enclosures made of multiple layers of soft magnetic materials. These structures can achieve shielding factors exceeding 10^5 [60, 61]. However, in gravitational-wave interferometers, fully enclosed shields are impractical. Open surfaces required for laser beam propagation and viewports prevent the use of complete enclosures, significantly reducing the achievable shielding factor.

To provide the reader with a clear understanding of the degradation caused by such apertures, we present a **toy model** analysis. To ensure the results are representative of the implementation challenges encountered within the context of gravitational-wave detectors, the toy model is not based on arbitrary parameters but utilizes a geometry and dimensions comparable to the lower section of the Virgo test mass towers ($R_{int} = 1.015$ m, $H = 2.375$ m). This allows for a direct assessment of how the height-to-radius ratio (H/R) and the absence of end-caps affect the shielding performance in a realistic scale.

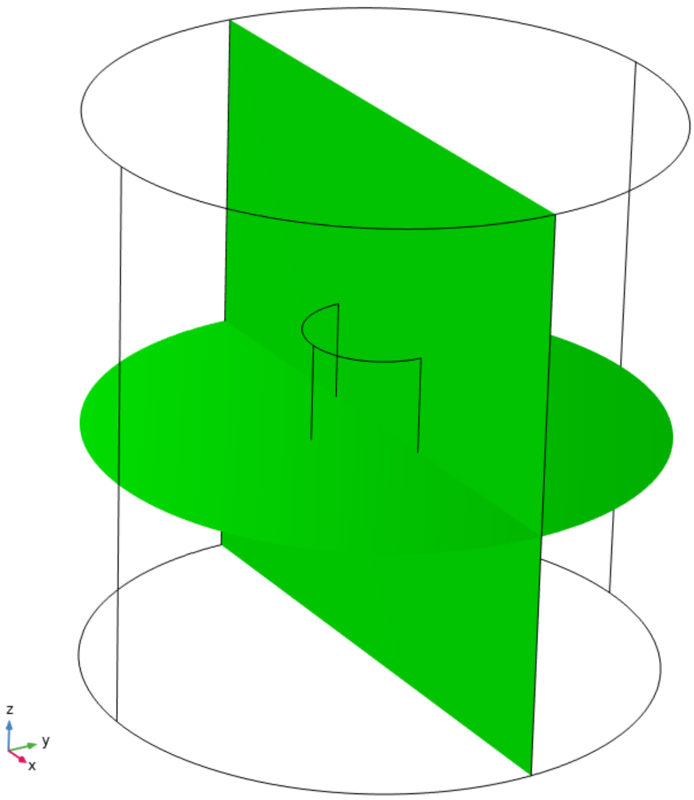

Figure 5.4: Schematic 3D representation of the toy model geometry. The green surfaces indicate the longitudinal and transverse planes used for the evaluation of the magnetic flux density B and the shielding factor SF.

The evaluation is performed on the two symmetry planes shown in Figure 5.4: a longitudinal plane passing through the cylinder axis and a transverse plane passing through its center.

The first case analyzed considers an external magnetic field directed **axially**.

Figure 5.5 compares the magnetic field distribution on the longitudinal plane for two configurations: (a) a fully enclosed cylinder and (b) an open-ended cylinder (lateral surface only). The shield consists of a 1 mm thick layer of high-permeability material ($\mu_r = 50\,000$).

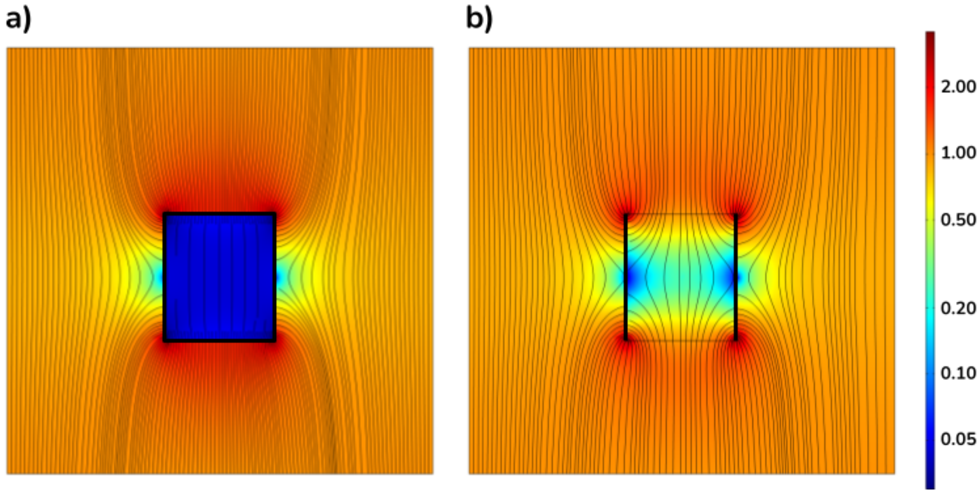

Figure 5.5: Toy model simulation (Axial Field): magnetic field distribution on a longitudinal plane. The external background field is 1 T, directed axially. (a) Ideal fully enclosed shield; (b) Realistic open-ended configuration.

The simulation highlights the "flux shunting" effect. In the closed configuration, the high-permeability wall provides a low-reluctance path that effectively channels the magnetic flux around the internal volume. Conversely, in the open toy model, the magnetic field lines "leak" through the apertures, significantly compromising the quiet zone at the center of the cylinder.

This behavior is further quantified in Figure 5.6 by the pointwise shielding factor $SF_{(P)}$. As previously defined, a value of $SF_{(P)} > 1$ indicates the effective attenuation of the external field. It should be noted that for visualization purposes, the colormap for $SF_{(P)}$ has been **lower-bounded** to a minimum value of 1. While the high-permeability material distorts the external field lines – potentially leading to $SF_{(P)} < 1$ in localized external regions due to flux compression – such effects are outside the region of interest and are thus saturated to 1 to highlight the attenuation performance within the shielded volume.

To complete the analysis, the same comparison was performed considering an external magnetic field directed **radially**, evaluated on the transverse plane identified in Figure 5.4. As shown in the field distribution (Figure 5.7) and the corresponding $SF_{(P)}$ map (Figure 5.8), the radial component is significantly better attenuated than the axial one. Even in the absence of end-caps,

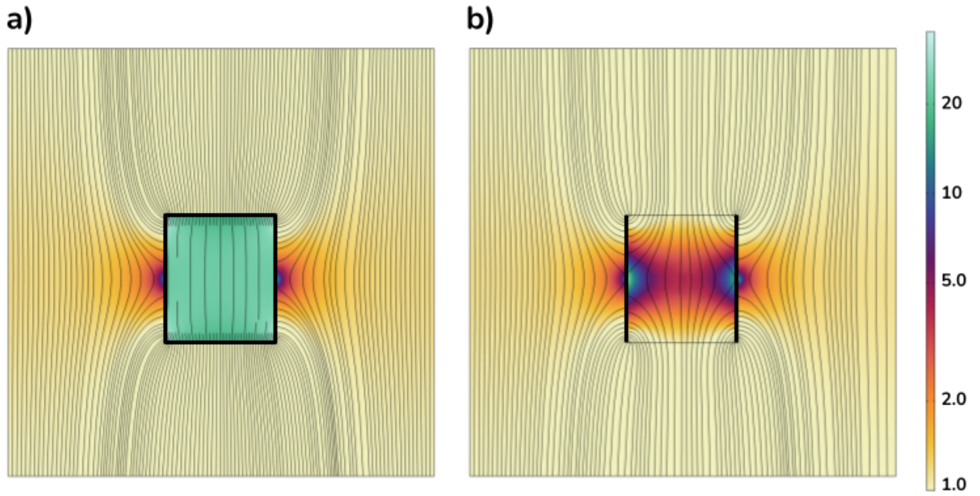

Figure 5.6: Toy model simulation (Axial Field): pointwise shielding factor $SF_{(P)}$ on the longitudinal plane. The logarithmic colormap illustrates the leakage effect through the open bases (b); values $SF_{(P)} < 1$ are saturated to 1 to focus on the attenuation ($SF_{(P)} > 1$) within the volume.

the magnetic flux can still be effectively shunted along the circumference of the cylinder.

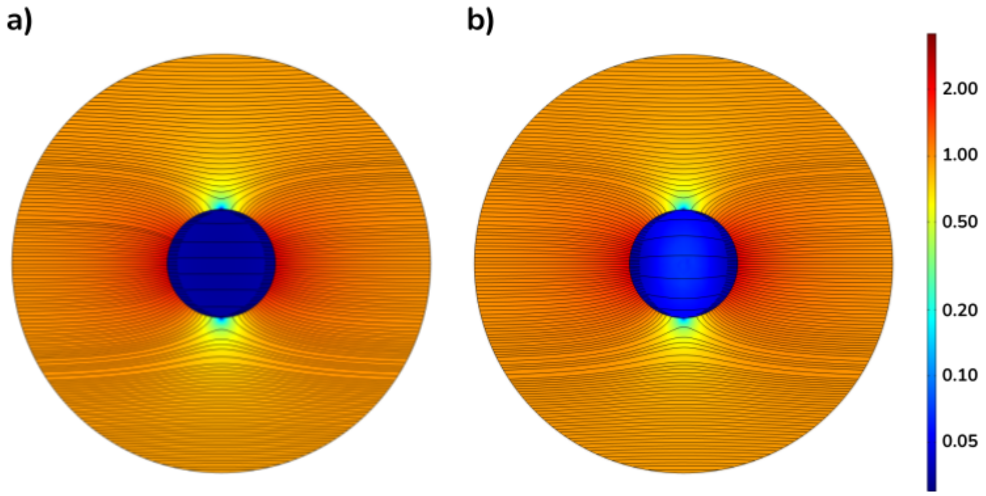

Figure 5.7: Toy model simulation (Radial Field): magnetic field distribution on a transverse plane. The external background field is 1 T, directed radially. (a) Fully enclosed shield; (b) Open-ended cylinder.

At the center of the volume, the shielding performance for a radial field remains high, with $SF_{(P)}$ values significantly greater than unity. However, these results confirm that the shielding effectiveness in open structures is highly sensitive to both the system geometry and the orientation of the external magnetic field. While an open-ended cylinder may provide sufficient mitigation for radial fields, it proves ineffective against axial components.

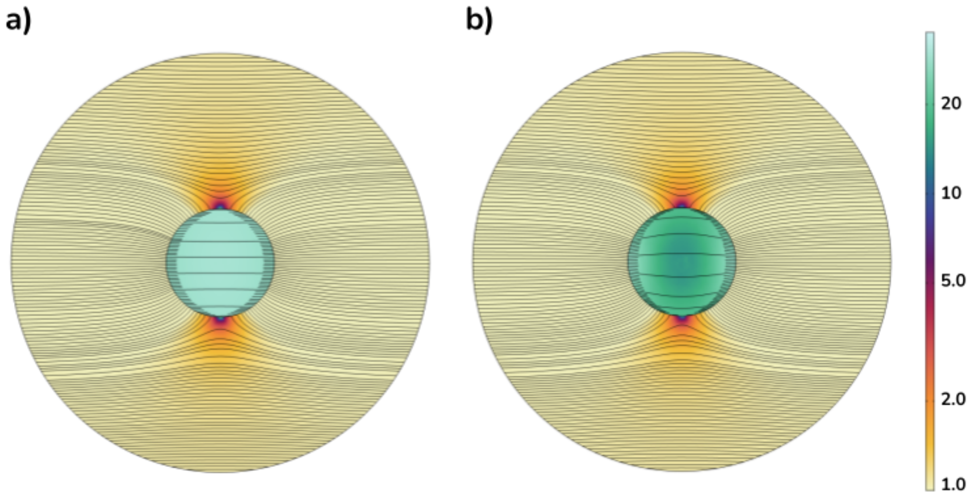

Figure 5.8: Toy model simulation (Radial Field): pointwise shielding factor $SF_{(P)}$ on the transverse mid-plane. In the open-ended cylinder (b) the attenuation is more uniform than in the previous case, reaching higher $SF_{(P)}$ values.

This anisotropy implies that a general shielding factor cannot be defined for open structures; instead, the problem must be studied *ad hoc*, accounting for the vector nature of environmental magnetic noise and the specific placement of sensitive components. While this toy model illustrates these fundamental limitations, a detailed study accounting for the specific technical apertures and features of the real Virgo towers will be presented in Chapter 6.

5.1.1 Multilayers

Ferromagnetic shields are typically built using multilayer configurations. For a given amount of material, this approach provides better performance compared to single-layer designs.

This phenomenon has been extensively studied in the literature. As early as 1892, Rücker [62] analytically solved the multilayer shielding problem for spherical symmetry. In 1897, Du Bois [63] provided a detailed treatment for bilayer configurations with spherical and cylindrical symmetry, later extended to trilayers by Wills [64].

The enhanced performance of multilayer shields can be attributed to the fact that the ability of a ferromagnetic material to redirect magnetic field lines depends not only on its bulk magnetic properties but also on the boundary conditions imposed by Maxwell's equations:

$$B_{\perp}^{1} = B_{\perp}^{2} \tag{5.3}$$

$$B_{\parallel}^{1}/\mu_{r_1} = B_{\parallel}^{2}/\mu_{r_2} \tag{5.4}$$

where $B_{1,2}$ and $\mu_{r_{1,2}}$ denote the magnetic field and relative permeability of the first and second material, respectively, at their interface.

Table 5.2 compares the results from the analytical models of Du Bois and Wills with finite element simulations for three configurations: a single spherical shell with $\mu_r = 10,000$ and thickness 3 cm; a bilayer shell with each layer 1.5 cm thick and a 0.5 cm air gap; and a trilayer shell with each layer 1 cm thick separated by two 0.5 cm air gaps.

Shielding Factor	**1-layer**	**2-layers**	**3-layers**
Analytical formulas	1211	61544	$1.77\ 10^6$
Finite element simulation	1216	62993	$1.24\ 10^6$

Table 5.2: Comparison between analytical solutions and finite element simulations for multilayered spherical shells.

Furthermore, the presence of Johnson noise makes multilayer designs preferable. Soft magnets are dissipative materials and therefore generate magnetic noise themselves [65]. This noise originates from currents within the material, known as Johnson currents [66].

Johnson currents arise from the thermal agitation of free electrons. For temperatures $T > 0$ K, thermally agitated electrons move randomly and, by colliding with atoms and other electrons, generate fluctuating current densities. These fluctuations produce local microcurrents that vary continuously in magnitude and direction [67].

While these currents occur throughout the material and constitute white noise in principle, the magnetic noise produced is dominated by low frequencies (below kHz) due to the skin effect shielding higher frequencies.

Multilayer structures mitigate Johnson noise, as the noise generated by outer layers is partially shielded by inner layers. Consequently, the dominant contribution to magnetic noise typically comes from the innermost layer [68].

The use of ferrite materials also reduces Johnson noise. Although ferrites generally have lower magnetic permeability than mu-metal or supermalloy, their much lower electrical conductivity results in significantly reduced thermal noise [69].

5.1.2 Low-Field Magnetic Permeability

Ferromagnetic materials are characterized by the presence of a hysteresis loop, which implies that their magnetic permeability is not constant but depends on both the intensity of the applied magnetic field and the magnetic history of the material [70].

In the case of soft magnetic materials, however, the hysteresis loop is extremely narrow. As a result, the magnetic behavior of the material can, in many cases, be adequately described by the initial magnetization curve alone, the so-called B-H curve. Consequently, the relative magnetic permeability can be approximated as a function of the external magnetic field only: it remains nearly constant for weak fields, increases significantly at intermediate values, and finally approaches unity as the material reaches magnetic saturation.

In the specific context of gravitational-wave detectors, as discussed in Chapter 4, the external magnetic fields of interest are on the order of nanotesla or even picotesla. Therefore, the focus lies on the magnetic permeability of materials in extremely weak-field regimes. However, the magnetic response of soft ferromagnetic materials under such low field intensities remains poorly characterized in the literature. Most available experimental data do not extend below the nanotesla range [59].

Fortunately, as previously mentioned, the fact that the magnetic permeability becomes approximately constant below a certain threshold - or equivalently that the relationship between the applied field and the induced field remains linear - makes it possible to extrapolate the permeability behavior for field strengths lower than those accessible to direct measurement. In particular, Rayleigh's law [71] describes the relationship, near the linear regime, between the magnetic field inside the material B and the magnetizing field H:

$$B = \mu_0 \mu_i H + a H^2 \tag{5.5}$$

where $\mu_0 = 4\pi\, 10^{-7}\, T\, m\,/A$, μ_i is the relative initial permeability, and a is the Rayleigh constant.

This regime has been experimentally validated in a permalloy sample in [72] (Figure 5.9).

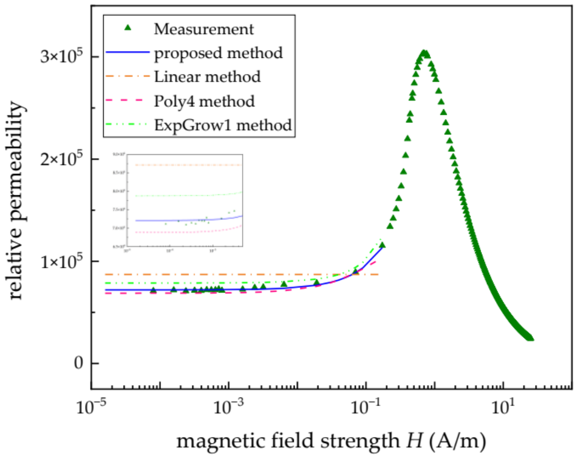

Figure 5.9: Experimental validation of Rayleigh's law (proposed method in the legend). Image reproduced from [72].

5.1.3 Magnetic Permeability Frequency Dependence.

Magnetic permeability depends not only on the intensity of the applied magnetic field but also on its oscillation frequency. This frequency dependence arises from the dynamic response of magnetic domains and eddy-current effects within the material.

In the context of gravitational-wave interferometers, since magnetic noise is most relevant at low frequencies (below 100 Hz), our interest lies in shielding external fields within this range – where, fortunately, the magnetic permeability tends to be higher. In particular, Figure 5.10 shows the relative magnetic permeability of the same mu-metal sample at different frequencies [59].

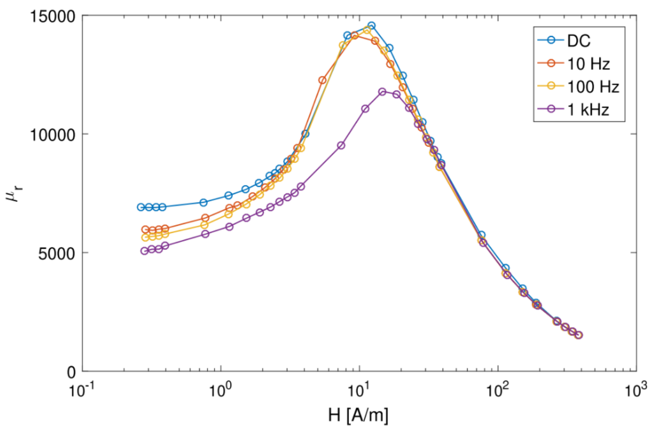

Figure 5.10: Measured relative permeability as a function of the external magnetic field, both in DC and at various frequencies. Image reproduced from [59].

5.2 Eddy Currents

Faraday's law of magnetic induction states that a variation of the magnetic flux Φ_B through a surface induces a potential difference $\mathcal{E}$:

$$\mathcal{E} = -\frac{d\Phi_B}{dt} \tag{5.6}$$

In the presence of a conductive material, this potential difference generates a current that creates a magnetic field opposing the variation of the flux. This means that if, for example, the external field is decreasing, a magnetic field will be generated in the same direction as the external field, thus limiting its decrease. Conversely, if the external magnetic field is increasing, an opposing magnetic field will be generated, limiting its growth (Figure 5.11).

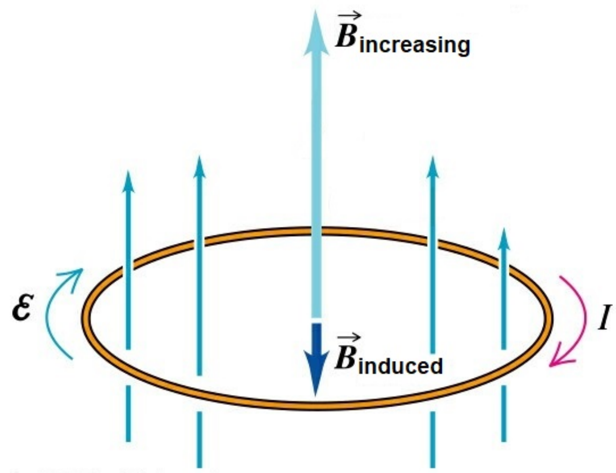

Figure 5.11: Schematic representation of a conducting loop illustrating Faraday's Law: the induced magnetic field opposes the increase in external magnetic flux.

Consequently, when an external magnetic field oscillates (e.g., a sinusoidal wave), the induced eddy currents generate a counter-acting magnetic field that opposes the change. This results in a transmitted field that oscillates at the same frequency but with a attenuated amplitude. Since the induced electromotive force is proportional to the rate of change of the magnetic flux, the shielding effectiveness is frequency-dependent: higher frequencies induce stronger currents, resulting in greater attenuation. Conversely, for static fields, the lack of time variation results in zero induced current, rendering this shielding technique ineffective.

As an example, consider a hollow copper cylinder with a radius of 1 m, a height of 0.5 m, and a thickness of 1 cm, placed in a 1 T uniform magnetic field aligned with its axis and oscillating at frequencies of 1 Hz and 10 Hz. Due to the induced currents, the magnetic field inside the cylinder decreases to approximately 0.79 T at 1 Hz and 0.35 T at 10 Hz (Figure 5.12).

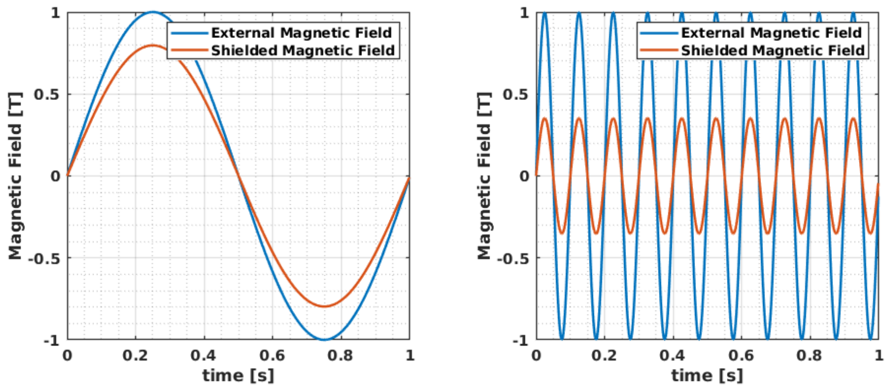

Figure 5.12: Comparison between the external magnetic field and the magnetic field at the center of the cylinder for an oscillating field at 1 Hz (left) and 10 Hz (right).

In the context of magnetic-noise reduction in gravitational-wave interferometers, however, this strategy is of limited effectiveness, since the frequencies of interest are below 100 Hz, where induced currents are extremely weak [73].

5.3 Active Mitigation Techniques

Active mitigation techniques rely on the implementation of adaptive current systems operating within a feedback control loop. The fundamental objective is to generate a compensation magnetic field that is, at any given time and within a specific spatial volume, equal and opposite to the environmental field detected by a network of sensors.

The most common architecture for such systems is based on **Helmholtz coils**, originally proposed by Helmholtz [74, 75]. Due to their specific geometry, these coils can generate a highly uniform magnetic field within a restricted central volume, serving as the primary actuators for active noise cancellation.

While conceptually straightforward, the practical implementation of these systems – whether based on Helmholtz coils or more complex actuator configurations – presents significant technological challenges for next-generation gravitational wave detectors. The efficacy of any active mitigation strategy is intrinsically limited by physical and technical constraints inherent to electromagnetic feedback:

- **Signal-to-Noise Ratio (SNR) and Sensor Precision:** Every active system is fundamentally limited by the floor noise of the magnetometers used for monitoring. The sensor's electronic noise is inevitably "injected" into the control loop and converted into real magnetic fluctuations by the compensation coils. Furthermore, the finite distance between the sensing point and the volume of interest (the payload) introduces a systematic error in the field reconstruction, limiting the fidelity of the cancellation.

- **Bandwidth and Loop Latency:** The ability to respond to fast transients or high-frequency magnetic fluctuations is dictated by the acquisition system's latency and the actuators' inductance. A temporal phase lag between the external field and the compensation field can turn negative feedback into positive feedback, paradoxically leading to an amplification of the environmental noise rather than its suppression.

- **Inductive Coupling and Eddy Currents:** Dynamic variations in the compensation currents induce eddy currents in the surrounding metallic structures. These currents generate secondary magnetic fields with complex temporal and spatial dependencies, which can destabilize the feedback loop and degrade the field's homogeneity within the payload volume.

- **Mechanical Interference with the Payload:** The mitigation field is not strictly confined to the target volume but permeates the entire apparatus. This field can directly interact with the permanent magnets used for the position control of the Test Masses, introducing mechanical disturbances that couple directly into the interferometer's sensitivity channel.

These critical challenges underscore that a purely active approach may prove insufficient to satisfy the stringent *magnetic cleanliness* requirements of Advanced Virgo+ and future-generation detectors, such as the Einstein Telescope (ET). This limitation provides the primary motivation for pursuing hybrid mitigation strategies and synergistic projects, such as **CALMA** (see Chapter 8), aimed at further suppressing environmental magnetic noise.

5.4 Superconductors

Superconductivity is a macroscopic quantum phenomenon discovered by Heike Kamerlingh Onnes in 1911 [76], characterized by the total disappearance of electrical resistance and the expulsion of magnetic fields when certain materials are cooled below a characteristic **critical temperature** (T_c). This property can be effectively leveraged in the design of gravitational wave interferometers to suppress magnetic noise.

The following sections describe the two primary categories of superconductors, while the final one evaluates their effectiveness in realistic experimental configurations. Crucially, the analysis highlights that, as with ferromagnetic shields, the presence of apertures and geometric discontinuities significantly degrades the Shielding Factor (SF) provided by the superconducting layer, presenting a major challenge for their practical integration.

5.4.1 Type-I Superconductors

Type-I superconductors, which predominantly comprise pure metallic elements, are characterized by low critical temperatures – typically below 10 K. Once cooled below T_c, they manifest two defining properties: the total disappearance of electrical resistance and the complete expulsion of the internal magnetic flux, a phenomenon known as the **Meissner effect**.

Unlike classical diamagnetism, the Meissner effect is not attributable to a simple modification of magnetic permeability, but is instead a macroscopic quantum phenomenon arising from screening currents circulating near the material's surface. Consequently, treating a superconductor as a perfect diamagnet can lead to oversimplified or incorrect descriptions.

A phenomenological description of the magnetic behavior of type-I superconductors was proposed by the London brothers in 1935 [77]. The London equations assume that the magnetic field is expelled through currents confined within a finite depth λ, known as the London penetration depth.

Building on the London model, Ginzburg [78] and later Lung-Tao and Zharkov [79] derived analytical expressions for the shielding factor of an infinitely long hollow superconducting cylinder of thickness d. In the limit $d \gg \lambda$, the shielding factor can be written as [80]:

$$SF \simeq \frac{R_{in}}{4\lambda}\sqrt{\frac{R_{in}}{R_{out}}}e^{\frac{d}{\lambda}} \tag{5.7}$$

where R_{out} and R_{in} are, respectively, the outer and inner radii of the superconductor.

By contrast, Du Bois and Wills [63, 64] showed that the shielding factor for an infinitely long cylindrical ferromagnetic layer with relative permeability

μ_r is given by:

$$SF = 1 + \frac{1}{4}\frac{(\mu_r - 1)^2}{\mu_r}\left[1 - \left(\frac{R_{in}}{R_{out}}\right)^2\right] \tag{5.8}$$

The marked difference in the geometrical dependence of these two cases highlights why describing type-I superconductivity using the classical perfect-diamagnet model is insufficient to correctly capture the shielding properties of real superconductors.

It is also important to note that the critical temperature is not a fixed parameter but depends on the strength of the applied magnetic field. Above a certain threshold – known as the critical field – the material transitions out of the superconducting state, regardless of temperature (Figure 5.13 and Table 5.3).

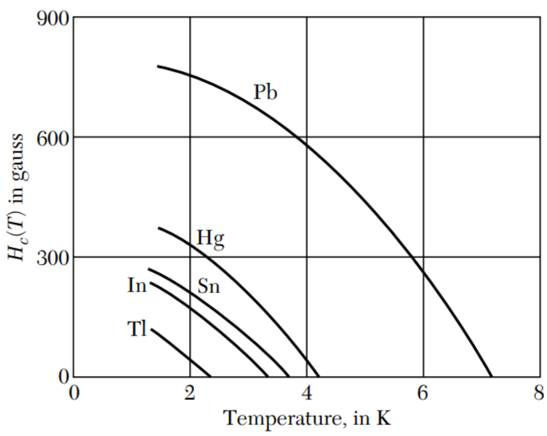

Figure 5.13: Experimental threshold curves of the critical field $H_c(T)$ versus temperature for several superconductors. A specimen is superconducting below the curve and normal above it. Image reproduced from [81].

Elements	T_C [K] at $H = 0$	H_C [gauss] at $T = 0$
Sn	3.72	305
Pb	7.19	803
Hg	4.15	411
Nb	9.25	2060
V	5.40	1410

Table 5.3: Critical temperature and zero-temperature critical field for selected type-I superconductors [82].

5.4.2 Type-II Superconductors

Type-II superconductors, typically alloys and compounds, are characterized by higher critical temperatures and the existence of a mixed state.

Below the first critical field $H < H_{C_1}(T)$, they behave as type-I superconductors: perfect conductors and perfect diamagnets. Between the first and the second critical field, $H_{C_1}(T) < H < H_{C_2}(T)$, they enter the mixed state: resistivity remains zero, but the magnetic field penetrates the material through quantized flux lines. Above the second critical field $H > H_{C_2}(T)$, the material loses superconductivity entirely (Figure 5.14 and Table 5.4).

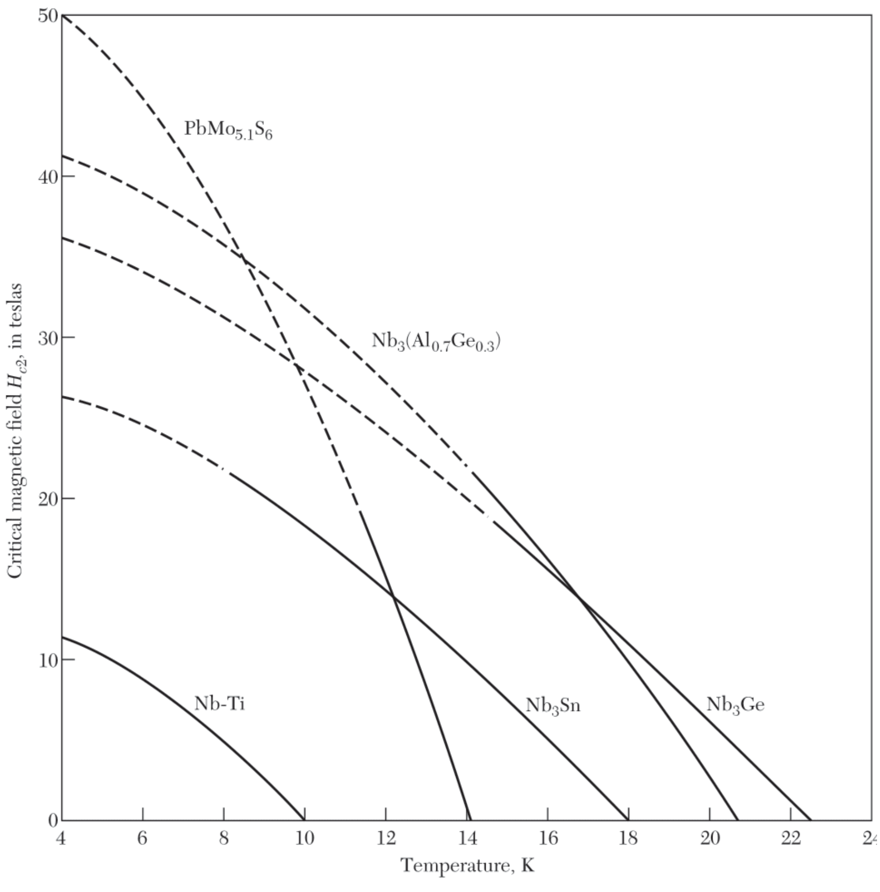

Figure 5.14: Experimental threshold curves of the second critical field $H_{c_2}(T)$ versus temperature for several superconductors. A specimen is in the mixed state below the curve and normal above it. Image reproduced from [81].

Compounds	T_C [K] at $H = 0$	H_{C_2} [T] at $T = 0$
V_3G_a	16.5	27
V_3S_i	17.1	25
$N_{b_3}A_l$	20.3	34
$N_{b_3}G_e$	23.3	38
M_gB_2	40	≈ 20

Table 5.4: Critical temperature and zero-temperature second critical field for selected type-II superconductors [82].

5.4.3 Magnetic Shielding in Real Geometries

While analytical models are often based on simplified assumptions, such as infinite or perfectly closed geometries, experimental implementations necessarily require functional openings for optical or mechanical access. Such geometric discontinuities can induce a substantial degradation of the device's shielding effectiveness, shifting the real performance away from the nominal values predicted for superconducting materials.

As an illustrative example, the study by **Wéra et al. (2019)** [83] analyzes how the configuration of terminations in a superconducting cylinder (height 30 mm, inner radius 10 mm) drastically influences the overall shielding factor. The work identifies and compares four primary geometric configurations (Figure 5.15):

- **Open:** A hollow cylindrical tube without terminations, used as a reference for flux penetration from the ends.
- **Closed:** A superconducting disk (*cap*) placed in simple mechanical contact with the end of the tube; this interface introduces a thin air gap that interrupts the galvanic and magnetic continuity of the material.
- **Adjusted:** A configuration where the end of the tube is machined to house the cap inside, optimizing the geometric coupling while maintaining a physical surface discontinuity.
- **Fused:** A configuration in which the tube and termination constitute a single solid block, ensuring perfect continuity of the paths for supercurrents.

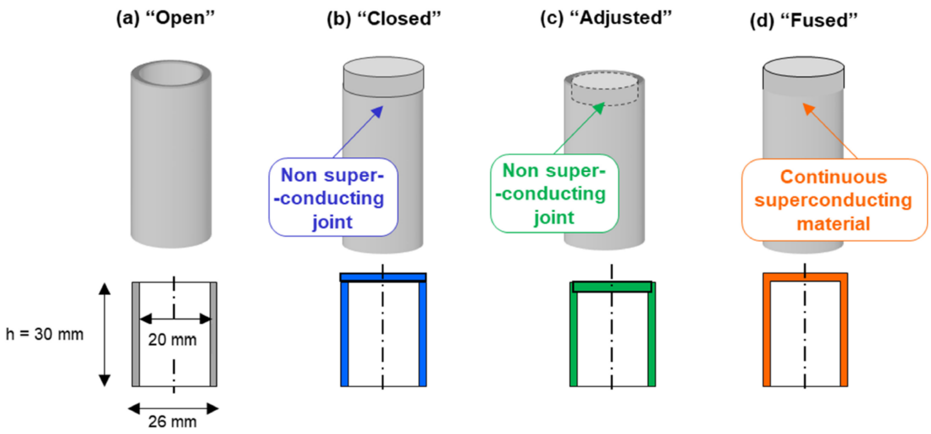

Figure 5.15: Schematic illustration of the "open", "closed", "adjusted", and "fused" configurations analyzed in the work by Wéra et al. Image reproduced from [83].

The different geometries were evaluated by exposing them to axial external magnetic fields (parallel to the tube axis) and transverse fields (perpendicular to the axis). As shown in Figure 5.16, the *shielding factor* (SF) measured near the ends varies significantly depending on the degree of system continuity and field orientation.

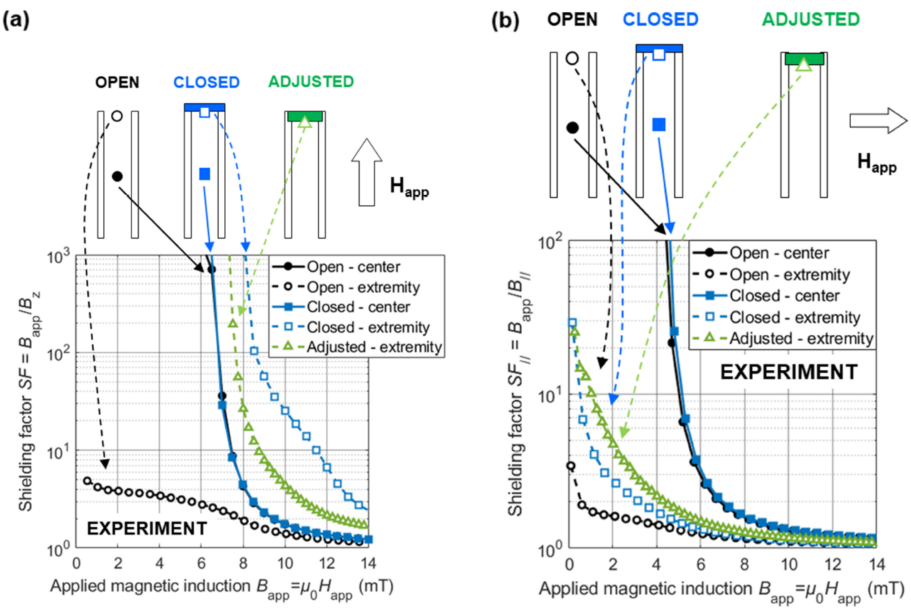

Figure 5.16: Experimental behavior of the shielding factor SF as a function of the applied magnetic field intensity, in the directions parallel (a) and perpendicular (b) to the tube axis, respectively. Image reproduced from [83].

Experimental evidence demonstrates that, especially in the presence of transverse fields (Figure 5.16b), only the **Fused** configuration preserves high shielding power along the entire axis. In the remaining configurations, even a minimal interruption in the superconductor's continuity prevents the circulation of the current loops necessary for complete compensation of the external field.

In conclusion, the presence of millimetric gaps or structural openings can compromise the system's efficiency, leading to SF values orders of magnitude lower than those theoretically predictable for an ideal superconducting shell. This aspect is critical in many applications within the field of gravitational wave detectors, such as the shielding of the test mass tower, where the presence of apertures is an unavoidable necessity.

Chapter 6

Test Mass Tower Shielding

Test Mass (TM) towers represent the primary coupling point between external environmental magnetic fields and the interferometer sensitive components, as discussed in Chapter 4.

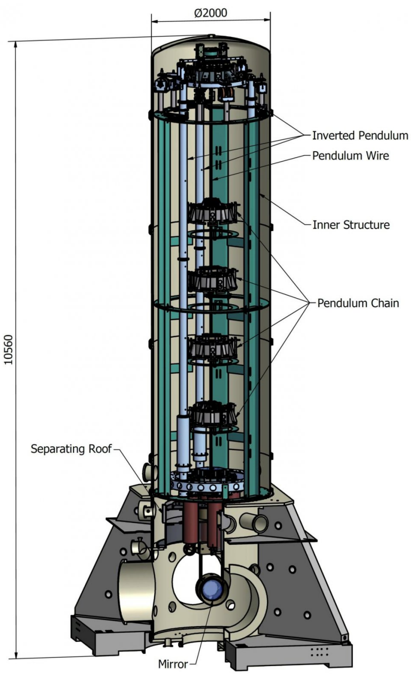

Figure 6.1: Schematic drawing of the Virgo TM tower.

Portions of this chapter, including figures and results, have been adapted from the author's previous works *"Magnetic Noise Mitigation Strategies for the Einstein Telescope Infrastructure"* [73] and *"Einstein Telescope: Ferromagnetic Shielding for Magnetic Noise Mitigation"* [84]

The numerical analyses presented in the following sections use the Virgo West-End tower as a reference (Figure 6.1). While definitive designs for the Einstein Telescope (ET) towers are still under development, the physical principles and the shielding optimization strategies derived here remain valid for both detectors.

6.1 Ferromagnetic Shields

The effectiveness of the shields was evaluated by implementing mu-metal layers in the lower section of the tower, which houses the TM. Following the methodology of **increasing geometric complexity** described in Chapter 3, the model was not derived by simplifying existing CAD files, but rather through a systematic analytical reconstruction.

The original CAD drawing (Figure 6.2) served as the primary reference for dimensions and structural layout. The modeling process started from elementary cylindrical geometries, which were progressively refined to incorporate the breaking of axial symmetry caused by the interferometer arm apertures (Figure 6.3), the viewports (Figure 6.4), and finally the complex mechanical flanges and supports (Figure 6.5).

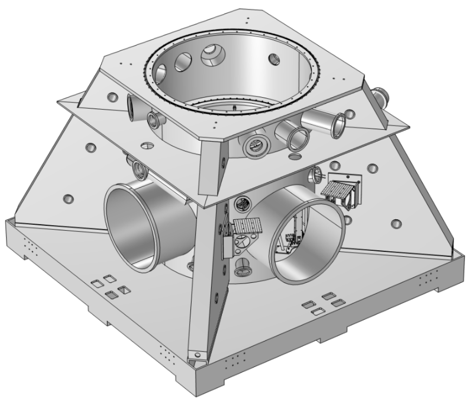

Figure 6.2: CAD drawing of the lower part of the West-End Virgo tower.

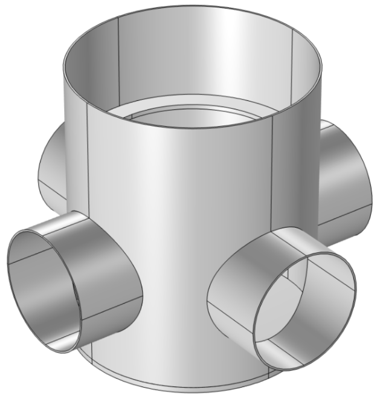

Figure 6.3: A highly simplified geometry of the tower's lower section.

This "bottom-up" approach, while more demanding during the initial geometric modeling phase, resulted in significant computational time savings. By eliminating magnetically negligible structural details, it allowed for the optimization of computational resources, focusing them on the features that primarily govern magnetic flux penetration – specifically, the discontinuities in the cylindrical surface where mu-metal cannot be applied.

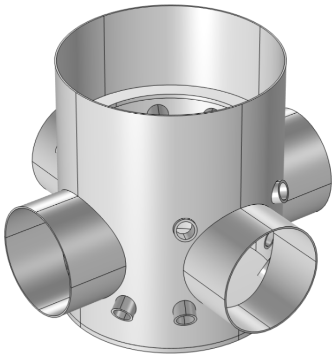

Figure 6.4: A more realistic representation including viewports.

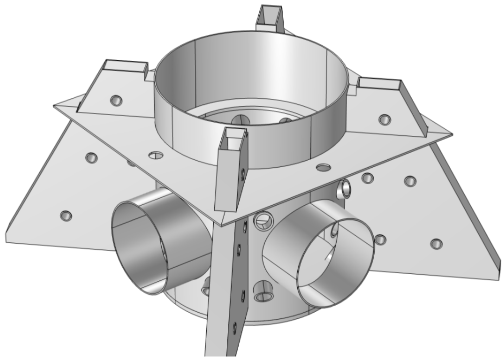

Figure 6.5: A high-fidelity representation including flanges and mechanical supports.

Furthermore, by isolating the impact of specific features such as arm apertures and viewports, this study provides a generalized shielding solution. While mechanical details may vary between different detectors (e.g., from Virgo to ET), the fundamental understanding of how these mandatory openings influence the Shielding Factor remains a scalable design standard, rather than a merely site-specific solution.

6.1.1 Material Properties and Simulation Setup

The magnetic fields of interest, as discussed in Chapter 4, range from the pT to the nT scale [46, 47, 29, 48]. In the simulations, the values of magnetic permeability measured in [59] for an annealed mu-metal sample subjected to a field of a few nT were employed. The underlying assumption is that the material preserves a linear response below the nanotesla threshold, an assumption experimentally validated for similar samples in [72].

The effectiveness of the shield is quantified through the Shielding Factor (SF), as defined in Chapter 5. In the following section, the SF is presented as a function of both the frequency of the external field and the thickness (width) of the mu-metal shield.

The shield is applied along the lateral surface of the tower (where no openings are present) over a height of 2.375 m, and extends by 0.585 m along each arm. For each configuration, the SF is calculated within a sphere of 0.5 m radius centered at the intersection point between the tower axis and the interferometer arms.

6.1.2 Shielding Performance Analysis

In this section, the results for the three different configurations are presented to highlight how the increasing geometric detail affects the magnetic mitigation.

Configuration 1: Simplified Geometry In Table 6.1, we show the *SF* achieved with the highly simplified geometry (Figure 6.3).

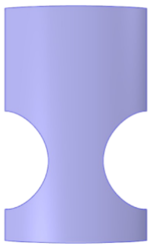

Figure 6.6: One of the ferromagnetic shields employed in the simulation. Image adapted from [84].

Frequency [Hz]	**Shielding Factor** width=1 mm	width=2 mm
0	10.40	14.47
10	9.43	13.47
100	8.45	12.39

Table 6.1: Shielding Factor achieved using a 1 mm/2 mm thick mu-metal layer. The magnetic field is directed along one interferometer arm. One of the shields applied in the simulation is shown in Fig. 6.6.

Configuration 2: Intermediate Geometry with Viewports In Table 6.2, we show the results for the model including viewports (Figure 6.4).

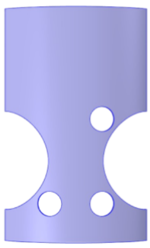

Figure 6.7: One of the ferromagnetic shields employed in the simulation. Image adapted from [84].

Frequency [Hz]	**Shielding Factor** width=1 mm	width=2 mm
0	9.89	13.85
10	8.95	12.87
100	8.02	11.82

Table 6.2: Shielding Factor achieved using a 1 mm/2 mm thick mu-metal layer. The magnetic field is directed along one interferometer arm. One of the shields applied in the simulation is shown in Fig. 6.7.

Configuration 3: Realistic Geometry Finally, Table 6.3 presents the data for the high-fidelity representation including flanges and supports (Figure 6.5).

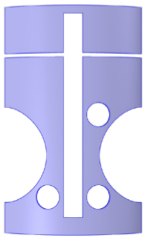

Figure 6.8: One of the ferromagnetic shields employed in the simulation. Image adapted from [84].

Frequency [Hz]	Shielding Factor width=1 mm	width=2 mm
0	4.07	6.10
10	3.69	5.51
100	3.34	4.95

Table 6.3: Shielding Factor achieved using a 1 mm/2 mm thick mu-metal layer. The magnetic field is directed along one interferometer arm. One of the shields applied in the simulation is shown in Fig. 6.8.

6.1.3 Discussion

The comparison between the three configurations reveals a critical dependence of the Shielding Factor on geometric details. The transition from a simplified shell to a realistic structure containing mechanical discontinuities leads to a significant degradation of the SF.

At 0 Hz, for a 2 mm thickness, the SF drops from 14.47 (simplified) to 6.10 (realistic). This phenomenon is primarily attributed to the "flux leakage" occurring at the mechanical interfaces and the alteration of the magnetic reluctance path provided by the shield. These findings suggest that for future detectors like ET, shielding design cannot rely on idealized models, as structural elements and flanges provide significant pathways for magnetic field penetration.

To gain a deeper understanding of this degradation, Figure 6.9 compares the magnetic field distribution on a longitudinal plane for the simplified (a) and realistic (b) configurations, both considering a mu-metal thickness of **1 mm**. While, Figure 6.10 shows the pointwise shielding factor $SF_{(P)}$ for the same geometries. In the simplified model, the attenuation is relatively uniform, with $SF_{(P)}$ values gradually increasing toward the center of the tower. In contrast, the realistic model exhibits significant "hotspots" of reduced shielding near the flanges and supports.

The situation exacerbates further when transitioning from numerical simulations to physical implementation, as evidenced in the study by D'Angelo et al. [85, 86]. In this work, a Faraday isolator was encased in multiple ferromagnetic layers; nonetheless, despite a simulated shielding factor of 165, experimental measurements on the physical prototype yielded an SF on the order of ten. This represents an unequivocal indication of the result's critical dependence on both geometric configurations and material non-idealities.

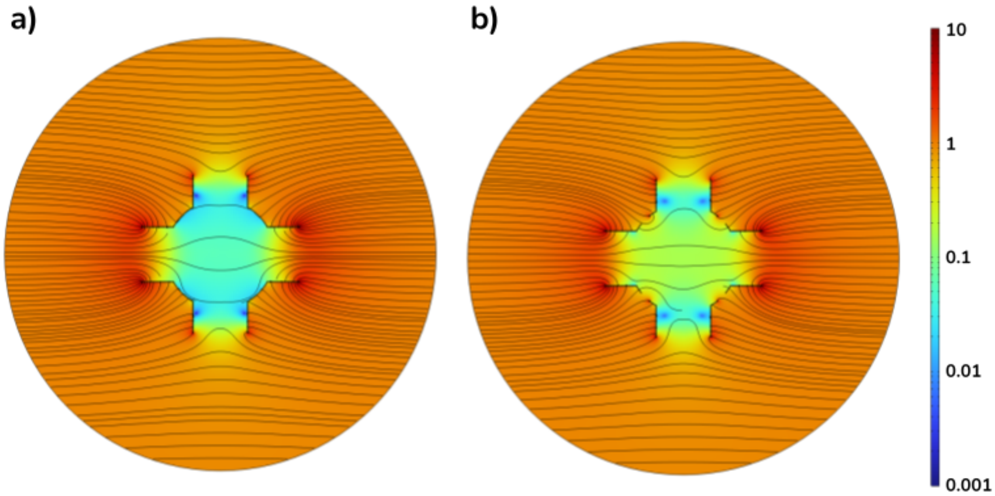

Figure 6.9: Magnetic field distribution on a longitudinal plane ($B_{ext} = 1$ T) for a shield thickness of 1 mm. (a) Configuration 1; (b) Configuration 3.

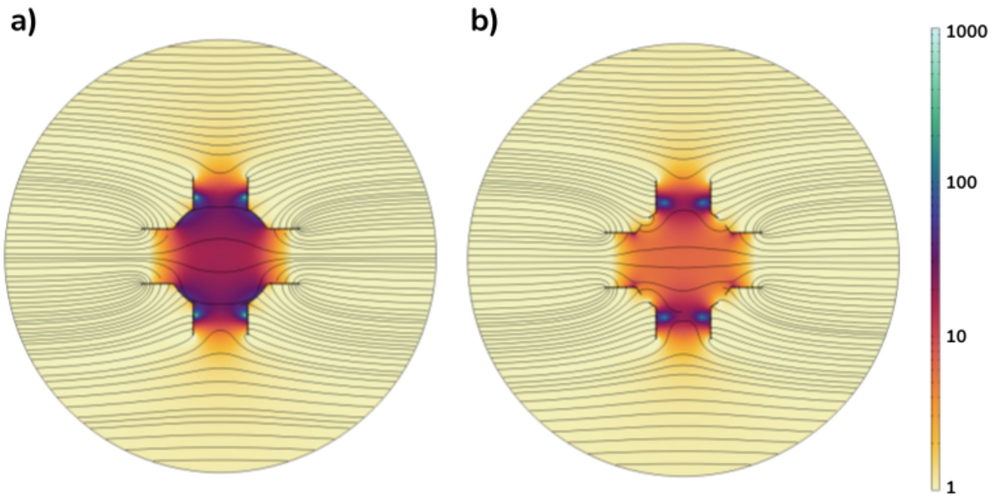

Figure 6.10: Pointwise shielding factor $SF_{(P)}$ on the longitudinal plane (shield thickness: 1 mm). The colormap is lower-bounded to 1. In the realistic geometry (b), the discontinuities in the shield significantly reduce the quiet zone area compared to the simplified shell (a).

6.2 Multilayer Shielding Strategy

As discussed in Chapter 4, the use of multilayer structures in closed configurations can increase the shielding factor by several orders of magnitude compared to a single layer of equivalent total thickness. However, in the case of interferometers, the mandatory presence of large openings could significantly limit this enhancement.

To evaluate the actual benefit of multilayers in an open geometry, we performed a series of finite element simulations. Due to the high computational cost – since multilayer models require extremely refined meshes to resolve the thin mu-metal shells – we adopted a simplified strategy. We used the intermediate geometry featuring only the viewports (Figure 6.4) and applied the mu-metal exclusively to the lateral surface of the tower, omitting the shields on the arms.

Table 6.4 reports the SF as a function of the number of layers, keeping the total mu-metal thickness constant at 1 mm.

Frequency [Hz]	**1 layer**	**2 layers**	**3 layers**	**4 layers**	**5 layers**
0	5.26	5.39	5.50	5.60	5.69
10	4.96	5.08	5.17	5.25	5.33
100	4.64	4.74	4.82	4.89	4.95

Table 6.4: Shielding Factor for different multilayer mu-metal configurations with a total thickness of 1 mm (1×1 mm, 2×0.5 mm, 3×0.33 mm, 4×0.25 mm, 5×0.2 mm). Layers are separated by 5 mm air gaps. The external magnetic field is applied along one interferometer arm.

The results show that while the SF increases with the number of layers, the improvement is remarkably small (less than 10% gain between one and five layers). This confirms that in geometries with large apertures, the performance is not limited by the magnetic reluctance of the material, but by the direct leakage through the openings. While multilayers effectively divert the flux that would otherwise penetrate the metal, they cannot mitigate the field lines entering through the mandatory viewports and arm apertures.

6.2.1 Practical Advantages of Multilayering

Despite the limited increase in the nominal SF shown by the simulations, multilayer configurations remain essential for several practical and physical reasons:

- **Saturation Mitigation:** Alternating mu-metal with materials such as ferrite – which possesses a lower permeability but a higher saturation threshold – protects the inner high-permeability layers from saturating when exposed to strong environmental fields.

- **Staggered Joint Arrangement:** In practice, shielding a structure as large as a TM tower requires the assembly of multiple mu-metal patches. A staggered arrangement across multiple layers is crucial to mitigate flux penetration through the mechanical gaps (leaks) between adjacent sections, as demonstrated in [87].

- **Johnson Noise Reduction:** As detailed in Chapter 5, multilayer structures are fundamental to suppressing Johnson noise, a critical requirement for meeting the sensitivity targets of third-generation detectors.

6.3 Active Mitigation: Adaptive Currents

In the previous sections, we observed that the system's shielding is strongly influenced by the presence of apertures, which prevent multilayer configurations from significantly improving the overall shielding factor. A promising strategy to mitigate this effect is to complement the passive ferromagnetic shielding with a dedicated active protection system specifically designed for these apertures.

6.3.1 Material Properties and Simulation Setup

The most straightforward active solution consists of placing four conductive coils at the locations of the arm apertures, as illustrated in Figure 6.11. For these simulations, the geometry and the arrangement of the mu-metal layers remain identical to those used in the multilayer analysis (Section 6.2).

The coils are supplied with a current specifically configured to generate a counter-field that cancels the external magnetic field at the center of each aperture. This "active plug" effectively reduces the flux leakage that previously bypassed the ferromagnetic layers.

6.3.2 Shielding Performance Analysis

Table 6.5 presents the results obtained by simulating the hybrid system, combining the multilayer ferromagnetic shielding on the lateral surface with the four active coils.

The integration of a dedicated active component provides a clear enhancement of the overall shielding performance. By comparing these results with Table 6.4, it is evident that the addition of the four coils allows the Shielding

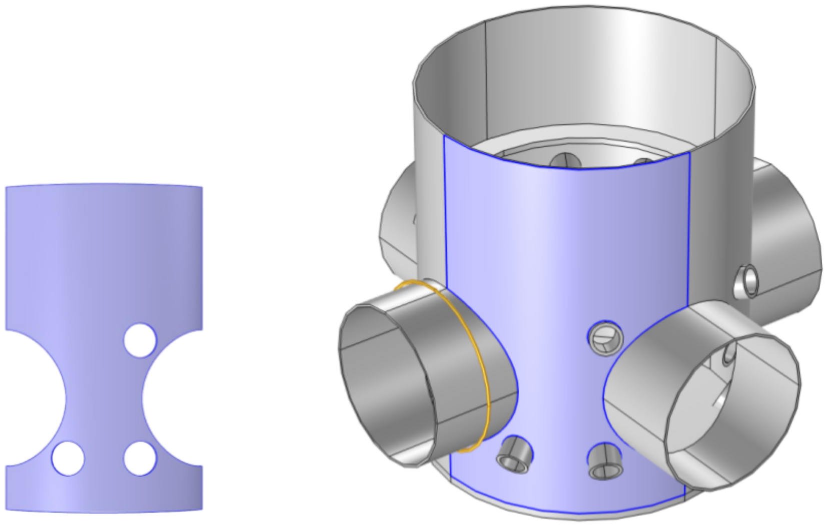

Figure 6.11: The simulated geometry (grey), with one of the ferromagnetic shields (blue) and one of the active coils (yellow) highlighted.

Factor to approximately double across all frequencies and layer configurations.

Frequency [Hz]	1 layer	2 layers	3 layers	4 layers	5 layers
0	10.14	10.86	11.08	11.23	11.47
10	9.15	9.72	9.89	10.01	10.20
100	8.16	8.60	8.73	8.82	8.96

Table 6.5: Shielding Factor for multilayer configurations (total thickness 1 mm) integrated with active coils. The coils are powered to cancel the component of the magnetic field directed along the arm axis at their respective centers.

6.3.3 Discussion

While the presented results demonstrate a significant improvement, it is important to emphasize that the current configuration represents a **proof of concept**. The choice of a current value that strictly cancels the magnetic field at the geometric center of the apertures is an arbitrary starting point; further optimization of the current profile and coil geometry would likely yield even higher Shielding Factors.

Furthermore, it must be noted that these simulations operate under ideal conditions. As discussed in Chapter 5, active solutions are theoretically capable of perfect cancellation, but their practical effectiveness is limited by the precision of the hardware. In a real-world implementation, the current generator introduces fluctuations around the nominal current value. For environmental fields as low as those encountered in gravitational wave detectors (pT to nT scale), the residual field generated by these current fluctuations can be of the same order of magnitude as the field one intends to eliminate. Consequently, the actual Shielding Factor achievable in the laboratory will be governed by the noise floor of the control system and the stability of the power supplies, factors that are not accounted for in these numerical models.

6.4 Eddy Current Shielding

An alternative mitigation strategy involves the exploitation of **eddy currents**. As discussed in Chapter 5, these currents are generated within a conductor according to the Faraday's law when it is exposed to a time-varying magnetic field.

Unlike active techniques, eddy current shielding is entirely passive, requiring no power supply or feedback electronics. However, as demonstrated in [73], this approach proves to be **extremely ineffective** for the specific requirements of gravitational-wave test mass towers.

6.4.1 Material Properties and Simulation Setup

To evaluate this method, two configurations were modeled using conductive hollow cylinders in a **Helmholtz configuration**. In this setup, the cylinders in each pair are separated by a distance equal to their respective radii to optimize the uniformity of the generated opposing field.

In **Configuration 1**, the two pairs of cylinders are placed outside the tower intersection, enclosing the interferometer arms (Figure 6.12). In **Configuration 2**, the pairs are placed inside the tower (Figure 6.13), significantly reducing the distance from the target area.

6.4.2 Analysis of Configuration 1: External Cylinders

The following tables summarize the Shielding Factor (SF) for the external cylinders ($R_x = 2.05$ m, $R_y = 2$ m).

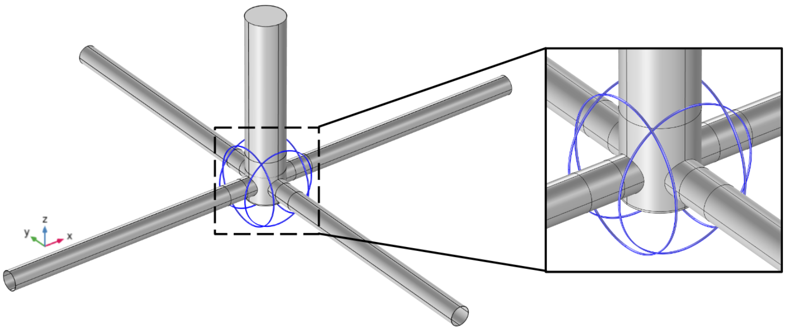

Figure 6.12: Configuration 1: Two pairs of conductive cylinders arranged in a Helmholtz configuration outside the tower intersection. Image reproduced from [73].

Frequency [Hz]	Shielding Factor $\mathbf{B}_{ext} \parallel \hat{x}$	$\mathbf{B}_{ext} \parallel$ diag	$\mathbf{B}_{ext} \parallel \hat{y}$
1000	1.836	1.845	1.836
2000	1.837	1.847	1.837
5000	1.838	1.848	1.838
10,000	1.838	1.848	1.838

Table 6.6: SF vs frequency for Configuration 1 (thickness=2 cm, height=5 cm).

Thickness [cm]	Shielding Factor $\mathbf{B}_{ext} \parallel \hat{x}$	$\mathbf{B}_{ext} \parallel$ diag	$\mathbf{B}_{ext} \parallel \hat{y}$
0.4	1.773	1.772	1.773
0.8	1.781	1.783	1.790
1.2	1.804	1.806	1.809
1.6	1.823	1.825	1.825
2.0	1.836	1.845	1.836

Table 6.7: SF vs Thickness for Configuration 1 (freq=1000 Hz, height=5 cm).

6.4.3 Analysis of Configuration 2: Internal Cylinders

For the internal cylinders ($R_x = 0.55$ m, $R_y = 0.5$ m), the results show a slight improvement due to the proximity to the Test Mass.

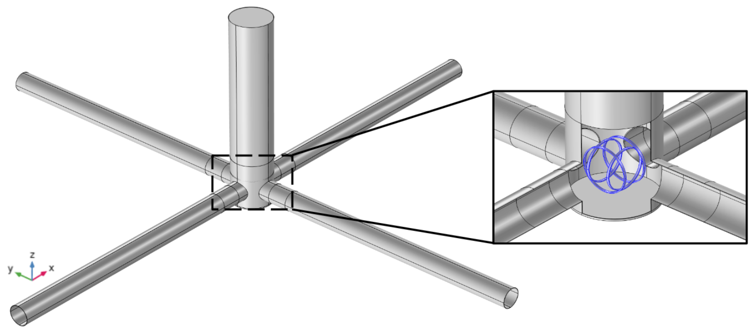

Figure 6.13: Configuration 2: Helmholtz pair of cylinders placed inside the tower. Image reproduced from [73].

Frequency [Hz]	Shielding Factor $\mathbf{B}_{ext} \parallel \hat{x}$	$\mathbf{B}_{ext} \parallel$ diag	$\mathbf{B}_{ext} \parallel \hat{y}$
100	2.338	2.394	2.436
500	2.435	2.498	2.546
1000	2.449	2.513	2.562
10,000	2.458	2.522	2.572

Table 6.8: SF vs frequency for Configuration 2 (thickness=2 cm, height=5 cm).

Thickness [cm]	Shielding Factor $\mathbf{B}_{ext} \parallel \hat{x}$	$\mathbf{B}_{ext} \parallel$ diag	$\mathbf{B}_{ext} \parallel \hat{y}$
0.4	2.240	2.260	2.275
0.8	2.308	2.329	2.355
1.2	2.356	2.369	2.401
1.6	2.417	2.444	2.472
2.0	2.435	2.498	2.546

Table 6.9: SF vs Height for Configuration 2 (freq=500 Hz, height=5 cm).

6.4.4 Discussion

The simulation results clearly indicate that eddy current shielding is inadequate for the requirements of the Virgo towers. Even at high frequencies (10 kHz) and increased thicknesses, the SF consistently fails to exceed a value of 3.5.

It is crucial to note that the frequencies investigated (100 Hz – 10 kHz) are significantly higher than the actual range of interest for magnetic noise mitigation in gravitational-wave detectors, which is typically concentrated below 100 Hz. Since the induced electromotive force – and consequently the shielding eddy currents – scales proportionally with frequency, the performance at lower frequencies is expected to be even worse, approaching an SF of 1 (no shielding) as the frequency tends to zero. These low-frequency regimes were not explicitly simulated due to numerical stability limits in COMSOL Multiphysics; as $\omega \to 0$, the inductive coupling becomes negligible, often leading to ill-conditioned matrices and convergence issues in the frequency-domain solver.

Furthermore, real-world implementation would likely yield even poorer results than those predicted by simulations. Our numerical models assume **ideal electrical continuity** across the entire structure. In practice, the presence of mechanical joints, bolts, and welds introduces significant resistive bottlenecks. Even a minor discontinuity in the material's conductivity or a high-resistance weld can disrupt the path of the induced currents, preventing them from forming the closed loops necessary to generate a coherent opposing magnetic field.

It is also important to emphasize that both simulated configurations serve primarily as a **proof of concept**. From an engineering perspective, Configuration 1 is extremely difficult to realize due to the massive dimensions of the required conducting loops. Configuration 2, while showing slightly better numerical results, is altogether unfeasible: the internal volume of the tower is already occupied by the test mass cage and the complex suspension system. Furthermore, the installation of such conductive structures inside the tower would be incompatible with the stringent ultra-high vacuum requirements.

The only structurally "feasible" alternative would involve placing the conductors around the interferometer arms, similar to the layout used for active adaptive current systems. However, this positioning would further diminish the shielding performance due to the increased distance from the target volume.

Chapter 7

The MANET Project

The MAgnetic Noise test facility for ET (MANET) [88] is a high-precision experimental laboratory designed for the magnetic characterization of components and materials. While its primary mission is to support the development of the Einstein Telescope (ET) [89, 90, 91], MANET is a standalone testing facility capable of providing sophisticated magnetic metrology for a wide range of scientific applications.

7.1 Motivation and Scientific Goals

The study conducted in Chapter 6 demonstrates that even with optimized ferromagnetic layers and active coils, the mitigation provided by shielding alone is not sufficient to reach the Einstein Telescope's target sensitivity. Indeed, as previously discussed, if the environmental magnetic noise at the ET site remains comparable to that of Virgo, a suppression factor of at least 100 is required – a goal that exceeds the performance of the passive and hybrid systems simulated so far.

This gap between simulation and target becomes even more critical when considering that real-world conditions are significantly more demanding than idealized numerical models. A primary example is the behavior of high-permeability materials like mu-metal: its magnetic properties are extremely delicate and heavily dependent on proper thermal annealing. Mechanical stresses, such as bending or machining during the assembly of the tower shields, can drastically degrade the material's permeability, essentially requiring a new annealing process to restore its shielding efficiency. Consequently, the actual shielding factor of a physical structure will invariably be lower than the one predicted by "ideal" simulations.

This is where MANET becomes essential, serving two primary and distinct purposes:

- **Characterization and Mapping:** It provides a controlled environment to precisely map the magnetic signature of specific devices – such as Faraday isolators – before their installation. This proactive approach is crucial for ET, where even a small, uncharacterized magnetic dipole could compromise the target sensitivity if placed near critical components.
- **Prototype Validation:** The facility serves as a dedicated platform to test full-scale shielding prototypes. This allows for the empirical validation of mitigation techniques under non-ideal conditions, providing a realistic assessment of shielding degradation caused by mechanical stress and assembly tolerances.

The true strength of the facility lies in the **complementarity of these functions**, which enables the complete validation of the *mitigation chain*. A device can first be characterized to identify its unshielded magnetic signature; subsequently, a custom mitigation system can be applied and the entire assembly re-measured. This iterative cycle – characterization, mitigation, and verification – provides a realistic assessment of the Shielding Factor (SF), accounting for assembly joints, edge effects, and material stresses that numerical models cannot fully predict.

7.2 System Design

MANET is a complex assembly designed to integrate magnetic sensing, sample manipulation, and field control within a single, magnetically transparent framework (Figure 7.1). The facility primarily consists of three key components:

- **Magnetic Sensing System:** A series of triaxial sensors arranged to map the field produced by the device under test.
- **Rotation System:** A rotating table with adjustable height to precisely orient the sample at the center of the measurement volume.
- **Field Generation System:** Three pairs of Helmholtz coils used to compensate for the Earth's magnetic field or to test the sample's susceptibility to external perturbations.

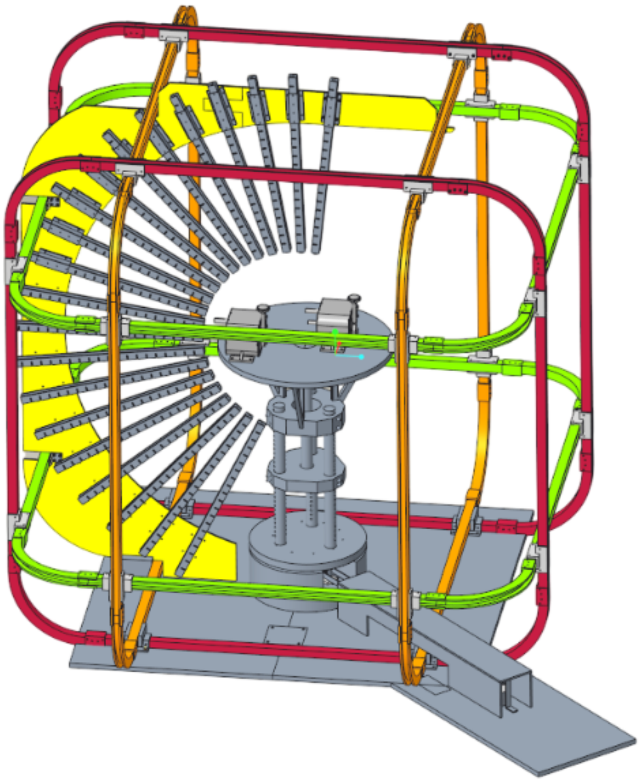

Figure 7.1: CAD drawing of the MANET facility.

7.2.1 Magnetic Sensing System

The sensors are mounted on sliding PE-HD bars arranged along a semicircle. This configuration allows for the radial distance from the center to be adjusted (from 48 cm up to 128 cm), enabling the characterization of objects with varying dimensions and magnetic emission intensities.
We selected two types of triaxial fluxgate magnetometers to provide a wide dynamic range (Table 7.1): the **Mag03-100** (high sensitivity, $\pm 100\ \mu T$ range) and the **Mag690-1000** (lower sensitivity, $\pm 1000\ \mu T$ range). This dual-sensor approach ensures that even strongly magnetic components can be characterized without saturating the acquisition system.

Performance	Mag03-100	Mag690-1000
Range	$\pm 100 \mu T$	$\pm 1000 \mu T$
Noise	$\leq 10pTrms/\sqrt{Hz}$ *at* $1Hz$	$\leq 40pTrms/\sqrt{Hz}$ *at* $1Hz$

Table 7.1: Comparison between Mag03-100 and Mag690-1000 magnetometers.

7.2.2 Rotation System

The sample is placed on a table that rotates around its vertical axis, allowing the sensors to measure the field over a discrete spherical surface. To support the mathematical development of the magnetic field into multipoles, the object must be perfectly centered. To this end, the table height is adjustable in 15 steps of 2.5 *cm*.
The rotational system is driven by a NEMA 34 stepper motor coupled to an 82-tooth ring gear via a 20-tooth pinion. This mechanical reduction provides an angular resolution of approximately 0.44° per step, ensuring high spatial precision during the mapping process. Despite being made of plastic, the table is designed to support loads up to 100 *kg*.

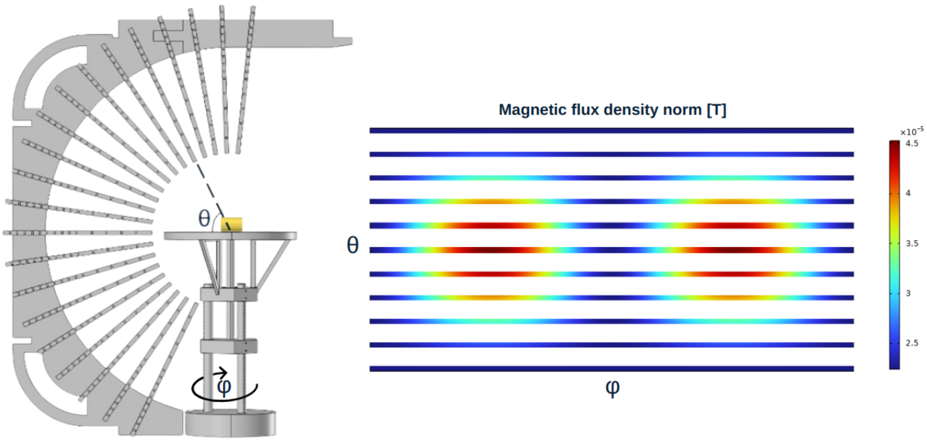

Figure 7.2: Simulation of the magnetic field magnitude produced by a horizontal perfect dipole, as it will be mapped by the MANET sensor array during table rotation. Image reproduced from [73].

	**Material(s):**	POM-C, PE-HD
	Weight:	~ 75 *kg*
	Maximum Payload:	~ 100 *kg*
	Vertical adjustability:	15 steps by 2.5 *cm*
	Table top radius:	45 *cm*

Table 7.2: Technical specifications and appearance of the custom-designed rotating table.

7.2.3 Field Generation System

The field generation system consists of three nested pairs of quasi-square coils: Large (LC), Medium (MC), and Small (SC). Each structure features 125 windings of 1 mm copper wire (Figure 7.3).

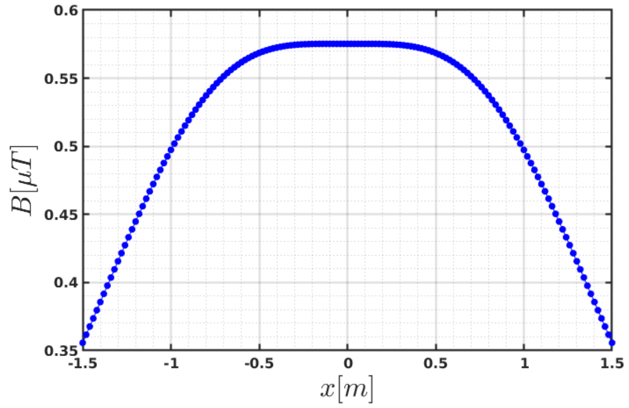

Figure 7.3: Magnetic field generated by the Large Coil (LC) pair along the symmetry axis ($I = 1\ A$). The field is sufficient to compensate for the Earth's magnetic field within the measurement volume.

Since the coils are not circular, their spacing was optimized via finite element simulations to maximize field uniformity within a spherical volume of 45 cm radius (the size of the table). The optimal distances were found to be 1.51 m for the LC, 1.49 m for the MC, and 1.47 m for the SC (Figure 7.4).

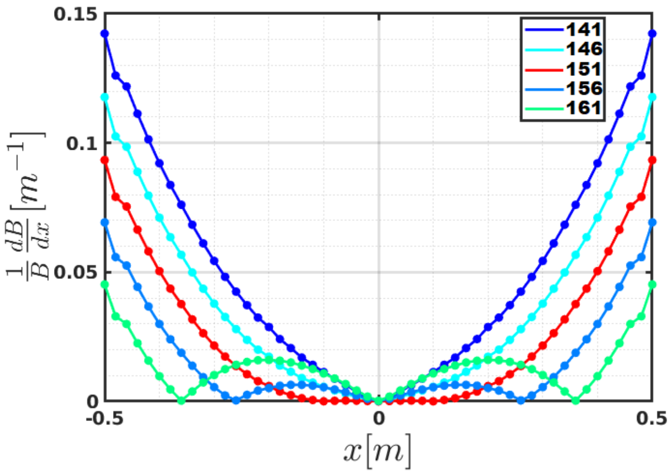

Figure 7.4: Magnetic field gradient along the symmetry axis for different coil spacings. The distance of 1.51 m was selected for the LC to minimize the gradient within the spherical region of interest.

7.3 Materials and Manufacturing

The construction of MANET posed a significant engineering challenge: to ensure high precision in magnetic mapping, the entire structure had to be non-magnetic to avoid any distortion of the field under characterization. We achieved this primarily by using high-performance polymers, such as **POM-C** and **PE-HD**.

However, for specific components subjected to high mechanical stress or requiring precise motion – namely the **slewing ring** and the **pinion** of the rotation system – the use of metallic materials was unavoidable. In these instances, **stainless steel** was selected due to its low magnetic permeability, which minimizes any residual interference with the measurements.

7.3.1 Material Selection

The physical and mechanical properties of the two polymers considered for the structure are compared in Table 7.3. Based on these parameters, the choice of material for each component was tailored to its specific functional and environmental requirements.

Mechanical proprieties	POM-C	PE-HD
Density [g/cm^3]	1.41	0.95
Yield stress [MPa]	65	22
Flexural Strength [MPa]	115	32

Thermal proprieties	POM-C	PE-HD
Melting temperature [$°C$]	+168	+128
Operating temperature (long-term) [$°C$]	< 100	< 50
Operating temperature (short-term) [$°C$]	< 140	< 80

Table 7.3: Comparison between POM-C and PE-HD mechanical and thermal properties. Operating temperatures are established with finished parts that are not under any stress in heated air, depending on the type and form of heat exposure, short-term = max. 1h, long-term = months.

POM-C was selected for the primary load-bearing components, namely the main platform and the coil support frames. This choice was primarily driven by its superior yield stress (65 MPa) and excellent dimensional stability, which are essential to maintain the structural alignment of the facility. Conversely, **PE-HD** was utilized for the sensor-support bars to minimize the total mass of the upper assembly, thereby reducing the mechanical load and inertia of the positioning system.

The use of POM-C for the coil frames was further necessitated by critical thermal constraints. Thermal simulations (Figure 7.5) indicate that during peak summer conditions at the Virgo site, the coils can reach operating temperatures of approximately 50°C. While such temperatures would approach the maximum operating limit of PE-HD, potentially compromising its structural integrity, POM-C remains perfectly stable well beyond this range. This ensures that the coil geometry remains constant even under thermal stress, preventing any systematic errors or calibration drifts during measurement campaigns.

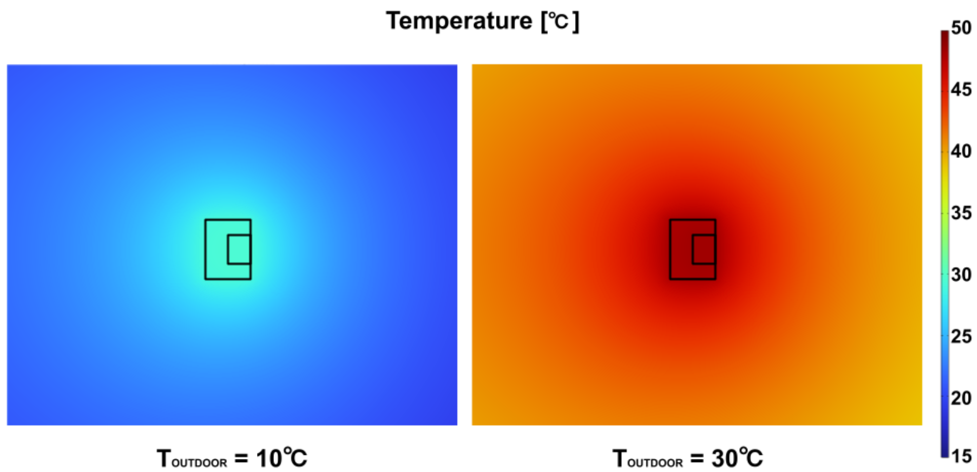

Figure 7.5: Thermal simulation of the coil structure dissipation at $I = 1\ A$ for two external temperatures ($10°C$ and $30°C$). The results confirm that POM-C remains within its operating temperature range even in summer conditions.

7.3.2 Manufacturing and Assembly Workflow

The transition from the conceptual design of MANET to its physical realization required a rigorous approach to bridge the gap between numerical simulations and laboratory requirements. A significant portion of this work was therefore dedicated to the structural and electromagnetic optimization of the facility's core components, ensuring that the theoretical magnetic performance could be maintained throughout the assembly process. The manufacturing followed a multi-step workflow:

1. **Machining:** Plastic semi-finished products were machined and refined at the University of Genoa to create the interlocking components of the coil frames and the rotating table.

2. **Integration of Standard Components:** High-precision non-magnetic commercial elements, such as the NEMA motor and the slewing ring, were integrated into the custom-designed plastic assembly.

3. **Precision Winding:** While the structural frames were developed in-house, the high-precision copper winding is currently being performed by a specialized industrial partner to ensure strict adherence to the design tolerances.

4. **Deployment and Installation:** Following the final assembly and validation in Genoa, MANET will be transported to the European Gravitational Observatory (EGO) for its final installation at the Virgo site, with full operation expected by Autumn 2026.

7.4 Measurement Protocol

To ensure the reproducibility and accuracy of the magnetic characterization, a standardized measurement protocol has been defined. This process is divided into three main phases: setup preparation, data acquisition and data processing.

7.4.1 Setup Preparation

Before starting the characterization of a device, a series of preliminary steps is required to isolate the contribution of the object under test from the environmental background:

- **Background Mapping:** A baseline measurement of the environmental magnetic field is performed in the empty facility to identify stationary noise and local gradients.

- **Background Compensation (Optional):** If the ambient field is sufficiently intense to risk saturating the fluxgate sensors, the three Helmholtz coil pairs are energized to generate a compensatory DC field, nulling the background at the center of the measurement volume.

- **Active Susceptibility Test (Optional):** In cases where the device's response to external perturbations must be evaluated, the coils are programmed to generate a specific target magnetic field (static or time-varying).

- **Sample Centering:** The device is positioned on the rotating table. The table height is then adjusted so that the expected magnetic center of the device coincides with the geometric center of the sensor array.

7.4.2 Data Acquisition

The measurement sequence is automated to achieve high spatial sampling density:

- The rotating table moves at discrete intervals of 0.44°, which represents the minimum angular step achievable given the motor's resolution and the transmission gear ratio.

- At each angular position, the triaxial magnetometers record the magnetic field components (B_x, B_y, B_z).

- By correlating the sensor readings with the rotation angle, the magnetic field produced by the device is mapped over a discrete spherical surface.

7.4.3 Data Processing

The raw data collected on the spherical surface are processed using a **multipole expansion** technique. This mathematical approach allows the complex magnetic field of a physical object to be represented as a sum of discrete magnetic moments (dipole, quadrupole, octupole, etc.).

This characterization is essential for the Einstein Telescope design effort, as it provides a compact and accurate model to calculate the magnetic coupling between the component and the sensitive suspensions of the interferometer, even when the component is placed at a non-asymptotic distance. This model allows the collaboration to determine safe installation distances and to verify if the actual emission of a device meets the strict magnetic budget requirements of the experiment.

Currently, the software implementation of this multipole expansion pipeline is under active development at the University of Genoa, representing a key contribution to the facility's analytical capabilities.

Chapter 8

The CALMA Project

As highlighted in Chapter 6, shielding the sensitive regions of the interferometer is necessary but insufficient to meet the stringent sensitivity requirements of the Einstein Telescope (ET). Furthermore, as established in Chapter 4, magnetic noise is not an intrinsic limit of the detector; rather, it arises from the coupling between environmental magnetic fields and specific interferometer components.

Paradoxically, this dependency offers a unique advantage: since the noise is generated by an interaction, it can be mitigated not only by shielding or by suppressing external sources, but also by re-engineering the coupling mechanism itself. This opens an additional, highly effective pathway for noise reduction, allowing for a more flexible and robust mitigation strategy beyond traditional shielding. From this perspective, the **CALMA** project (*Controlled And Low-noise Magnetic Actuators*) was conceived. Developed within the framework of the *INFN Grant Giovani* call, this research project aims to mitigate magnetic noise by fundamentally re-engineering the magnet-coil actuator system.

8.1 The Current Coupling Mechanism

Magnetic actuation is fundamental to the operation of the interferometer, as it allows for the active control of the longitudinal position and angular alignment of the test masses (TMs). In Virgo, this is achieved through **magnet-coil** actuators (Figure 8.2a), consisting of fixed coils integrated in a part of the suspension structure, called Reaction Mass (RM), and small Neodymium-Iron-Boron (NdFeB) permanent magnets glued to the back surface of the TM (Figure 8.1).

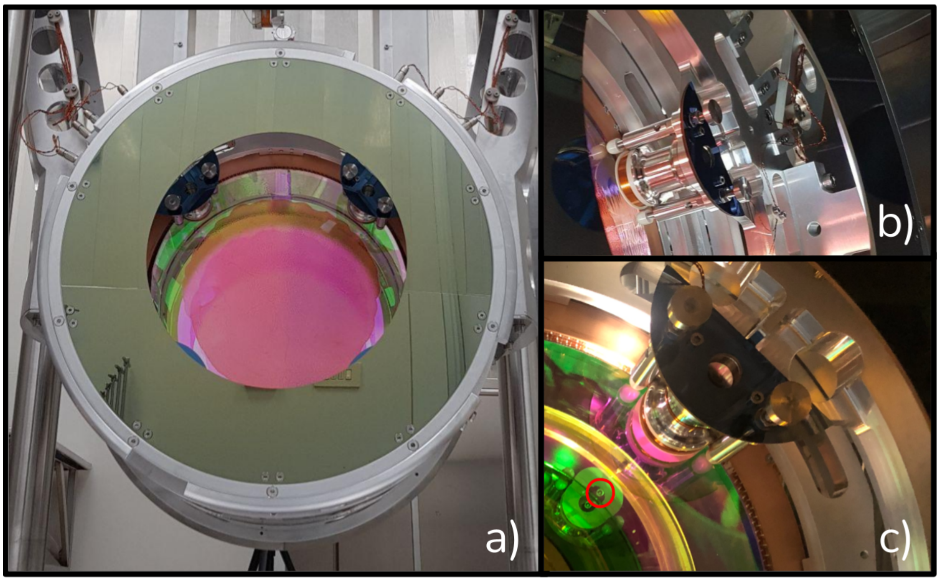

Figure 8.1: Magnet-coil actuation system. a) Rear view of the payload; b) detail of the actuation coil mounted on the reaction mass; c) close-up of the magnet bonded to the rear face of the test mass (highlighted by the red circle and visible via the reflection on the test mass surface). Image adapted from [92, 93, 94].

When a current I flows through the coil, it generates a local magnetic field whose gradient interacts with the magnetic moment $\vec{m}$ of the permanent magnet, producing the control force necessary to maintain the interferometric lock.

However, any external magnetic field also exerts a force $\vec{F}$, defined by the relationship:

$$\vec{F} = \vec{\nabla}(\vec{m} \cdot \vec{B}) \tag{8.1}$$

In the current Virgo configuration, four actuators arranged in a cross pattern are utilized. The magnets are mounted with alternating polarities (anti-parallel configuration), as shown in Figure 8.2b. This geometry was designed to nullify the total magnetic dipole moment of the test mass ($\sum \vec{m}_i \approx 0$). In this way, the mirror is theoretically insensitive to uniform external magnetic fields, as the forces exerted on the individual magnets cancel each other out.

However, the limitation of this design lies in its sensitivity to **magnetic field gradients**. If the external field exhibits spatial fluctuations on a scale comparable to the distance between the magnets, the force exerted on each of them differs, resulting in a net force or torque on the test mass. This coupling translates into displacement noise that limits sensitivity at low frequencies.

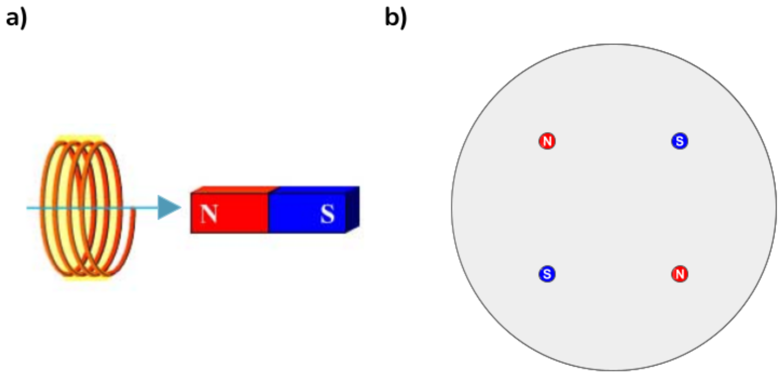

Figure 8.2: Schematic drawing of a) the magnet-coil system, b) the current arrangement of magnets on the Virgo test masses.

8.2 Exploration of New Configurations

The primary objective of CALMA is to investigate magnetic configurations that behave as higher-order multipoles. These configurations exhibit field profiles that decay significantly faster with distance, thereby drastically reducing the volume of interaction with the external environment.

The physical foundation for this approach lies in the **magnetic reciprocity principle**: a system that cannot "project" its field into the far-field is, by the same token, less susceptible to external magnetic noise originating from afar. By increasing the multipole order, the magnetic flux lines close more efficiently between adjacent poles, rendering the test mass intrinsically less sensitive to external non-uniform magnetic fields.

The exploration of new magnetic configurations follows two distinct development paths, categorized by their engineering complexity and performance potential. These paths are detailed in the following subsections, evaluating their respective performance versus implementation trade-offs.

8.2.1 Multipole Array

This approach involves a complete transition to a higher-order configuration designed to force magnetic flux lines to close locally. Depending on the mechanical and electrical constraints, this can be implemented through two main architectures:

- **Configuration 1:** Utilizing eight individual coils and eight magnets arranged in equidistantly spaced and alternating polarity pattern (Figure 8.3a). This provides maximum control over each degree of freedom but requires a significant increase in hardware and wiring complexity.

- **Configuration 2:** A more compact solution employing four ”figure-eight” shaped coils. In this design, each coil consists of two adjacent windings carrying counter-propagating currents interacting with an N-S magnet pair (Figure 8.3b). This effectively emulates a higher-order multipole while reducing the number of individual actuator units.

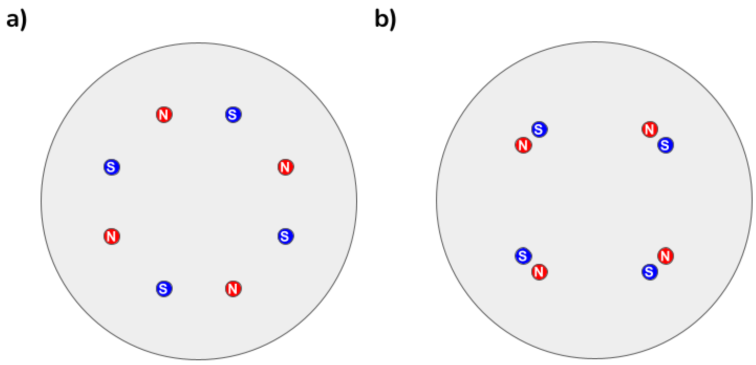

Figure 8.3: Multipole configuration with eight magnets: a) equidistantly spaced; b) arranged in opposite-polarity pairs.

Regardless of the chosen implementation, this approach acts as a true higher-order multipole, suppressing external field gradients even at short distances. However, it presents significant engineering complexities: it requires a complete redesign of the power electronics and introduces challenges in managing the actuator's degrees of freedom, as the resulting force profile becomes highly localized and sensitive to alignment tolerances.

8.2.2 Hybrid Configuration

A more conservative and minimally invasive proposal consists of maintaining the current 4-coil system while doubling the number of magnets mounted on the test mass. The magnetic arrangement is identical to that of **Configuration 1** described in the Multipole Array; however, the actuation is solely driven by the interaction between the coils and the 4 primary magnets. Specifically:

- 4 primary magnets are positioned in correspondence with the coils (e.g., all with the North pole facing outward) to ensure primary actuation.

- 4 compensation magnets with inverted polarity (South pole) are positioned in the intermediate spaces to enforce local flux closure.

This hybrid approach allows for the local closure of magnetic field lines, providing a significant reduction in far-field emission while avoiding the need for a complete redesign of the power electronics. By leveraging the existing 4-coil infrastructure, it offers a "bridge" solution that improves performance while maintaining high compatibility with the current experimental setup at the Virgo site.

To validate this hypothesis, a numerical simulation was performed as a **proof of concept** using a custom-developed MATLAB script, employing realistic geometric and physical parameters based on the Virgo detector. The simulation models a mirror radius of 17.5 cm, with actuators placed on a circle of radius $L = 14$ cm, each modeled with a magnetic moment $m = 0.05$ A·m^2. We compared the standard baseline (4-magnet configuration, acting as a quadrupole) with the proposed 8-magnet octupole design.

In the near-field (distance $d \approx 0.7$ cm), the octupole configuration exhibits a more fragmented gradient distribution (Figure 8.4).

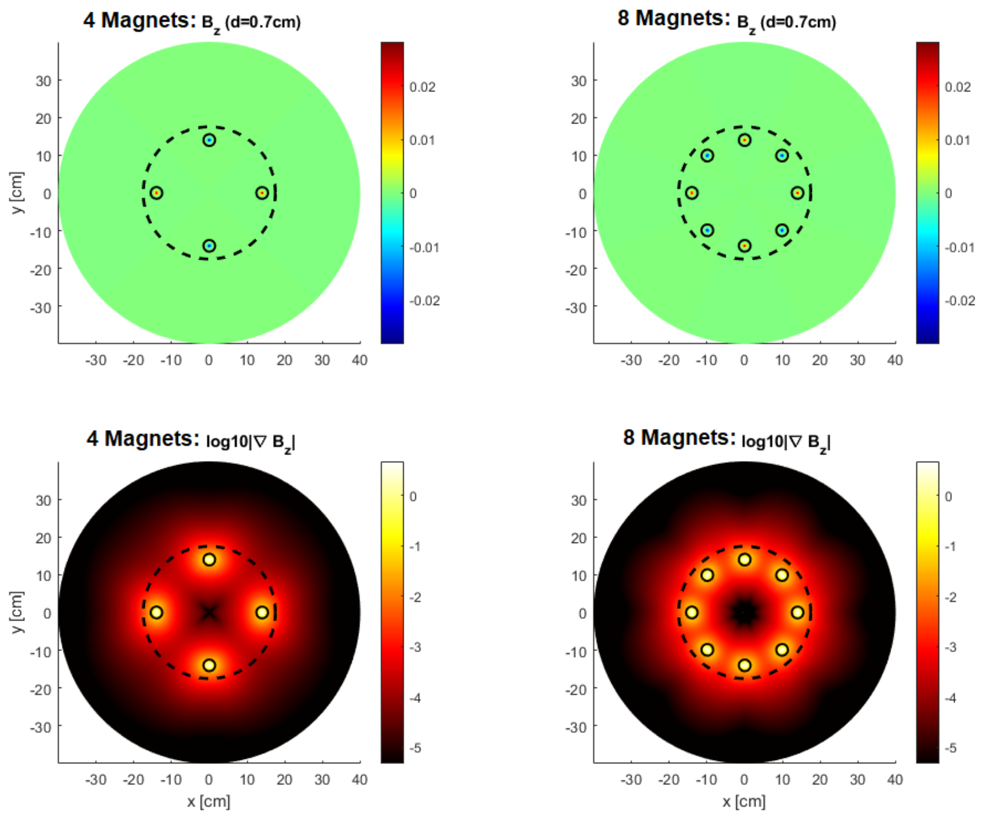

Figure 8.4: Comparison between the 4-magnet (quadrupole) and 8-magnet (octupole) configurations at 7 mm from the face of the Test Mass. Note the eight distinct gradient peaks in the octupole corresponding to the magnets (black circles).

From a control perspective, this represents a challenging trade-off: the more localized force profile requires smaller coil dimensions and higher alignment precision to prevent cross-talk between adjacent poles of opposite polarity.

However, far-field analysis confirms the efficacy of the octupole design in reducing environmental coupling. By projecting the gradient onto planes at increasing distances (Figures 8.5 and 8.6), it is observed that in the octupole, the field decays much more drastically from one plane to the next.

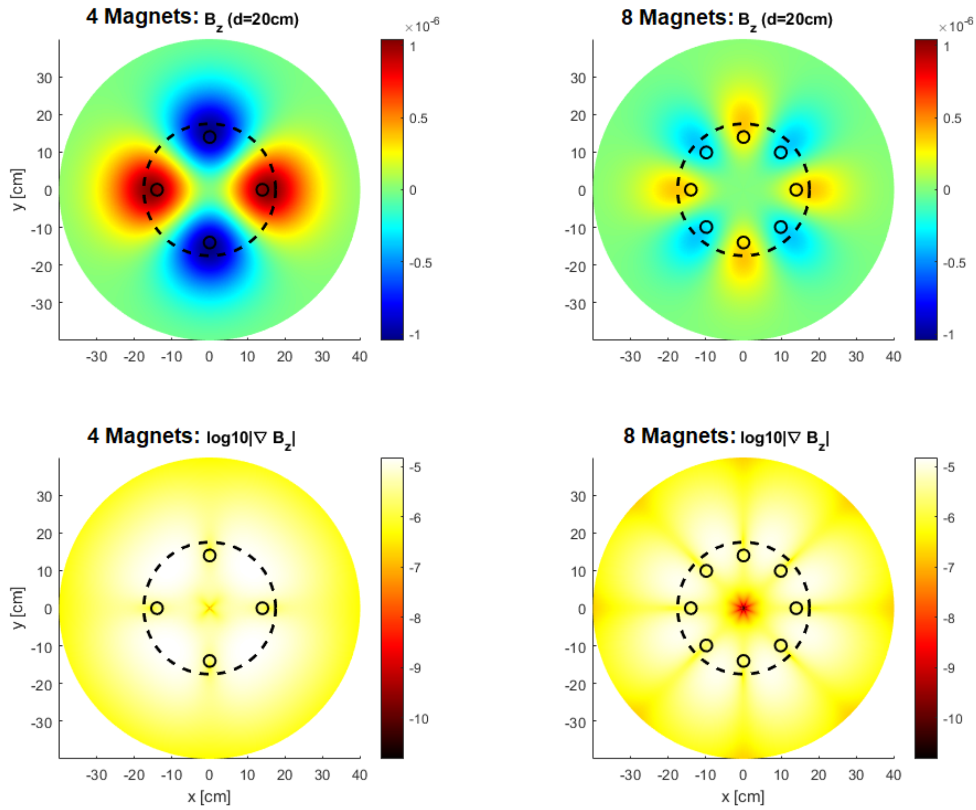

Figure 8.5: Field and gradient distribution at 20 cm from the test mass. Note the drastic reduction in magnetic intensity in the 8-magnet configuration compared to the standard one.

Therefore, while at close distances the 8-magnet configuration may still exhibit a significant gradient magnitude due to the proximity of the sources, at greater distances, multipolar cancellation takes over.

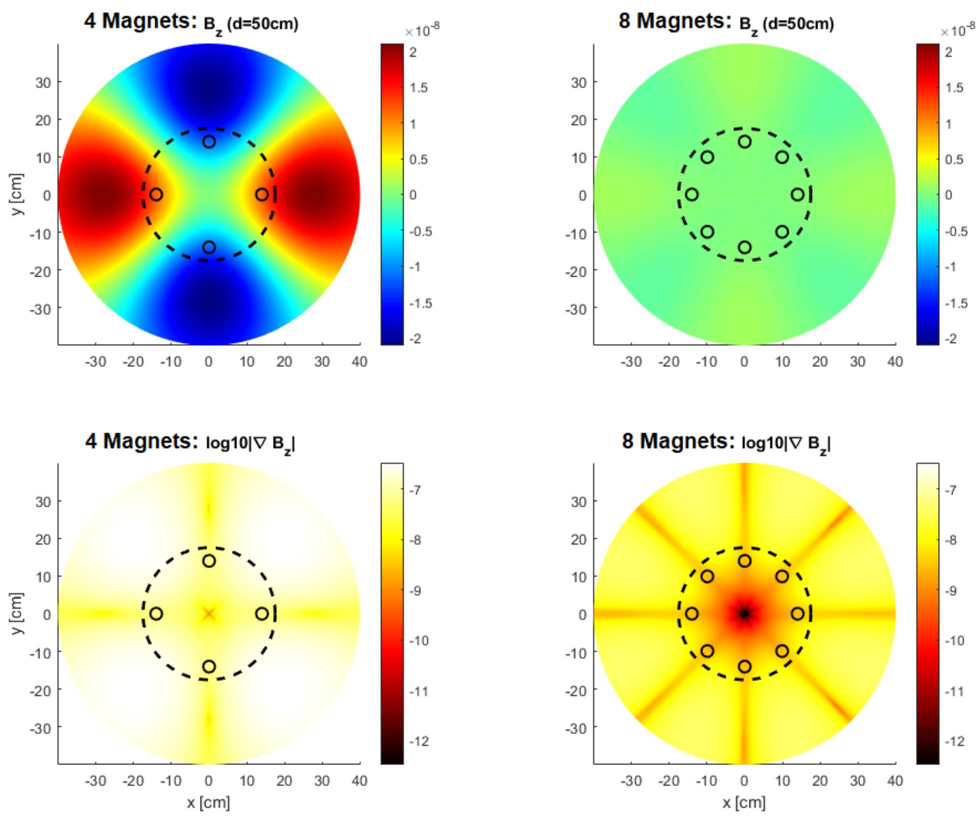

Figure 8.6: Field and gradient distribution at 50 cm. The octupole field is almost completely extinguished, and the gradient is orders of magnitude smaller than that of the quadrupole.

This behavior is summarized in the 1D decay plot (Figure 8.7). The change in slope observed in the plot at $z \approx 14$ cm represents the limit of the multipole approximation's validity:

- *Near-field ($z < L$).* The contribution of individual magnets is dominant, and the system geometry has not yet collapsed into a point source.
- *Far-field ($z > L$).* The solid angle subtended by the magnets decreases drastically. In this region, destructive interference between opposite poles becomes the dominant effect, stabilizing the slopes at the theoretical values of z^{-4} (quadrupole) and z^{-5} (octupole).

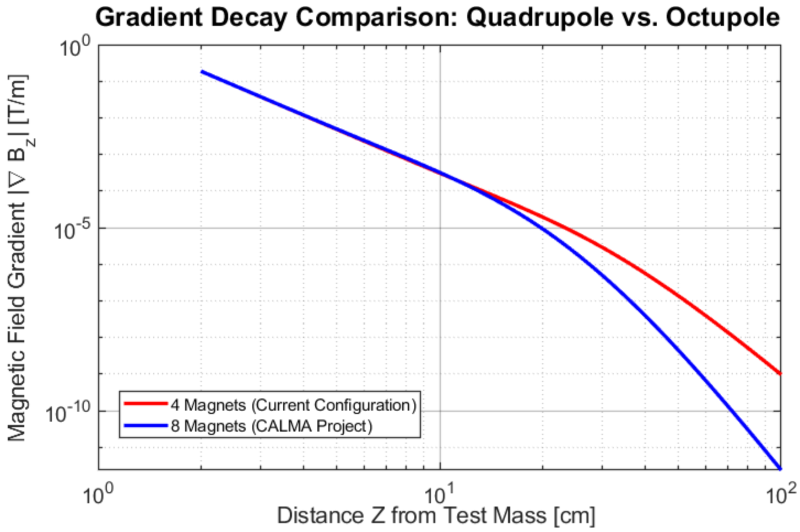

Figure 8.7: Decay of the gradient $|\nabla B_z|$ as a function of the distance z along the magnet axis. The steeper slope of the octupole confirms the multipolar confinement. The 1D decay profile was calculated along the longitudinal z-axis starting from the radial coordinate $r = L$, i.e., at the position of one of the actuator magnets. This choice represents the most critical condition for noise coupling, as it is the region where the local field is at its maximum.

The superior efficiency of the octupole does not depend solely on the multipole order, but also on the reduction of the distance between adjacent magnets:

- In the quadrupole, the magnets are spaced by 90° ($d_{quad} \approx 19.8$ cm).
- In the octupole, the spacing decreases to 45° ($d_{oct} \approx 10.7$ cm).

As the opposite poles are closer together, the magnetic flux lines close between them at much lower z altitudes compared to the quadrupole. This "early suppression" phenomenon allows the octupole to reduce magnetic noise even in the transition zone, making the system intrinsically quieter even at intermediate distances.

Although the CALMA project was not funded in the last grant cycle, the scientific validity of the approach remains intact. The reduction of the coupling factor represents, along with shielding, the second fundamental pillar to ensure that magnetic noise does not mask astrophysical signals in next-generation detectors.

Chapter 9

Electrostatic Noise

The term electrostatic noise refers to the noise generated by the coupling between a test mass (TM) and the surrounding electronics.

As with magnetic noise, the terminology is slightly misleading: this is not an intrinsic limit of the interferometer. Under ideal conditions, a test mass is electrically neutral and thus immune to coupling with static or low-frequency external electric fields. In practice, however, detectors such as LIGO and Virgo consistently observe a noise floor limit that is highly correlated with charge deposition on the TMs [30, 36]. In particular, in Virgo at the end of the O3 preparation phase, it was discovered that test masses exhibited electrical charging, with surface density values on the order of several tens of pC/cm^2 [30]. Furthermore, the charge distribution was found to be non-uniform across the dielectric surface of the mirrors [30, 38].

9.1 Electrostatic Noise Sources

At present, the physical phenomenon at the origin of charge deposition remains unidentified with certainty. Technical literature and in situ experience suggest several hypothetical scenarios [38, 40]:

- **Triboelectricity during vacuum phases:** Molecular friction of the residual gas against the mirror surface during vacuum evacuation (*pump-down*) or venting phases of the vacuum chamber [39].
- **Cosmic Ray Ionization:** Interaction of high-energy particles with the fused silica substrate, capable of generating net charges on the surface or within the dielectric volume [38, 40].
- **Particulate Contamination:** Deposition of microscopic charged dust

particles that adhere to the mirror surface through electrostatic attraction [34].

Despite these hypotheses, no measurement has ever been performed capable of experimentally determining the actual deposition mechanism. Hence the need to introduce a monitoring system that, in addition to quantifying the charge, allows for the identification of its temporal dynamics. Understanding whether the accumulation is associated with specific operational phases or occurs continuously would provide crucial clues to distinguish between mechanisms linked to procedures (such as vacuum pumping) or stochastic environmental events (such as cosmic rays).

9.2 Electrostatic Noise Coupling

The presence of surface charge has a different impact on different detectors, depending on the configuration of the actuation system.

In the case of **LIGO**, in addition to magnetic actuators, there are electrostatic actuators (ESD) that act directly on the test mass [95, 96]. The deposited charge distorts the actuation fields and alters the system response, heavily impacting the noise budget and the stability of the interferometric control [35, 36].

Conversely, in **Virgo**, the actuators are purely magnetic [49]. In an ideal condition where all surrounding electronics are perfectly grounded, electrostatic noise should not exist due to the lack of a coupling electric field. However, the noise detected during the O3 preparation phase [30] in Virgo was generated by the presence of floating potentials on the payload. In such a configuration, the charge on the mirror acts as a transducer for the potential fluctuations of these isolated metallic components. Although restoring the grounds temporarily eliminated the problem, the charge remains a latent vulnerability: any degradation of the contacts or the presence of AC electric fields in the test mass area would immediately reactivate this coupling channel.

The impact of electrostatic noise is primarily concentrated in the low-frequency range (typically below 50 Hz). This frequency localization is a direct consequence of the mechanical response of the suspension system: the test mass, being the final stage of a multi-stage pendulum chain, acts as a low-pass filter for external forces. Consequently, any stochastic force resulting from the interaction between the surface charge and surrounding electric fields is amplified by the mechanical resonance of the suspension and remains a dominant noise source only where the isolation provided by the chain is not yet total [30, 40].

The experimental impact of these effects is reflected in the overall sensitivity evolution of Advanced Virgo. Figure 9.1 shows the sensitivity curves during the O3 run; the visible improvement in the low-frequency range between O3 preparation phase and O3b is the result of a broader commissioning effort. While this gain stems from multiple concurrent upgrades – including the mitigation of scattered light and the optimization of angular controls – the resolution of the floating potential issues was a critical step in cleaning the 10-100 Hz band from the specific electrostatic coupling identified at the end of the O3 preparation phase [30].

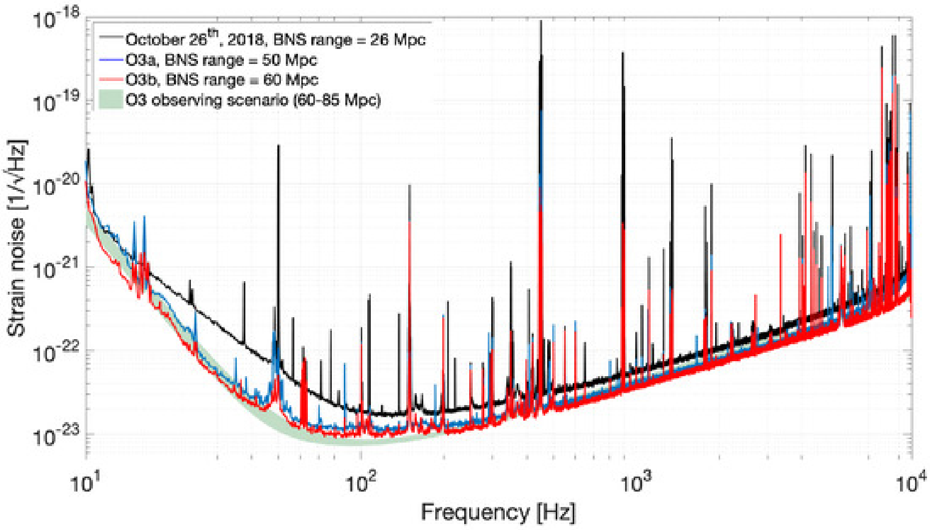

Figure 9.1: Sensitivity curves of Advanced Virgo during the O3 observing run. The transition from O3 preparation phase (black curve) to O3b (red curve) highlights the sensitivity gain achieved through various commissioning interventions. The mitigation of electrostatic noise via the grounding of floating potentials was one of the key contributors to the reduction of the noise floor in the low-frequency region. Image reproduced from [30].

9.3 Electrostatic Noise Budget in GW Detectors

The current Virgo Noise Budget does not include a curve for electrostatic noise, essentially treating it as an unknown variable mitigated a posteriori. This gap becomes critical in the perspective of the **Einstein Telescope**.

In ET, the use of cryogenic sapphire mirrors introduces new complexities: surface conductivity at low temperatures changes drastically, making current discharge techniques less predictable [97]. Without a continuous monitoring system, the ET Noise Budget for low frequencies will remain affected by unacceptable uncertainty, risking the masking of astrophysical signals or making control systems inefficient.

The transition from reactive management to predictive diagnostics is the objective of the system proposed in this work: transforming electrostatic charge from an environmental unknown into an observable physical variable, enabling intelligent control strategies for next-generation detectors.

Chapter 10

Monitoring System

The presence of noise associated with charge deposition on the test mass, combined with the current limited understanding of the underlying physical mechanisms, underscores the need for a real-time charge monitoring system. Such a system must be capable of determining both the magnitude and the spatial distribution of the charge on the test mass. By tracking the dynamics of charge accumulation, we can assess whether the process is continuous or correlated with specific interferometer activities, thereby providing valuable insight into its origin. Moreover, a monitoring system is essential for the effective deployment of any charge-mitigation device, as it provides the only means to verify its performance and efficiency.

This chapter presents two distinct monitoring approaches. The first is a **passive system**, where dedicated sensors measure the potential induced by the charge on the test mass. The second is an **active system**, which utilizes electrostatic actuators to exert a controlled force on the test mass, effectively employing the interferometer itself as a high-precision sensor.

The passive system serves primarily as a *proof of concept*, demonstrating how neural networks can be leveraged to reconstruct the charge distribution. In contrast, the active system is designed to overcome the practical implementation constraints encountered in the passive configuration.

Portions of this chapter, including figures and results, have been adapted from the author's previous work published in *"Gravitational Wave Science with Machine Learning"* [98].

10.1 The First Monitoring System: Passive Approach

The first monitoring system is based on the correlation between the surface charge distribution on the test mass (TM) and the electric potential induced on a series of dedicated sensors positioned in its vicinity. The objective is to solve the associated **inverse problem**: reconstructing the source characteristics – specifically the charge distribution – starting from discrete potential measurements.

However, accurately mapping the potential back to the charge distribution is computationally and analytically challenging due to several factors:

- The complex geometry of the system, which introduces non-linearities in the electric field distribution;
- The high dimensionality of the source space, given the virtually infinite degrees of freedom of a generic surface charge;
- The limited number of sampling points (sensors), which may lead to degenerate solutions where different charge configurations produce equivalent potential readings.

To overcome these analytical limitations, assumptions regarding the shape of the distribution are necessary. In this work, the charge is modeled as a **localized Gaussian distribution**. This choice is motivated by experimental evidence, which suggests that charge accumulation on test masses is typically non-uniform and localized [30].

To map the non-linear relationship between the measured potentials and the Gaussian parameters – namely position, intensity, and standard deviation – **Neural Networks (NNs)** are employed.

The workflow is organized as follows: first, an optimal sensor configuration is determined to maximize the information content regarding the charge distribution. Second, the selected geometry and its electrostatic behavior are modeled using COMSOL Multiphysics to generate a comprehensive dataset. Subsequently, the neural network architecture is presented, and the dataset is employed for training and validation purposes. Finally, the results of the reconstruction are discussed.

10.1.1 Sensor Placement Optimization

A critical challenge in designing the monitoring system is determining the optimal number and placement of sensors. While a high number of sensors theoretically provides more information, practical constraints within the Virgo payload – such as limited physical space and the need to minimize disturbances near the TM – require a strategic minimization of the sensing hardware.

The starting point for this optimization was the identification of **32 candidate sites**, corresponding to the pre-existing holes in the metallic structure surrounding the test mass. The spatial distribution of these sites is shown in Figure 10.1, where the labels indicate the position relative to the mirror (f: front, b: back, r: right, l: left).

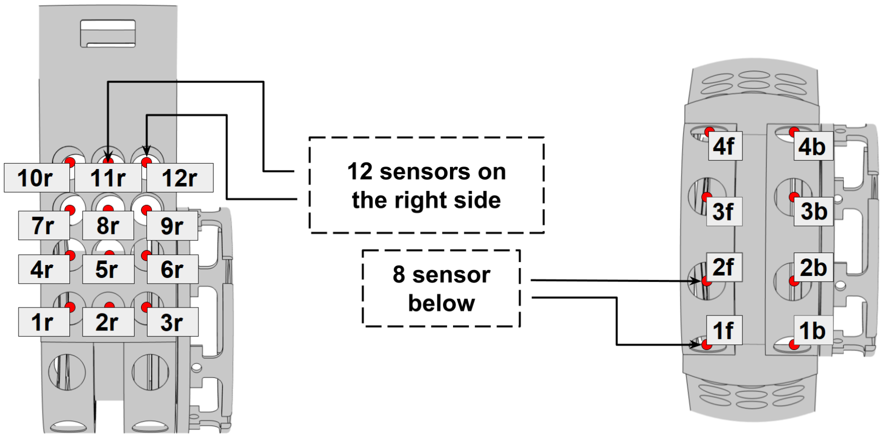

Figure 10.1: In red, the possible sensor locations in the West End (WE) payload. The sensors on the left of the Test Mass (TM) are mirrored counterparts of those on the right shown in the figure. Image adapted from [98].

To identify the most informative subset of sensors and avoid redundant data, three selection criteria were developed.

Two of the methods leverage **Principal Component Analysis (PCA)**, a technique that transforms the raw sensor data into a new coordinate system of uncorrelated variables called Principal Components (PCs), ranked by the amount of variance they explain.

- **Importance Method:** This criterion ranks sensors based on their cumulative contribution to the most informative PCs, weighted by the percentage of variance each PC explains.

- **Loadmax Method:** The goal is to preserve as many distinct PCs as possible by retaining the most significant sensor for each PC. For the first sensor, we prioritize the one contributing most to the first PC; for the second sensor, the one contributing most to the second PC, and so forth.

- **Mincorr Method:** This method starts by selecting the most "important" sensor using the Importance Method and then chooses subsequent sensors based on having the **minimum correlation** with those already selected. This explicitly limits information redundancy.

The use of multiple selection criteria stems from the fact that no single sensor set is "optimal" in absolute terms. As will be shown, certain configurations are more effective for capturing specific features, while others are better suited to different monitoring objectives.

10.1.2 Dataset Generation and COMSOL Modeling

The dataset was generated through a massive campaign of numerical simulations conducted in the **COMSOL Multiphysics** environment.

The simulated model includes the **Test Mass** (TM) and the structural elements in its immediate vicinity: the **Ring Heater** (RH), the **Large Baffles** (LBs), and the **Actuator Cage** – the metallic structure surrounding the test mass that houses critical components, such as the coil actuators for precision control (Figure 10.2).

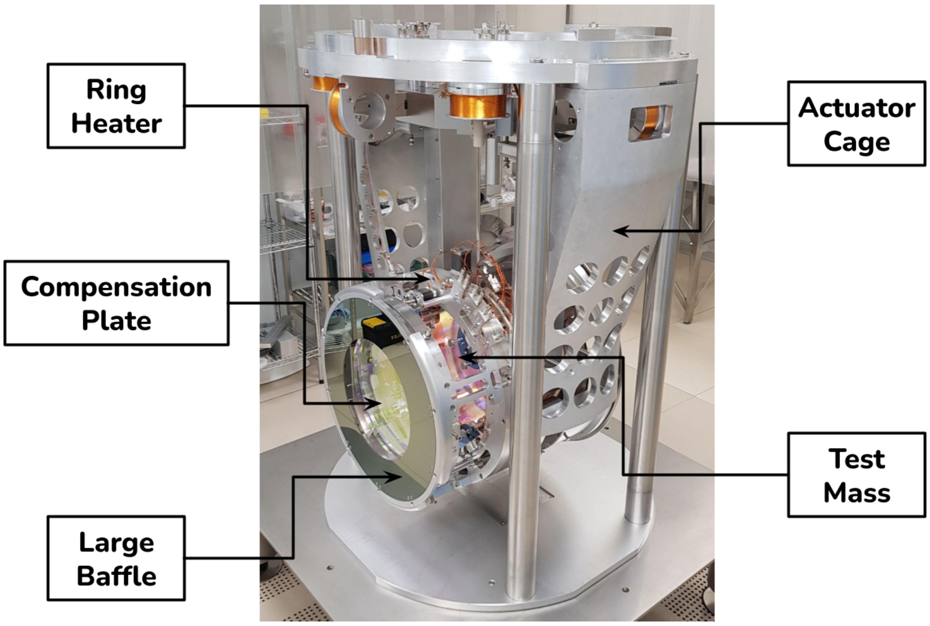

Figure 10.2: WI Payload configuration in the cleanroom. The view shows the Compensating Plate (CP) surrounded by the circular Large Baffle (LB). The fused silica Test Mass is located immediately behind it. The upper structure houses the Ring Heater (RH) for thermal control. The Actuator Cage, which supports the components for micrometric positioning and beam steering, surrounds the entire system. Image adapted from [99].

The geometry was derived from the original CAD files of the West End (WE) tower of the Virgo interferometer. A **top-down simplification** approach was followed to remove sub-millimetric details (fasteners, threads, fillets) that would cause numerical instabilities. Furthermore, a **manual re-modeling** phase was carried out to reconstruct complex elements like the large rear baffle from scratch, ensuring smooth surfaces and controlled thicknesses for optimal mesh compatibility (Figure 10.3).

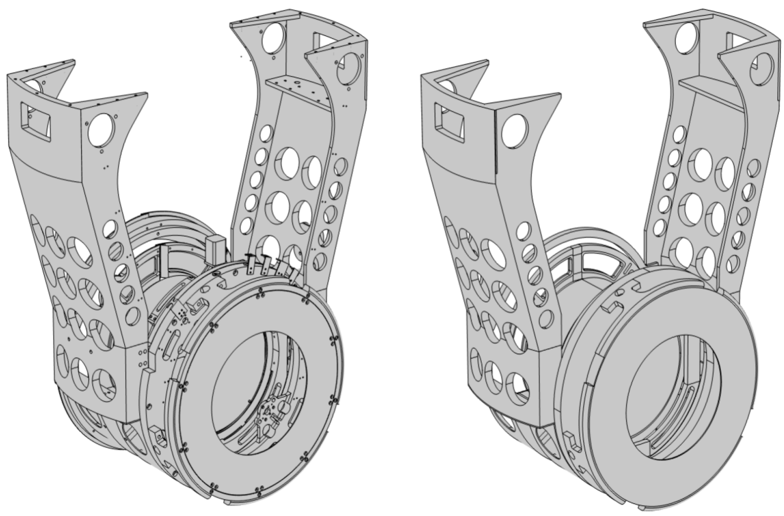

Figure 10.3: Comparison between the original CAD (left) and the simplified simulated geometry (right). Image reproduced from [98].

The TM was modeled as fused silica ($\epsilon_r = 3.75$), while the payload and baffles were set to **Ground** ($V = 0$).

In line with the strategy described in Chapter 3, the domain was discretized using a fully tetrahedral mesh. Although structured elements could theoretically be applied to the cylindrical geometries of the TM and RH, a uniform tetrahedral approach was maintained to ensure seamless transitions at the complex interfaces and gaps. This choice, combined with the local refinement in high-gradient regions mentioned earlier, allowed for an optimized distribution of Degrees of Freedom (DoF), ensuring the necessary resolution for the simulation campaign.

A visual comparison of two representative simulated cases is provided in Figure 10.4. The figure highlights how the neural network must handle significantly different spatial distributions: from highly localized spots with low total charge to broader, more intense distributions that cover a larger portion of the test mass surface.

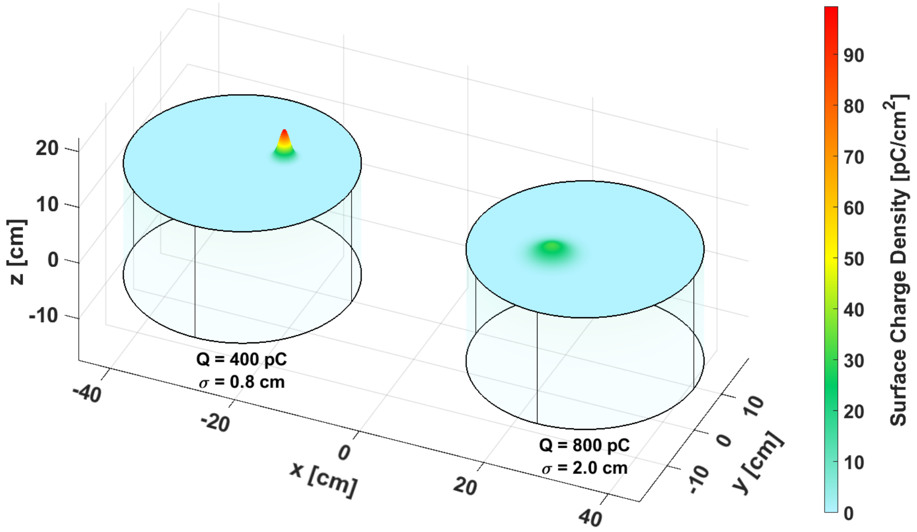

Figure 10.4: Visual representation of two simulated Gaussian surface charge distributions on the Virgo TM. The left panel shows a more localized distribution with lower total charge ($Q = 400$ pC, $\sigma = 0.8$ cm), while the right panel illustrates a more intense but more diffused distribution ($Q = 800$ pC, $\sigma = 2.0$ cm).

To create a robust training set, more than 100 000 **different Gaussian charge distributions** were simulated. The parameters were varied within the following physical ranges:

- **Total Charge (Q):** from 1 pC to 800 pC;
- **Standard Deviation (σ):** from 0.1 cm to 2.0 cm;
- **Position:** randomly distributed across the surfaces of the front and back faces of the TM.

10.1.3 Neural Network Architecture

Given the complexity of the inverse problem and the non-linear nature of the system, a **modular architecture** was adopted. Rather than relying on a single monolithic network, the system consists of a suite of specialized networks operating in parallel to solve distinct sub-tasks.

Categorical Networks.

Three independent **categorical networks** were developed to extract **dichotomous information** regarding the charge distribution:

- **Face Discrimination:** Determines whether the charge resides on the front or back face of the Test Mass.
- **Horizontal Discrimination:** Identifies whether the charge center is in the right or left hemisphere, regardless of the face.
- **Vertical Discrimination:** Determines if the charge is deposited on the upper or lower part of the TM.

The training and validation process was implemented in **MATLAB** using the *Deep Learning Toolbox*. Architecturally, these are **shallow neural networks** comprising a single hidden layer of **20 neurons** with **ReLU** activation functions. Training was performed using the **BFGS** (Broyden-Fletcher-Goldfarb-Shanno) algorithm. As a quasi-Newton method, it provides faster convergence and higher numerical precision for networks of this size compared to standard gradient descent algorithms.

To ensure stability, the input data were pre-processed using **z-score normalization**. This centers the sensor potential readings around a zero mean with unit standard deviation, preventing sensors with higher absolute potential values from disproportionately biasing the network and ensuring the NNs focus on the relative spatial variations of the electric field.

Regression Networks.

In parallel, two neural networks were trained to estimate continuous physical parameters:

- **Charge Intensity (Q):** This is the most critical metric for monitoring deposition rates over time and verifying the efficiency of discharging procedures.
- **Standard Deviation (σ):** This network estimates the spatial width of the Gaussian distribution. This parameter is inherently difficult to reconstruct due to solution degeneracy, where different spatial extensions can produce nearly identical sensor signals.

The regression networks also feature a single hidden layer of **20 neurons**. Unlike the categorical modules, they utilize a **hyperbolic tangent sigmoid** activation function, which is better suited for mapping continuous, non-linear relationships. Training was performed using the **Levenberg-Marquardt** algorithm. This optimization method is specifically designed for minimizing sum-of-squared errors in non-linear problems, providing superior convergence speed and stability when estimating physical parameters.

Notably, the estimation of exact (x, y) coordinates was not implemented. For current charge mitigation strategies, the sector-based information provided by the categorical networks is sufficient and significantly more robust than a continuous spatial regression, which would be highly susceptible to experimental noise.

10.1.4 Results

The optimization process yielded distinct sensor rankings for each of the three criteria. **Table 10.1** illustrates the comparison between the *Importance*, *Loadmax*, and *Mincorr* methods.

Sensor Ranking Comparison		
Importance	**Loadmax**	**Mincorr**
3f	1b	3f
2f	4f	10r
2r	1f	10l
2l	3r	11r
5l	2f	11l
...	...	...

Table 10.1: Sensor ranking from most to least informative according to Importance, Loadmax, and Mincorr criteria. The complete ranking can be found in [98].

To evaluate the predictive power of these subsets, NNs were tested at varying Signal-to-Noise Ratios (SNR) using only the top four sensors identified by each criterion.

As shown in **Figure 10.5**, the reconstruction of the total charge Q is remarkably robust across all criteria, with the Mean Squared Error (MSE) decreasing consistently as the SNR improves. In contrast, the spatial spread σ proves significantly more difficult to determine.
The poor performance in estimating σ is an intrinsic feature of the inverse problem: different spatial extensions of the same total charge can produce nearly identical potential signatures at the sensor locations, leading to a mathematical degeneracy that even the NN struggle to resolve.

Regarding spatial localization, the categorical networks (**Figure 10.6**) demonstrate that the choice of sensors is task-dependent. For instance, the *Loadmax* subset excels in discriminating whether the charge is on the front or back face (achieving $> 85\%$ accuracy at high SNR), while other configurations are better suited for vertical or horizontal positioning.

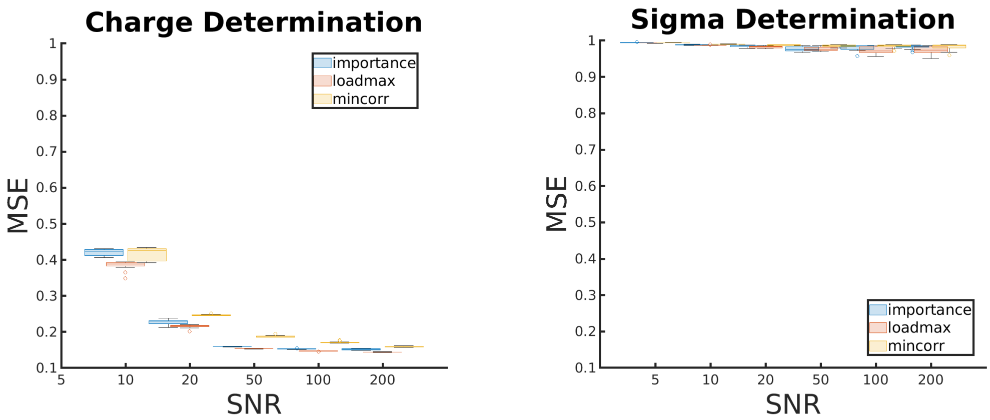

Figure 10.5: MSE in charge value (Q) and standard deviation (σ) estimation for different NNs at varying SNR. Input data are z-score normalized. Image reproduced from [98].

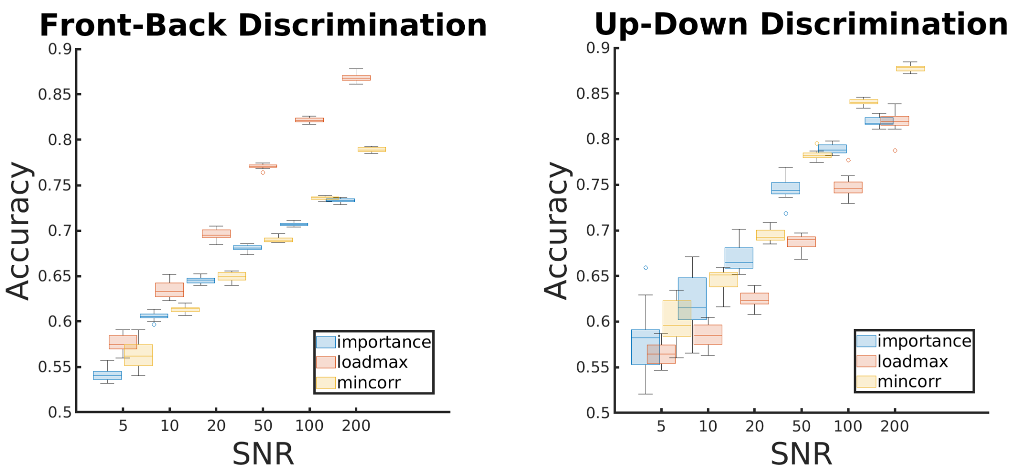

Figure 10.6: Accuracy in Front-Back and Up-Down discrimination at varying SNR. Image reproduced from [98].

This diversity implies that the "best" monitoring layout depends on the chosen mitigation strategy. If a directional discharging method, such as a localized electron gun [100], is employed, precise localization is the priority. Conversely, if a non-directional method like an ion-gas cloud [101] is used, the total charge Q becomes the primary parameter of interest.

10.1.5 Discussion

The results presented above, also detailed in our contribution to the monograph on Artificial Intelligence (AI) in physics [98], demonstrate that Neural Networks are an exceptionally flexible tool for solving inverse problems in charge monitoring and provide theoretical proof that AI can effectively reconstruct complex charge distributions. This operational approach (summarized in **Figure 10.7**) is inherently portable: the same architecture can be retrained for any geometry, provided a sufficient synthetic dataset is available.

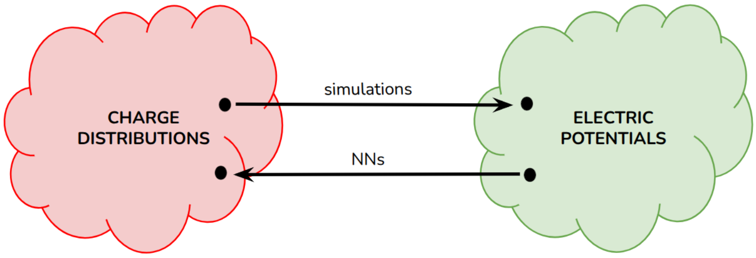

Figure 10.7: Mapping the problem: simulation moves from charge space to measurement space; NNs perform the inverse mapping.

However, a fundamental physical limitation emerges when confronting these simulated results with experimental reality. Based on charge levels typically measured at Virgo [30], the electric potentials induced on passive point sensors often fall below the detection threshold of current low-noise electronics. In practical terms, the "measurement space" depicted in **Figure 10.7** is frequently dominated by electronic noise, rendering the monitoring system blind to small but significant charge depositions.

To overcome this barrier, a paradigm shift is required: transitioning from **passive potential sensing** to **active force sensing**. This transition forms the basis of the second monitoring system.

10.2 The Second Monitoring System: Active Approach

The core idea of the second system involves replacing passive sensors with potential generators (electrodes) and measuring the resultant **mechanical force** exerted on the test mass, rather than the induced potential. This approach offers two transformative advantages:

1. **Interferometric Precision**: By using the interferometer itself as the sensor, we leverage a displacement sensitivity on the order of 10^{-19} $\mathrm{m}/\sqrt{\mathrm{Hz}}$. This allows for the detection of forces orders of magnitude smaller than what can be inferred via electronic potential measurements.

2. **Computational Continuity**: The logic of the inverse problem remains. We "simply" substitute the potential measurement space with a force measurement space in our NN training.

As discussed in [98], this framework partially resolves the degeneracies that plagued the first system. By strategically selecting and modulating the potentials injected into the electrodes, we can "interrogate" the charge distribution from multiple electrical perspectives, effectively resolving ambiguities in the spatial reconstruction.

It is important to note, however, that this framework is conceptually distinct from the previous one. In the first system, the neural networks acted as an "inverse function" of the simulations, mapping measured effects back to their origins. In this second approach, the chosen potentials serve as a common input for both the simulations and the neural networks (**Figure 10.8**), shifting the focus towards a more active and controlled characterization of the system.

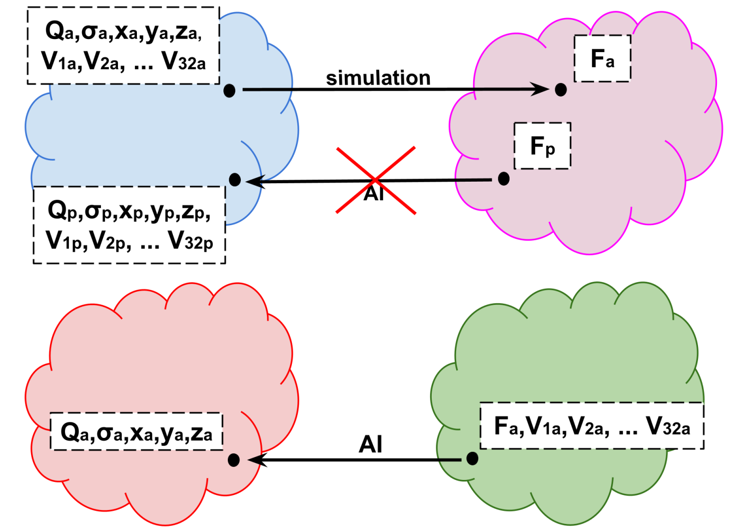

Figure 10.8: Active sensing mapping: the NN deduces the charge configuration given the known injected potentials and the measured force.

10.2.1 Advanced Virgo+ Phase II Upgrades

This monitoring system was officially presented in 2025 as a key deliverable of the Vacuum sub-system (**VAC.08 — Electrostatic mirror charge measuring system**) within the framework of the **Advanced Virgo+ Phase II** upgrades.

In view of an effective experimental deployment, which includes both numerical simulations and validation on a dedicated **mockup**, a specific configuration of **8 active electrodes** has been defined *a priori*.

To maximize the induced force along the beam direction – the axis where the interferometer exhibits maximum sensitivity – the electrode installation sites were moved away from the lateral sides of the payload cage. This reconfiguration also addresses the **information redundancy** observed in earlier studies, where symmetrically placed sensors provided nearly identical data, failing to break the spatial degeneracy of the charge distribution.

To minimize the structural impact on the payload and ensure non-invasive integration, a hybrid approach was adopted for the 8 electrodes:

- **4 dedicated active electrodes** are installed on the mechanical support of the internal front baffle (Figure 10.9). This location ensures safe clearance from the laser beam while allowing direct electrostatic interaction with the mirror's face.

- **4 electrodes are integrated into the existing coil actuators**. By modifying the driving electronics, the coils used for standard magnet-coil actuation can function as electrostatic electrodes. This allows the system to "interrogate" the charge distribution without adding extra mass or complex mechanical components near the Test Mass.

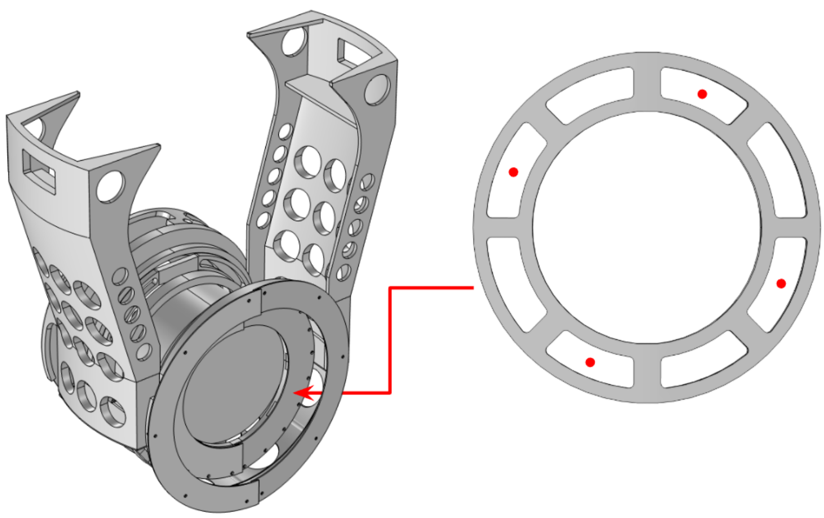

Figure 10.9: On the left, a simplified model of the test mass. On the right, a close-up view of the mechanical support for the inner front baffle, with electrode positions highlighted in red.

This 8-electrode layout defines the final **input vector** for the second generation of monitoring NNs. By modulating the potentials $V_1, \dots, V_8$ and measuring the resulting longitudinal force F_z, the network can resolve charge parameters with a precision that exceeds the first system's capabilities by several orders of magnitude, effectively transitioning the monitoring technology from a theoretical study to a deliverable ready for AdV+ Phase II integration.

Conclusion

The analysis conducted in this research work highlights that low-frequency electromagnetic noise in gravitational-wave interferometers remains a phenomenon that is far from being fully understood, let alone exhaustively mitigated. Historically less investigated than other noise sources, this noise currently suffers from a lack of consolidated mitigation strategies, particularly regarding its systematic integration into existing and future experimental infrastructures.

This study aimed to provide a systematic investigation of this subject, seeking to bridge the gap between theoretical frameworks and practical implementation. While the phenomenological state of the art has been delineated, the practical application of established mitigation techniques, such as ferromagnetic shielding, has been addressed in depth. The results demonstrate that implementing such solutions in extreme-precision environments necessitates *ad hoc* studies, as standard configurations often prove insufficient to meet the stringent sensitivity requirements of the field.
A key finding of this work concerns the decisive role of geometric detail, even within the numerical modeling phase. Simulations performed on test mass tower shielding revealed that the presence of functional openings drastically reduces the shielding factor. This degradation is further amplified during the transition from ideal models to physical realization: the case study of the Faraday isolator shielding highlighted how material non-idealities and assembly tolerances can lead to a discrepancy of more than an order of magnitude between simulated and experimentally measured shielding factor values.

Furthermore, this thesis emphasizes that the complexity of the problem necessitates a multidirectional approach. The limitations identified in the shielding of the towers indicate that merely protecting sensitive components is insufficient. In this context, the **MANET** facility emerges as an essential tool for the preventive characterization of sources, enabling the identification of critical components that require corrective intervention at the root. Concurrently, the **CALMA** project proposes a paradigm shift focused on reducing intrinsic coupling through the redesign of magnetic actuators, thereby addressing one of the primary root causes of magnetic noise.

Another significant outcome is the necessity of developing custom instrumentation, dictated by the absence of standard technology suitable for these specific applications. The resulting need for dedicated infrastructure, such as the MANET facility, underscores that managing electromagnetic noise requires a considerable investment of time and resources, as generic commercial solutions are inadequate for the required precision levels.

To this is added an incomplete understanding of the sources themselves. As observed in the case of electrostatic noise, the fundamental mechanisms leading to charge deposition are not yet fully understood. Moreover, the complexity of the system currently precludes an accurate modeling of the noise budget, necessitating further and more profound phenomenological studies.

In conclusion, a significant gap exists between the theoretical perception of the problem and the engineering effort required for its resolution. This work establishes an indispensable line of research for the design of third-generation interferometers. For the **Einstein Telescope** in particular, electromagnetic noise mitigation must be addressed *by design*: underestimating this challenge during the structural design phase would result in prohibitive future corrective costs, with the risk that such interventions may no longer be feasible if they require structural modifications.
While the results of this research provide a critical starting point, current understanding remains insufficient to provide a complete solution; further investigation is imperative to ensure that ET is not ultimately limited by its own electromagnetic environment.

List of Acronyms

AdV Advanced Virgo
AI Artificial Intelligence
ASD Amplitude Spectral Density
BBH Binary Black Hole
BH-NS Black Hole-Neutron Star
BNS Binary Neutron Star
CF Coupling Function
CP Compensating Plate
EGO European Gravitational Observatory
ESD Electrostatic Drive
ET Einstein Telescope
FE Finite Elements
GR General Relativity
GW Gravitational Wave
IF Interferometer
IMC Input Mode Cleaner
IMP Input Mirror Payload
KAGRA Kamioka Gravitational Wave Detector
LB Large Baffle
LC Large Coil
LIGO Laser Interferometer Gravitational-Wave Observatory
MANET Magnetic Noise test facility for ET
MC Medium Coil
NN Neural Network
O1 First Observing run
O2 Second Observing run

O3 Third Observing run
O3a First part of O3
O3b Second part of O3
O4 Fourth Observing run
O5 Fifth Observing run
PAY Payload
PC Principal Component
PCA Principal Component Analysis
PE-HD High Density Polyethylene
POM-C Polyoxymethylene Copolymer
RH Ring Heater
RM Reaction Mass
S6 Sixth Science run of LIGO
SA Superattenuator
SC Small Coil
SF Shielding Factor
SF$_{(P)}$ Pointwise Shielding Factor
SGWB Stochastic Gravitational Wave Background
SNR Signal to Noise Ratio
SQL Standard Quantum Limit
SR Schumann Resonance
TM Test Mass

Bibliography

[1] J. Weber. Detection and Generation of Gravitational Waves. *Phys. Rev.*, 117:306–313, Jan 1960.

[2] J. Weber. Evidence for discovery of gravitational radiation. *Phys. Rev. Lett.*, 22:1320–1324, 1969.

[3] P. Astone et al. The Gravitational wave detector NAUTILUS operating at T = 0.1-K. *Astropart. Phys.*, 7:231–243, 1997.

[4] M. Cerdonio et al. The ultracryogenic gravitational-wave detector AURIGA. *Classical and Quantum Gravity*, 14(6):1491, jun 1997.

[5] J. Aasi et al. Advanced LIGO. *Classical and Quantum Gravity*, 32(7):074001, mar 2015.

[6] F. Acernese et al. Advanced Virgo: a second-generation interferometric gravitational wave detector. *Classical and Quantum Gravity*, 32(2):024001, dec 2014.

[7] T. Akutsu et al. KAGRA: 2.5 Generation Interferometric Gravitational Wave Detector. *Nature Astron.*, 3(1):35–40, 2019.

[8] B. P. Abbott et al. Observation of Gravitational Waves from a Binary Black Hole Merger. *Phys. Rev. Lett.*, 116:061102, Feb 2016.

[9] M. Punturo et al. The Einstein Telescope: a third-generation gravitational wave observatory. *Classical and Quantum Gravity*, 27(19):194002, sep 2010.

[10] Albert Einstein. Die grundlage der allgemeinen relativitätstheorie. *Annalen der Physik*, 354(7):769–822, 1916.

[11] Albert Einstein. Näherungsweise integration der feldgleichungen der gravitation. *Sitzungsberichte der Königlich Preußischen Akademie der Wissenschaften*, pages 688–696, 1916.

[12] Albert Einstein. Über gravitationswellen. *Sitzungsberichte der Königlich Preußischen Akademie der Wissenschaften*, pages 154–167, 1918.

[13] Robert M. Wald. *General Relativity*. University of Chicago Press, 1984.

[14] M. Maggiore. *Gravitational Waves: Volume 1: Theory and Experiments*. Oxford University Press, 2007.

[15] F. Acernese et al. Measurements of Superattenuator seismic isolation by Virgo interferometer. *Astroparticle Physics*, 33(3):182–189, 2010.

[16] Jan Harms and Krishna Venkateswara. Newtonian-noise cancellation in large-scale interferometric GW detectors using seismic tiltmeters. *Classical and Quantum Gravity*, 33(23):234001, oct 2016.

[17] John Hanson, G Mac Keiser, Saps Buchman, Robert Byer, Dave Lauben, Daniel DeBra, Scott Williams, Dale Gill, Ben Shelef, and Gad Shelef. St-7 gravitational reference sensor: analysis of magnetic noise sources. *Classical and Quantum Gravity*, 20(10):S109, apr 2003.

[18] Marc Diaz-Aguiló, Enrique García-Berro, and Alberto Lobo. Inflight magnetic characterization of the test masses onboard LISA Pathfinder. *Phys. Rev. D*, 85:042004, Feb 2012.

[19] Zi-He Huang, Yan-Chong Liu, and Ze-Bing Zhou. Possibility analysis of a flat cuboid Au-Pt alloy test mass employed in space gravitational wave detection. *Classical and Quantum Gravity*, 42(11), 2025. Cited by: 0.

[20] Jia-Hao Xu, Wen-Long Ma, Ya-Ting Zhang, Qing-Lan Wang, Lin Zhu, and Qi Liu. Determining AC Magnetic Susceptibility of Kilogram-Level Test Masses for TianQin. *Chinese Physics Letters*, 42(7), 2025. Cited by: 0.

[21] Cristian Maria-Moreno, Ignacio Mateos, Guillermo Pacheco-Ramos, Francisco Rivas, María-Ángeles Cifredo-Chacón, Ángel Quirós-Olozábal, José-María Guerrero-Rodríguez, and Nikolaos Karnesis. Magnetic Field Simulation and Correlated Low-Frequency Noise Subtraction for an In-Orbit Demonstrator of Magnetic Measurements. *IEEE Transactions on Instrumentation and Measurement*, 73, 2024. Cited by: 1; All Open Access, Green Open Access, Hybrid Gold Open Access.

[22] A. Effler, R. M. S. Schofield, V. V. Frolov, G. González, K. Kawabe, J. R. Smith, J. Birch, and R. McCarthy. Environmental Influences on the LIGO Gravitational Wave Detectors during the 6th Science Run. *Class. Quant. Grav.*, 32(3):035017, 2015.

[23] W. O. Schumann. Über die strahlungslosen Eigenschwingungen einer leitenden Kugel, die von einer Luftschicht und einer Ionosphärenhülle umgeben ist. *Zeitschrift für Naturforschung A*, 7(2):149–154, 1952.

[24] W. O. Schumann. Über die Dämpfung der elektromagnetischen Eigenschwingungen des Systems Erde — Luft — Ionosphäre. *Zeitschrift für Naturforschung A*, 7(3-4):250–252, 1952.

[25] Eric Thrane, Nelson Christensen, and Robert Schofield. Correlated magnetic noise in global networks of gravitational-wave interferometers: observations and implications. *Phys. Rev. D*, 87:123009, 2013.

[26] Izabela Kowalska-Leszczynska, Marie-Anne Bizouard, Tomasz Bulik, Nelson Christensen, Michael Coughlin, Mark Gołkowski, Jerzy Kubisz, Andrzej Kulak, Janusz Mlynarczyk, Florent Robinet, and Maximilian Rohde. Globally coherent short duration magnetic field transients and their effect on ground based gravitational-wave detectors. *Classical and Quantum Gravity*, 34(7):074002, mar 2017.

[27] B. P. Abbott et al. Characterization of transient noise in Advanced LIGO relevant to gravitational wave signal GW150914. *Class. Quant. Grav.*, 33(13):134001, 2016.

[28] A. Cirone, A. Chincarini, M. Neri, S. Farinon, G. Gemme, I. Fiori, F. Paoletti, E. Majorana, P. Puppo, P. Rapagnani, P. Ruggi, and B. L. Swinkels. Magnetic coupling to the advanced Virgo payloads and its impact on the low frequency sensitivity. *Review of Scientific Instruments*, 89(11):114501, 11 2018.

[29] A. Cirone, I. Fiori, F. Paoletti, M. M. Perez, A. R. Rodríguez, B. L. Swinkels, A. M. Vazquez, G. Gemme, and A. Chincarini. Investigation of magnetic noise in advanced Virgo. *Classical and Quantum Gravity*, 36(22):225004, oct 2019.

[30] I. Fiori, F. Paoletti, M. C. Tringali, K. Janssens, C. Karathanasis, A. Menéndez-Vázquez, A. Romero-Rodríguez, R. Sugimoto, T. Washimi, V. Boschi, A. Chiummo, M. Cieślar, R. De Rosa,

C. De Rossi, F. Di Renzo, I. Nardecchia, A. Pasqualetti, B. Patricelli, P. Ruggi, and N. Singh. The Hunt for Environmental Noise in Virgo during the Third Observing Run. *Galaxies*, 8(4), 2020.

[31] Kamiel Janssens, Katarina Martinovic, Nelson Christensen, Patrick M. Meyers, and Mairi Sakellariadou. Impact of Schumann resonances on the Einstein Telescope and projections for the magnetic coupling function. *Phys. Rev. D*, 104(12):122006, 2021. [Erratum: Phys.Rev.D 105, 109904 (2022)].

[32] Kamiel Janssens et al. Correlated 1–1000 Hz magnetic field fluctuations from lightning over Earth-scale distances and their impact on gravitational wave searches. *Phys. Rev. D*, 107(2):022004, 2023.

[33] S. Rowan, S. M. Twyford, J. Hough, D. H. Ganezer, P. V. Lyons, R. K. Meyer, H. Radkins, S. Schiller, J. R. Williams, and P. Willems. Investigations into the effects of electrostatic charge on the q factor of a prototype fused silica suspension for use in gravitational wave detectors. *Physics Letters A*, 233(4-6):303–308, 1997.

[34] Michael J. Mortonson, Steve Vass, Sheila Rowan, and Phil Willems. Effects of electrical charging on the mechanical Q of a fused silica disk. *Review of Scientific Instruments*, 74(11):4840–4845, 2003.

[35] M. Hewitson, K. Danzmann, H. Grote, G. Heinzel, H. Luck, K. A. Strain, H. Ward, and B. Willke. Charge measurement and mitigation for the main test masses of the GEO 600 gravitational wave observatory. *Classical and Quantum Gravity*, 24(24):6379, 2007.

[36] L. G. Prokhorov and V. P. Mitrofanov. Space charge polarization in fused silica test masses of a gravitational wave detector associated with an electrostatic drive. *Classical and Quantum Gravity*, 27(22):225014, 2010.

[37] F. Acernese et al. Virgo Detector Performance during the O3 Run. *Physical Review Materials*, 130:141101, 2023.

[38] A. Chincarini, A. Cirone, and G. Gemme. FEA Charging Simulations. Technical report, Virgo Docs: VIR-0827B-18.

[39] Dennis Ugolini et al. Charging issues in LIGO. *Journal of Physics: Conference Series*, 32:032, 2007.

[40] V. P. Mitrofanov, L. G. Prokhorov, and K. V. Vitushkin. Investigation of effects associated with variation of electric charge on a fused silica test mass. *Classical and Quantum Gravity*, 21(5):S1083, 2004.

[41] D. Ugolini et al. Discharging fused silica optics occluded by an electrostatic drive. *Review of Scientific Instruments*, 84:054502, 2013.

[42] S. Buchman et al. Charge neutralization in vacuum for non-conducting and isolated objects using directed low-energy electron and ion beams. *Classical and Quantum Gravity*, 25:125001, 2008.

[43] COMSOL AB. *COMSOL Multiphysics®*. COMSOL AB, Stockholm, Sweden, 2022. Version 6.0.

[44] F. Amann, F. Bonsignorio, T. Bulik, H. J. Bulten, S. Cuccuru, A. Dassargues, R. DeSalvo, E. Fenyvesi, F. Fidecaro, I. Fiori, C. Giunchi, A. Grado, J. Harms, S. Koley, L. Kovács, G. Losurdo, V. Mandic, P. Meyers, L. Naticchioni, F. Nguyen, G. Oggiano, M. Olivieri, F. Paoletti, A. Paoli, W. Plastino, M. Razzano, P. Ruggi, G. Saccorotti, A. M. Sintes, L. Somlai, P. Ván, and M. Vasúth. Site-selection criteria for the Einstein Telescope. *Review of Scientific Instruments*, 91(9):094504, 09 2020.

[45] Stw and Neotesla. Schumann resonance 01 (english version). Wikimedia Commons, 2007. Licensed under CC BY-SA 3.0. Derivative work based on the original by Neotesla.

[46] H. Abe et al. The Current Status and Future Prospects of KAGRA, the Large-Scale Cryogenic Gravitational Wave Telescope Built in the Kamioka Underground. *Galaxies*, 10(3), 2022.

[47] Rosario De Rosa et al. Magnetometer measurement in Sos Enattos area. Technical report, ET Docs: ET-0211A-25.

[48] M. Coughlin et al. Measurement and subtraction of Schumann resonances at gravitational-wave interferometers. *Phys. Rev. D*, 97, May 2018.

[49] The Virgo Collaboration. Advanced Virgo Technical Design Report. Technical report, Virgo TDS: VIR-0128A-12, April 2012.

[50] Virgo Collaboration. assembly of the magnetic antisprings for SR tower. Virgo Logbook, Entry 32611, 2015.

[51] Virgo Collaboration. Filter0 upgrade for MC suspension. Virgo Logbook, Entry 30901, 2012.

[52] Virgo Collaboration. Gluing markers, magnets and spacers on IMC end mirror: day 2. Virgo Logbook, Entry 31124, 2013.

[53] Virgo Collaboration. NE payload dismounted and mirror removed. Virgo Logbook, Entry 60469, 2023.

[54] M. C. Tringali, I. Fiori, F. Paoletti, G. Quéméner, A. Chincarini, F. Bucci, C. Miritescu, F. Carbognani, R. Poulton, and R. De Rosa. Magnetic injections: overview and plans. Technical report, Virgo Docs: VIR-0300A-24.

[55] Conor Mow-Lowry et al. Low-frequency noise. Technical report, ET Docs: ET-0310A-21.

[56] J. M. D. Coey. *Magnetism and Magnetic materials.* Cambridge University Press, 2010.

[57] J. F. Dillinger and R. M. Bozorth. Heat Treatment of Magnetic Materials in a Magnetic Field I. Survey of Iron-Cobalt-Nickel Alloys. *Physics*, 6(9):279–284, 09 1935.

[58] A. Boglietti, A. Cavagnino, L. Ferraris, and M. Lazzari. The annealing influence onto the magnetic and energetic properties in soft magnetic material after punching process. In *International Electric Machines and Drives Conference.*, volume 1, pages 503–508, 2003.

[59] P. Arpaia, P. N. Burrows, M. Buzio, C. Gohil, M. Pentella, and D. Schulte. Magnetic characterization of Mumetal® for passive shielding of stray fields down to the nano-Tesla level. *Nuclear Instruments and Methods in Physics Research Section A: Accelerators, Spectrometers, Detectors and Associated Equipment*, 988:164904, 2021.

[60] A. Canova, F. Freschi, L. Giaccone, M. Repetto, and L. Solimene. Identification of Material Properties and Optimal Design of Magnetically Shielded Rooms. *Magnetochemistry*, 7(2), 2021.

[61] N. J. Ayres, G. Ban, G. Bison, K. Bodek, V. Bondar, T. Bouillaud, B. Clement, E. Chanel, P.-J. Chiu, C. B. Crawford, M. Daum, C. B. Doorenbos, S. Emmenegger, A. Fratangelo, M. Fertl, W. C. Griffith, Z. D. Grujic, P. G. Harris, K. Kirch, J. Krempel, B. Lauss, T. Lefort, O. Naviliat-Cuncic, D. Pais, F. M. Piegsa, G. Pignol, G. Rauscher,

D. Rebreyend, I. Rienäcker, D. Ries, S. Roccia, D. Rozpedzik, W. Saenz-Arevalo, P. Schmidt-Wellenburg, A. Schnabel, N. Severijns, B. Shen, M. Staab, K. Svirina, R. Tavakoli Dinani, J. Thorne, N. Yazdandoost, J. Zejma, G. Zsigmond, and The nEDM Collaboration. The very large n2EDM magnetically shielded room with an exceptional performance for fundamental physics measurements. *Review of Scientific Instruments*, 93(9):095105, 09 2022.

[62] A. W. Rücker. On the Magnetic Shielding of Concentric Spherical Shells. *Proc. Phys. Soc.*, 1892.

[63] U. Du Bois. On Magnetic Shielding. *The Electrician*, 1897.

[64] A. P. Wills. On the Magnetic Shielding Effect of Trilammeral Spherical and Cylindrical Shells. *The Physical Review*, 1899.

[65] D. Ma, M. Ding, J. Lu, J. Zhao, K. Yang, X. Fang, K. Wang, N. Zhang, and B. Han. Magnetic noise calculation of mu-metal shields at extremely low frequencies for atomic devices. *Journal of Physics D: Applied Physics*, 54(2):025004, oct 2020.

[66] J. B. Johnson. Thermal Agitation of Electricity in Conductors. *Physical Review*, 1928.

[67] H. Nyquist. Thermal Agitation of Electric Charge in Conductors. *Physical Review*, 1928.

[68] T. W. Kornack, S. J. Smullin, S.-K. Lee, and M. V. Romalis. A low-noise ferrite magnetic shield. *Applied Physics Letters*, 90(22):223501, 05 2007.

[69] Y. Gao, D. Ma, K. Wang, X. Xu, S. Li, Y. Dou, and J. Li. A low-noise multilayer mu-metal thin shell magnetic shield for ultra-highly sensitive atomic sensors. *Sensors and Actuators A: Physical*, 352:114207, 2023.

[70] P. Weiss. L'hypothèse du champ moléculaire et la propriété ferromagnétique. *Journal de Physique Théorique et Appliquée*, 1907.

[71] Lord Rayleigh. XXV. Notes on electricity and magnetism.—III. On the behaviour of iron and steel under the operation of feeble magnetic forces . *The London, Edinburgh, and Dublin Philosophical Magazine and Journal of Science*, 23(142):225–245, 1887.

[72] J. Sun, Y. Lu, L. Zhang, Y. Le, and X. Zhao. A Method to Measure Permeability of Permalloy in Extremely Weak Magnetic Field Based on Rayleigh Model. *Materials*, 15(20), 2022.

[73] B. Garaventa, F. Armato, A. Chincarini, and I. Fiori. Magnetic Noise Mitigation Strategies for the Einstein Telescope Infrastructure. *Galaxies*, 13(1), 2025.

[74] Hermann von Helmholtz. Ueber die Theorie der Elektrodynamik. *Annalen der Physik und Chemie*, 165(6):211–233, 1853. Original work on the mathematical formalization of the Helmholtz coil configuration.

[75] John David Jackson. *Classical Electrodynamics*. Wiley, New York, 3rd edition, 1998.

[76] Heike Kamerlingh Onnes. Further experiments with liquid helium. c. on the change of electric resistance of pure metals at very low temperatures etc. iv. the resistance of pure mercury at helium temperatures. *Comm. Phys. Lab. Univ. Leiden*, 120:3–15, 1911.

[77] F. London, H. London, and F. A. Lindemann. The electromagnetic equations of the supraconductor. *Proceedings of the Royal Society of London. Series A - Mathematical and Physical Sciences*, 149(866):71–88, 1935.

[78] V. L. Ginzburg. Magnetic Flux Quantization in a Superconducting Cylinder. *Soviet Physics Jetp*, 1962.

[79] H. Lung-Tao and G. F. Zharkov. Hollow Superconductors in a Magnetic Field. *Soviet Physics Jetp*, 1963.

[80] N. Rotheudt, M. Fracasso, P. Vanderbemden, and L. Gozzelino. Superconductor-based passive shielding and screening systems. *Superconductor Science and Technology*, 38(4):043002, mar 2025.

[81] C. Kittel. *Introduction to Solid State Physics*. John Wiley & Sons, 2005.

[82] G. Grosso and G. P. Parravicini. *Solid State Physics*. Academic Press, 2014.

[83] Laurent Wera, Jean-François Fagnard, et al. Magnetic Shielding of Open and Semi-closed Bulk Superconductor Tubes: The Role of a Cap. *IEEE Transactions on Applied Superconductivity*, 29(3):1–10, 2019.

[84] F. Armato, B. Garaventa, and A. Chincarini. Einstein telescope: Ferromagnetic shielding for magnetic noise mitigation. *Il Nuovo Cimento C (Incontri di Fisica delle Alte Energie - IFAE 2025)*, 49(1-2):4, 2026.

[85] B. D'Angelo et al. Advanced Virgo Technical Design Report. Technical report, Virgo TDS: VIR-1091A-23, November 2023.

[86] B. D'Angelo et al. Advanced Virgo Technical Design Report. Technical report, Virgo TDS: VIR-1087A-24, December 2024.

[87] B. Garaventa, F. Armato, A. Chincarini, I. Fiori, F. Paoletti, G. Quéméner, and M.C. Tringali. Magnetic noise mitigation for upcoming gravitational waves detectors. *Nuclear Instruments and Methods in Physics Research Section A: Accelerators, Spectrometers, Detectors and Associated Equipment*, 1080:170637, 2025.

[88] B. Garaventa, V. Sequino, W. Ali, F. Sorrentino, J. P. Zendri, A. Chincarini, I. Fiori, F. Armato, R. De Rosa, M. Graziaplena, F. Paoletti, G. Quéméner, and M. C. Tringali. Future gravitational wave detectors: Phase noise investigation and magnetic noise mitigation strategies. *Nuclear Instruments and Methods in Physics Research Section A: Accelerators, Spectrometers, Detectors and Associated Equipment*, 1066:169629, 2024.

[89] I. Fiori and A. Chincarini. Magnetic noise: ET mitigation POC, capitalizing on Virgo lessons. Technical report, ET Docs: ET-0175A-23, May 2023.

[90] B. Garaventa. Magnetic Noise WP status - ANM division meeting. Technical report, ET Docs: ET-0512A-23, December 2023.

[91] F. Armato, B. Garaventa, and A. Chincarini. MAgnetic Noise test facility for ET (MANET). Technical report, ET Docs: ET-0210A-25, April 2024.

[92] Virgo Collaboration. NE Payload assembled and ready for electrical check. Virgo Logbook, Entry 60483, 2023.

[93] Virgo Collaboration. NE payload integrated. Virgo Logbook, Entry 60507, 2023.

[94] Virgo Collaboration. Installation of NE payload completed. Virgo Logbook, Entry 60513, 2023.

[95] D. Bridges. Quadruple Suspension Controls Arrangement. Technical report, LIGO DCC: LIGO-E1000617-v6, October 2010.

[96] D. Bridges. Beamsplitter/Folding Mirror Controls Arrangement. Technical report, LIGO DCC: LIGO-E1100108-v3, February 2011.

[97] T. Akutsu et al. Construction of the KAGRA electrostatic actuator system. *Optical and Quantum Electronics*, 49:163, 2017.

[98] Federico Armato and Andrea Chincarini. *AI-Powered Charge Monitoring in Interferometers*, pages 85–100. Springer Nature Singapore, Singapore, 2025.

[99] Virgo Collaboration. WI Payload: TCS and Baffles installation. Virgo Logbook, Entry 57972, 2022.

[100] L. Spallino et al. Can electrons neutralize the electrostatic charge on test mass mirrors in gravitational wave detectors? *Phys. Rev. D*, 105(4):042003, 2022.

[101] P. Campsie et al. Charge mitigation techniques using glow and corona discharges for advanced gravitational wave detectors. *Classical and Quantum Gravity*, 28(21):215016, sep 2011.